

**Electrode-Specific Degradation Diagnostics
for Lithium-Ion Batteries with Practical Considerations**

by

Suhak Lee

A dissertation submitted in partial fulfillment
of the requirements for the degree of
Doctor of Philosophy
(Mechanical Engineering)
in the University of Michigan
2021

Doctoral Committee:

Associate Research Scientist Jason B. Siegel, Co-chair
Professor Anna G. Stefanopoulou, Co-chair
Assistant Professor Bryan R. Goldsmith
Assistant Professor Youngki Kim

Suhak Lee

suhaklee@umich.edu

ORCID iD: [0000-0003-2582-6194](https://orcid.org/0000-0003-2582-6194)

© Suhak Lee 2021

DEDICATION

To
My loving wife Gieun Kim
And my family

ACKNOWLEDGMENTS

First and foremost, I would like to express my gratitude to my advisors, Professor Anna Stefanopoulou and Associate Research Scientist Jason Siegel, for their remarkable guidance, encouragement, and support. Prof. Stefanopoulou and Dr. Siegel provided me the opportunity to work on state-of-the-art lithium-ion batteries.

I am thankful to the committee members, Assistant Professor Bryan Goldsmith and Assistant Professor Youngki Kim, for taking the time and interest in evaluating my work and for providing their critical feedback. I truly believe that their insightful comments have led this dissertation to be more thorough and complete.

It has been a great pleasure working with all my colleagues in the Powertrain Control Laboratory that I cannot thank enough for their company and enthusiastic discussion - Peyman Mohtat, Miriam Figueroa, Ting Cai, Sravan Pannala, Vivian Tran, Dr. Valentin Sulzer, and Andrew Weng. Thanks to my friends in Ann Arbor and around the world who made my Ph.D. full of good times.

I would like to recognize financial support from Samsung SDI, South Korea. Thanks to the colleagues at Samsung SDI - Dr. Tae-Kyung Lee and Jang-Woo Lee, for exciting discussion and feedback.

I would also like to thank Professor Jun Ni, who allowed me to embark on the Ph.D. program and work on both physics and data-driven approaches in fault diagnostics and prognostics.

Special thanks go to my loving wife, Gieun Kim. Without her love and support, I would not have completed this Ph.D. journey. I am incredibly thankful to my family in South Korea for their unconditional love and faith in me that made me keep moving forward.

I want to end with a quote that I have always wished for my life. "Stay hungry, Stay foolish."

TABLE OF CONTENTS

DEDICATION	ii
ACKNOWLEDGMENTS	iii
LIST OF FIGURES	vii
LIST OF TABLES	ix
ABSTRACT	x
CHAPTER	
1 Introduction	1
1.1 Battery Degradation and State-of-Health	1
1.1.1 Degradation Modes of Li-ion Batteries	2
1.2 The Need of Advanced Diagnostics and State of the Art	5
1.2.1 Battery Cell-Level State of Health Estimation	7
1.2.2 Electrode-Specific Degradation Diagnostics	9
1.3 Contributions and Dissertation Organization	10
2 Li-ion Battery Models and Electrode-Specific Degradation Diagnostics	14
2.1 Introduction	14
2.2 Overview of Li-ion Battery Models	14
2.3 Open Circuit Voltage Model	16
2.3.1 Half-cell Potential Function	16
2.3.2 Parameterization with Electrode Parameters	17
2.4 Electrode-Specific Degradation Diagnostics	19
2.5 Experimental	21
2.5.1 Half-cell Potential Function Identification	21
2.5.2 Electrode Parameter Identification	23
2.6 Conclusion	26
3 Estimation Considering Positive Electrode Half-Cell Potential Change Due to Aging .	27
3.1 Introduction	27
3.2 Estimation of Electrode State of Health Parameters	28
3.2.1 Conventional Voltage Fitting Method	28
3.2.2 Proposed Peak Alignment Method	30
3.3 Experimental Results	33

3.3.1	Test Cell and Aging Condition	33
3.3.2	Fresh cell	35
3.3.3	Aged cell	36
3.3.4	Aged cell with Half-cell potential calibration	39
3.4	Discussion	39
3.4.1	Half-cell potential change	40
3.4.2	Electrode state of health diagnostics	42
3.5	Conclusion	43
4	Estimation Accuracy with Limited Data Availability	46
4.1	Introduction	46
4.2	Methodology	46
4.2.1	OCV model and parameter estimation	46
4.2.2	Error bound of parameter estimation	47
4.3	Results and Discussion	51
4.3.1	Data window	52
4.3.2	Analytic error bounds of electrode parameters	53
4.3.3	Impact of voltage constraint	56
4.4	Validation	58
4.4.1	Numerical validation	58
4.4.2	Experimental validation	61
4.5	Conclusion	61
5	Minimum-Time Measurement of Open Circuit Voltage of Battery Systems	65
5.1	Motivation and Connection to Electrode Degradation Diagnostics	65
5.2	Minimum-Time Optimal Control Problem	67
5.2.1	Battery model	67
5.2.2	Formulation of minimum-time optimal control problem	69
5.3	Pontryagin Analysis for Optimal Control Sequence	70
5.3.1	Minimum-Time control without active state constraints	70
5.3.2	Minimum-time control with active state constraints	71
5.3.3	Optimal input current sequence	73
5.4	Conversion to Switching Time Optimization	75
5.4.1	Switching time optimization for inactive state constraint	75
5.4.2	Switching time optimization for active state constraint	75
5.5	Simulation Results	76
5.5.1	Comparison between ordinary pulse-relation profile and minimum-time current profile	76
5.5.2	Minimum-time current profile with active state constraint	80
5.5.3	Sensitivity of model parameter error	82
5.5.4	Reformulated switching time problem	84
5.6	Experimental Validation	85
5.6.1	Comparison between Pulse-Relaxation and Minimum-Time Profile	86
5.7	Conclusion	89
6	Electrode-Specific Degradation Diagnostics at Practical Charging Rate	90

6.1	Introduction	90
6.2	Practical Charging Rate	91
6.3	Peak Smoothing with Increasing Current Rates	93
6.3.1	Peak Behavior Map	93
6.3.2	Analysis on Peak Smoothing Phenomenon	96
6.4	Overpotential due to Internal Resistance	101
6.4.1	Battery model	101
6.4.2	Sensitivity-based Least Square Estimation	102
6.4.3	Adaptive Algorithm	105
6.5	Results and Discussion	106
6.5.1	Resistance Estimation via Window Least Square Estimation	106
6.5.2	Electrode SOH Estimation Error due to Inaccurate Resistance	109
6.6	Conclusion	111
7	Physics-Guided Machine Learning for Battery Diagnostics and Prognostics	112
7.1	Introduction	112
7.2	Case Study 1: Electrode Degradation Diagnostics using Neural Network	113
7.2.1	Background	113
7.2.2	Proposed Data-driven Method using Neural Network	114
7.2.3	Degradation Simulation and Electrochemical Features	114
7.2.4	Results and Discussion	118
7.2.5	Interpretable Machine Learning	121
7.2.6	Summary	124
7.3	Case Study 2: Early Prediction of Battery Cycle Life	124
7.3.1	Background	124
7.3.2	Experimental Method and Data Generation	124
7.3.3	Feature Extraction and Machine Learning Approach	126
7.3.4	Results and Discussion	128
7.3.5	Summary	131
7.4	Conclusion	131
8	Conclusions and Future Work	135
8.1	Summary of Contributions	135
8.2	Future work	136
8.2.1	Degradation diagnostics for field use cases	137
8.2.2	Second-life batteries via advanced battery degradation diagnostics	137
8.2.3	Physics-guided machine learning in battery lifetime prediction	138
	APPENDIX A Optimal Control Theories	140
A.1	State Constraints In Optimal Control Problem	140
A.2	Number of Switching Point	141
	BIBLIOGRAPHY	142

LIST OF FIGURES

FIGURE

1.1	Degradation mechanisms in Li-ion cells	3
1.2	Degradation mechanisms: Causes, effects and degradation modes in Li-ion cells	5
1.3	Life cycle of traction batteries	7
2.1	An example of the equivalent circuit model: OCV-R-RC-RC	15
2.2	Open circuit voltage (OCV) of a cell aligned with the utilization window of individual electrodes	20
2.3	Half-cell potential of electrodes and their function fit	22
2.4	Full-cell C/20 data and the OCV model fit	25
3.1	Flowchart for the proposed peak alignment method	31
3.2	Voltage curve and differential voltage curve for an NMC/graphite cell	32
3.3	Results of the fresh cell from the conventional voltage fitting (VF) method and the proposed peak alignment (PA) method	37
3.4	Results of the aged cell from the conventional voltage fitting (VF) method and the proposed peak alignment (PA) method	38
3.5	Results on the aged cell from the conventional voltage fitting (VF) method and the proposed peak alignment (PA) method after updating the positive electrode potential function $U_p(y)$ from the calibration	40
3.6	Positive electrode half-cell potential change is identified from the proposed peak alignment (PA) method with $U_p(y)$ calibration	41
3.7	Electrode state of health (eSOH) diagnostic results with degradation modes	43
4.1	Half-cell potential of individual electrodes and OCV of a NMC/graphite cell	48
4.2	Definition of data window	52
4.3	Data windows (DWs) for different battery usage patterns	53
4.4	The analytic error bound of each electrode parameter in a logarithm scale	54
4.5	The analytic error bound of each electrode parameter for various data windows	55
4.6	Analytic error bound with respect to depth of discharge (DOD)	57
4.7	Scatter plot of the electrode parameter estimation errors from Monte Carlo simulation for the DW-deep case	59
4.8	The OCV model fit for the given full-range data of a NMC/graphite cell	62
4.9	Experimental estimation errors for the electrode parameters under different data windows	63
5.1	Example of incremental open-circuit voltage (OCV) measurement	65
5.2	Schematic of two-stage OCV measurement strategy	67

5.3	Schematic of equivalent circuit model (ECM) with double RC pairs	68
5.4	Schematic of bang-bang control trajectory	72
5.5	Schematic of bang-off-bang control trajectory	74
5.6	Ordinary pulse-relaxation for OCV measurement	78
5.7	Minimum-time current profile for OCV measurement	79
5.8	Minimum-time current profile for OCV measurement with an active state constraint for $SOC_{max} = 0.60$	81
5.9	Trad-off relationship between total testing time and the level of SOC upper bound . . .	82
5.10	Minimum-time current profile for OCV measurement with 10% model parameter errors	83
5.11	Experimental results for pulse-relaxation profile and minimum-time profile	87
5.12	Relaxation voltage with respect to the OCV reference	88
6.1	Experimental data of voltage and differential voltage curves with increasing charging rates	93
6.2	Peak behavior map with respect to charging rate for three different ambient temperatures	97
6.3	Peak distance with respect to cell state-of-health and charging rate	98
6.4	Comparison of the voltage between the experimental data and three electrochemical models at different charging rates	98
6.5	Simulation results of terminal voltage and differential voltage curves with increasing charging rates	99
6.6	Simulation results of surface concentration of lithium using DFN model	100
6.7	Example of sensitivity-based data selection strategy	105
6.8	Proposed framework with an adaptive parameter estimation from two separate datasets	106
6.9	Current profile of synthetic drive cycle	107
6.10	Sensitivity of equivalent circuit parameters with synthetic drive cycle	108
6.11	Estimation error statistic (i.e. mean and standard deviation) of equivalent circuit model parameters with and without data selection strategy	109
6.12	Estimation error of electrode parameters with respect to resistance error	111
7.1	Schematic structure for a three layer feed-forward neural network	114
7.2	Evolution of three different data curves with increments of three different degradation modes	116
7.3	Defined features from the IC and DV curves	117
7.4	Schematic view of training and testing data sets	118
7.5	Averaged test errors (MAE and RMSE) over the test data set for three independent degradation modes	120
7.6	Correlation matrix for input features	122
7.7	Partial dependence plots (PDP) for the selected features for three degradation modes .	123
7.8	Discharge capacity curves and correlation with Ah-throughput life, indicating the dif- ficulty of the early prediction	126
7.9	Features from the discharge voltage curves	126
7.10	Ah-throughput life predictions using a ridge regression algorithm	129
7.11	Map between the variance of ΔQ_{190-10} and degradation modes	130
7.12	Correlation between the log of the variance of ΔQ_{190-10} and the Ah-throughput life with varying data window size	130

LIST OF TABLES

TABLE

2.1	The NMC/graphite pouch cell specification	24
2.2	The identified electrode parameters for fresh NMC/graphite pouch cell	25
3.1	Test cells and aging condition	36
3.2	The parameter estimates from the fresh and aged cells	45
4.1	Nominal parameters for the selected NMC/graphite cell	52
4.2	Estimation error bound for unconstrained case	58
4.3	Estimation error bound for constrained case	60
4.4	Estimation errors for the experimental validation under different data windows	64
5.1	Comparison of total testing time without active state constraint	80
5.2	Comparison of total testing time with active state constraint	80
5.3	Comparison of total testing time with 10% model parameter errors	84
5.4	Comparison of two different solutions in switching points with the computation time	85
5.5	Comparison of two different solutions in switching points under the presence of an active state constraint	86
5.6	Identified parameters for the equivalent circuit model	86
5.7	Comparison of total testing time for one OCV measurement from experiment	89
6.1	Estimated charge time chart for battery electric vehicles	92
6.2	Cycle aging test condition matrix	94
6.3	C-rate dependency test procedure	95
7.1	Nominal parameters for a LFP/graphite cell	115
7.2	Degradation simulation scenarios	117
7.3	Parametric study for selecting the best NN model structure	120
7.4	The aging test conditions matrix	133
7.5	Log-correlation of various statistics of the discharge difference curve, ΔQ_{190-10} , with Ah-throughput life	134

ABSTRACT

Li-ion batteries inevitably degrade with cyclic usage and storage time. Close to end-of-life batteries can no longer meet their performance requirements and the likelihood of occurring catastrophic failures increases. Thus, an accurate diagnosis of their state of health over long-term use has become a critical function for reliable and safe battery management systems, especially for vehicle electrification and large scale energy storage systems. Degradation of batteries is typically quantified at the cell level with capacity loss and power fade, however different usage conditions and environmental factors can contribute to the degradation of batteries differently. Therefore, typical cell-level lumped degradation metrics are not sufficient to give a full explanation of battery state of health.

This dissertation presents approaches for the diagnosis of electrode-specific degradation of Li-ion batteries considering a variety of practical aspects in real-world applications such as the half-cell potential change, the partial data availability, data acquisition method, and practical charging rate. The electrode-specific degradation diagnosis is performed by model-based identification of the individual electrode state-of-health (eSOH) parameters, electrode capacity and utilization range.

The advancements contributed by this dissertation are summarized as follows. First, a novel diagnostic algorithm is proposed by combining the terminal voltage fitting process with the peak alignment method to improve electrode parameter estimation confidence. The proposed method addresses the half-cell potential change of the positive electrode due to the chemical aging of the metal oxide. The diagnostic result is experimentally verified with large-format prismatic commercial cells. The second practical consideration is partial data availability. In practice, the full range of OCV measurement is not obtainable without the designated offline diagnostic test. With the limited data, the accuracy of parameter estimation becomes questionable. Therefore, the achievable estimation error bound is analyzed with respect to partial data windows through the Cramer-Rao Bound and confidence interval. The result shows that the eSOH estimation improves when a data window includes slope changes of electrode half-cell potential. This fundamental limitation is applied in data-driven approach to provide data-requirements for machine learning of battery cycle life prediction. Third, continued from the partial window idea, a time-optimal current profile is proposed to enable direct measurement of pseudo-OCV data for the desired range without a long relaxation period. By allowing bi-directional charging, the proposed time-optimal control

problem identifies a proper sequence of charge/discharge pulses and successfully reduces total data acquisition time by more than 60% in both simulation and experiment, showing a possible way to implement the developed OCV-based electrode degradation diagnostic algorithm. Fourth, the feasibility of the electrode-specific degradation diagnostics is studied for real-world charging conditions where the typical charging current rate is usually higher (e.g. $C/5$) than $C/20$ of pseudo-OCV data. With increasing charging rates, the individual electrode's electrochemical features is obscured, and the overpotential due to internal resistance needs to be estimated concurrently, making the eSOH estimation challenging. An adaptive algorithm with a data selection strategy is proposed to deal with the estimation of both resistance and electrode SOH parameters. Lastly, the potential of the physics-guided machine learning approaches is explored with two case studies for Li-ion battery degradation diagnostics and prognostics.

CHAPTER 1

Introduction

1.1 Battery Degradation and State-of-Health

Lithium-ion (Li-ion) batteries are imperative for various applications ranging from consumer electronics to the transportation industry as a critical energy storage device. Especially in electric vehicles (EVs) and stationary energy storage systems (ESS) applications, it has become a dominant solution due to their high energy density and long lifespan. However, the performance of batteries gradually deteriorates with time and usage over their lifetime. For battery-powered systems, it is important to understand the battery degradation to manage both the performance of the systems and warranty liabilities. Underestimation of the battery life can be too conservative for system design, and overestimation could cause large financial losses.

Degradation of batteries is an inevitable phenomenon due to the undesirable chemical and mechanical reactions inside the battery. These side reactions are usually irreversible and result in a reduction of available energy per full-charge and failure to meet the power requirement due to the internal resistance increase. To quantify such performance degradation, cell capacity and internal resistance are often used as parameters in defining the state-of-health (SOH) of batteries. Cell capacity is a measure of the total electrical charge it can store, represented in ampere-hours (Ah). Internal resistance is directly related to cell power that describes how quickly a cell can provide the stored energy. An aged cell with the increased internal resistance provides less power than a fresh cell for the same withdrawing current. As a metric, the battery SOH is quantified by the ratio of the current capability of a battery cell to that of at the beginning of their life. Generally speaking, determining the SOH of a battery pack composed of multiple cells is not straightforward due to cell-to-cell variability. The cell-to-cell variability within a battery pack is still an active research problem, where it can be caused by manufacturing variability or non-uniform temperature distribution due to an imperfect cooling system. In most cases, the battery pack SOH is typically determined by the weakest cell in a series string. Therefore, the battery SOH in this thesis refers to individual cell performance.

Typically, batteries are categorized into two types based on their serving purposes: an energy cell or a power cell. The former is aiming to maximize the energy storage capacity for a long run-time while the latter is designed for high-power delivery such as power tools. As a general rule, energy content optimization is realized at the expense of power capability and vice versa. Given these differences, the most common way of defining the SOH is based on capacity loss or internal resistance increase for capacity fade or power fade, respectively [20]. Over a number of cycles, the capacity of a Li-ion cell will drop due to a variety of degradation mechanisms. Typically, if an aged cell is fully charged and discharged to its lower voltage limit, the charge drawn from the cell will be less than that of when it was new. For electric vehicle applications, the ability to achieve the maximum range is most important, hence the SOH is based on a comparison of current cell capacity with respect to fresh cell capacity as shown in Eq. (1.1). On the other hand, for hybrid electric vehicles (HEV) that use the battery system for power assist, the ability to deliver a specified power level is more important than the total capacity. As cells age, their internal resistance increases, resulting in a voltage drop for a given load and negatively impacting their ability to provide peak power. Thus, the SOH for power cells is quantified as a function of its increasing internal resistance as it ages as represented in Eq. (1.2). Typically, the internal resistance is measured from DC resistance by hybrid pulse power characterization [17] or electrochemical impedance spectroscopy [2]. Based on the loss of the capacity or increase of the internal resistance, the simplest form of SOH metrics can be written as follows,

$$SOH_{capacity} = \frac{\text{Cell capacity now}}{\text{Cell capacity when new}} \times 100, \quad (1.1)$$

$$SOH_{resistance} = \frac{\text{Internal resistance when new}}{\text{Internal resistance now}} \times 100. \quad (1.2)$$

1.1.1 Degradation Modes of Li-ion Batteries

Capacity and power fade in Li-ion batteries result from various degradation mechanisms in different cell components: the electrodes, the electrolyte, the separator, and the current collectors. Fig. 1.1 [8] illustrates some of the most commonly reported degradation mechanisms in Li-ion cells. These degradation mechanisms result in a loss of cyclable lithium for intercalation in the electrodes, electrolyte decomposition, active material loss from the electrodes, increased internal resistance due to resistive film formation, phase changes in the active materials, and loss of electrical contact between the electrodes and current collector.

From a diagnostic perspective, it is very challenging to identify those individual degradation

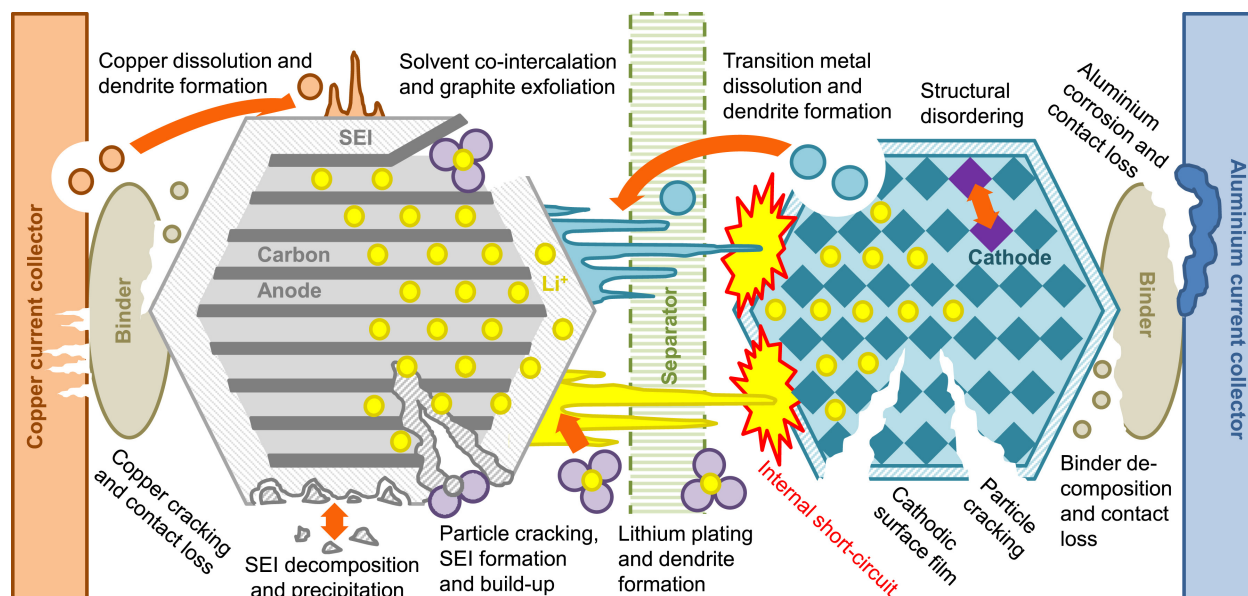


Figure 1.1: Degradation mechanisms in Li-ion cells. Figure from [8]

mechanisms responsible out of the large number of possible mechanisms due to their complicated inter-dependencies. Since not every individual degradation mechanism produces a unique aging effect, degradation mechanisms with the same physical effect can be grouped into a few degradation modes, as suggested by Bloom *et al.* [11] and Dubarry *et al.* [26]. The widely accepted degradation modes are [8]:

1. **Loss of lithium inventory (LLI).** LLI is related to the consumption of Li-ions by side reactions such as, solid electrolyte interface (SEI) formation on the surface of the graphite negative electrode, electrolyte decomposition reactions, lithium plating etc. Li-ions consumed by such parasitic reactions are irreversible, leading to capacity fade. LLI can also occur when the lithiated electrode material is isolated, trapping in the electrode material and making it unavailable for subsequent charge/discharge.
2. **Loss of active material at positive electrode (LAM_{PE}).** LAM indicates active material is no longer available for lithium insertion and extraction. LAM_{PE} can be caused by structural disordering, metal ion dissolution, particle cracking or loss of electrical contact. These processes can lead to both capacity and power fade.
3. **Loss of active material at negative electrode (LAM_{NE}).** LAM_{NE} indicates active material at the negative electrode is no longer available for lithium insertion and extraction due to particle cracking, blockage of active sites by resistive surface layers, and loss of electrical contact. These processes can lead to both capacity and power fade.

Each degradation mechanism has its own causes and stress factors in areas such as battery chemistry, environmental conditions (e.g. temperature, mechanical stress), and usage patterns (e.g. operating range, input current). For instance, batteries degrade even when not in use, called calendar aging, of which main stress factors are high storage SOC and high temperature [34]. High SOC implies low lithium concentration in the active material of the positive electrode, which increases the tendency to chemically decompose electrolyte. When it comes to cyclic aging, it is affected by additional factors, such as over-charge/discharge, current rate, and depth of discharge [56]:

- **High temperature:** accelerates side reactions, including (i) SEI layer growth rates on the negative electrode, resulting in LLI and internal resistance increase [108, 1], (ii) metal ion dissolution [108, 96], and (iii) electrolyte decomposition, with (ii) and (iii) causing LAM and LLI.
- **Low temperature:** slows down the transport of Li ions in both electrodes and the electrolyte. As a result, at low temperatures, local lithium plating at the graphite negative electrode may occur due to the low electrode polarization potential [108, 44], leading to LLI [7]. Continuous growth of lithium dendrite can cause catastrophic failure of Li-ion batteries by penetrating the separator and causing an internal short circuit.
- **Over-charge/discharge:** when a cell is overcharged, the positive electrode active material is over-delithiated and the negative electrode is over-lithiated. The positive electrode materials suffers from irreversible structural change when over-delithiated [81], and the dissolution of transition metal ions and active material decomposition [124, 33], resulting in LAM. Significant increase of the total internal resistance was found during the overcharging process [39]. During over-discharging, the negative electrode potential increases which leads to the anodic dissolution of the copper (Cu) current collector and formation of Cu^{2+} ions [123].
- **High rate currents:** excessive charge and discharge currents can cause localized over-charge and over-discharge to occur, leading to the same degradation mechanisms as over-charge/discharge [56]. For graphite negative electrode, fast charging results in metallic Li plating due to the graphite's limited ability to accept Li-ions at high current rates, leading to LLI [14, 95]. In addition, high rate currents cause a rapid increase in cell temperature and consequently can affect the degradation rate.
- **Mechanical stresses:** Li-ion cells are subjected to stress from different sources. In a pack, cells are packaged in a constrained space (e.g. external preload is applied), electrode materials exhibit a volume change induced by lithium intercalation and de-intercalation [71]. The

electrode materials can suffer from material failure such as cracking or fracture at the localized maximum stress areas, most likely near the separator [29]. This can result in significant degradation of cell performance and capacity fade [75, 12].

Yet, most of the commonly reported degradation mechanisms can fall into one of the three degradation modes. Fig. 1.2 [8] summarizes an overview of the causes and effects of widely known degradation mechanisms and categorizes them into the three degradation modes. These degradation mechanisms leave a fingerprint on the open circuit voltage (OCV). Hence, as the cell ages, the cell's OCV curve change can be used for electrode-specific degradation diagnostics. To sum up, it is necessary to detect the type and extent of degradation inside Li-ion cells to prevent an abrupt failure and maximize the utilization, and this can be performed by exploring the OCV of the cell.

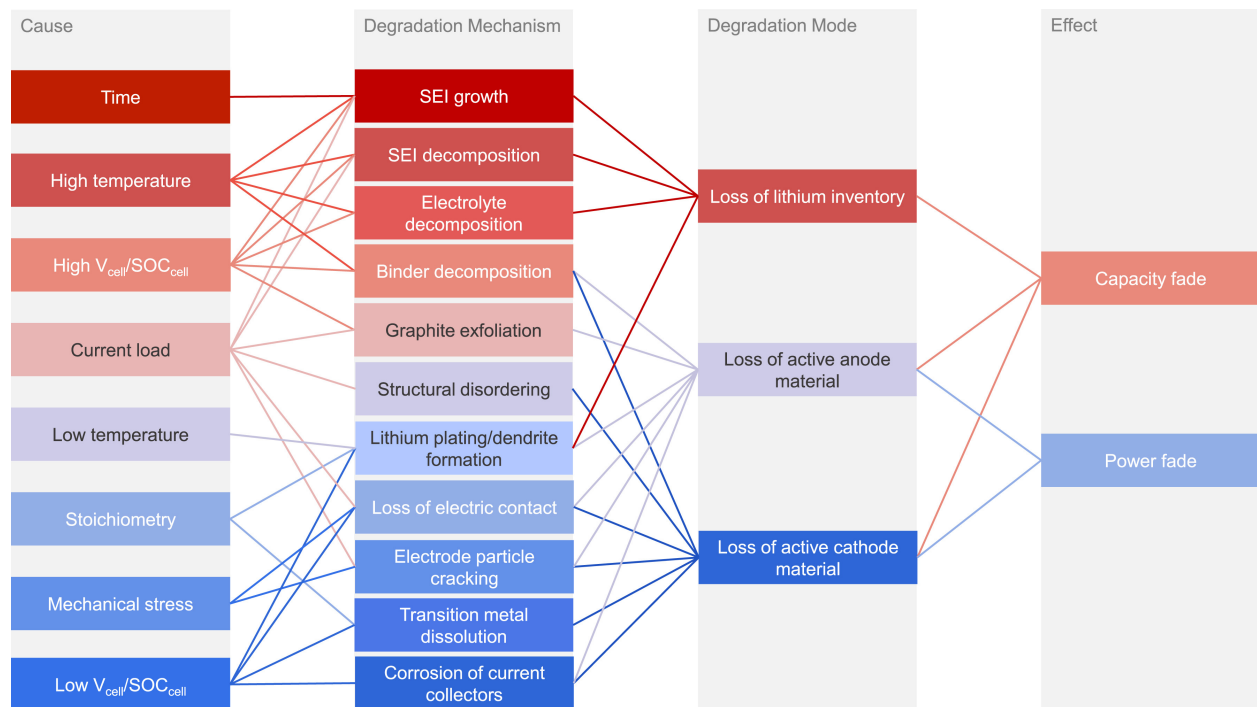


Figure 1.2: Degradation mechanisms: Causes, effects and degradation modes in Li-ion cells. Figure from [8]

1.2 The Need of Advanced Diagnostics and State of the Art

Degradation of Li-ion batteries is often characterized at a cell level, based on capacity loss or resistance increase. However, a detailed understanding of battery degradation is still necessary because the actual state-of-health of Li-ion batteries can be different depending on how they were used,

even if they have the same capacity or resistance values. For instance, two given aged cells (assuming historical data is not provided, but the characterization test is performed) can have very similar capacity values, but they could have undergone totally different degradation paths. Different usage conditions and environmental factors can cause the degradation of Li-ion cells differently. Then, the capacity-based-cell-level SOH metric fails to distinguish them as a different state of health. This is because the capacity fade results from a complex interplay of physical and chemical degradation mechanisms inside a cell. Therefore, advanced battery degradation diagnostics is needed. There can be four broad different aspects of the usefulness of the battery degradation diagnostics.

- **Intelligent Battery Management:** by taking the battery degradation into account, the battery management system (BMS) can be more accurate and reliable across the battery life [73]. As the battery ages, the battery model used in the battery management system becomes off from the physical battery's actual state. Thus, proper model calibration is required to keep the model prediction accurate. One common practice is state of charge (SOC) estimation associated with changes in battery capacity [125]. Furthermore, with a correct battery model, health-aware optimal control [120, 90] is possible for intelligent and safer battery operation. For instance, Samad *et al.* [90] showed power capability calculation considering capacity loss and resistance increase to reduce the number of Li-ion cells in the pack.
- **Remaining Useful Life Prediction:** with knowledge of the current and historical state of health of batteries, one can extend this into the future for predicting the remaining useful life (RUL). Battery RUL prediction is one of the most active research topics [89, 86, 116] in that it can be beneficial in many aspects such as maintenance scheduling, warranty liability, and safety assurance. To develop a reliable battery prognostics solution, an accurate understanding of the current SOH of batteries and diagnostics that enable BMS to interpret the possible issues is essential.
- **Second Life Batteries:** the global plug-in electric vehicle (BEVs & PHEVs) industry has continued to expand at a rapid pace with significant improvements in battery technology and global efforts on environmental protection from emissions. With the continued global growth of vehicle electrification, a new opportunity is emerging for the ESS and power systems using second-life EV batteries [13, 63] as illustrated in Fig. 1.3. Stationary energy-storage applications require less frequent battery cycling (e.g. 100 to 300 cycles per year) compared to automotive applications, which makes the reuse of retired EV batteries a viable and important option to bolster a local utility's power and energy reserves at a lower cost.
- **Feedback on Cell Design for Improvement:** with the advanced diagnostics for battery degradation along with historical data from diverse environmental and usage conditions, one

can find a correlation between battery degradation and the operating conditions [121]. For instance, if the battery cell undergoes severe loss of negative electrode active material at a particular usage condition (e.g. hot operating temperature), the battery manufacturer could improve the anode material or design to address this specific degradation. Another aspect is an adaptation for field applications. Unlike the lab-based aging study where aging test conditions are under control, real-world operating conditions can vary to a large extent. Therefore, the diagnostic algorithm that is robust and flexible is required to encounter unfavorable situations.

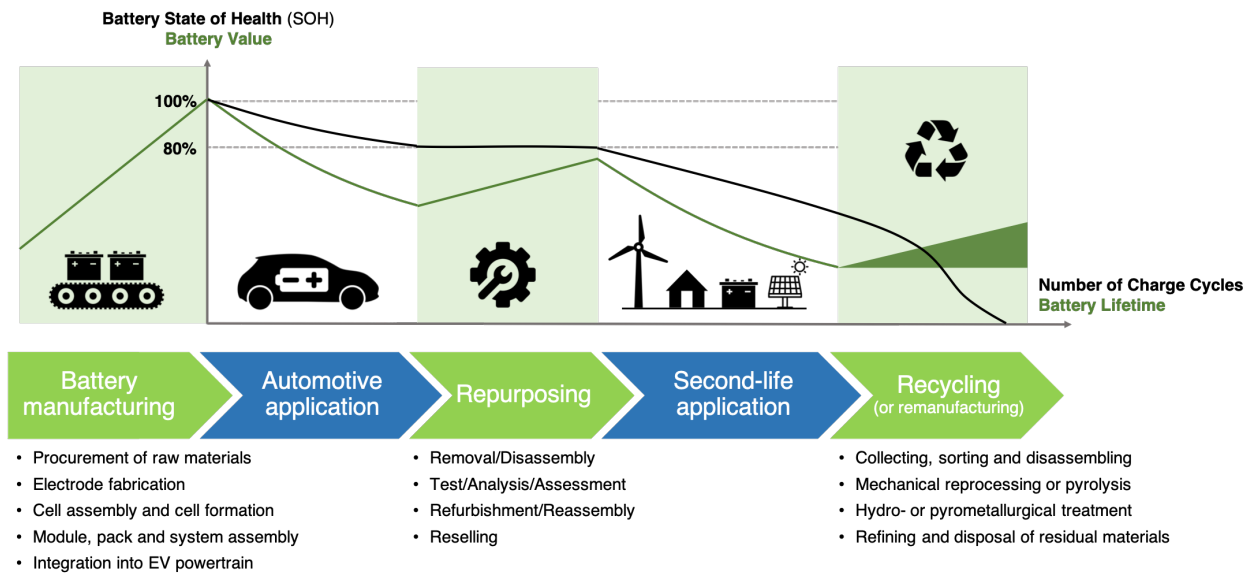


Figure 1.3: Life cycle of traction batteries. Figure is reproduced from [83].

1.2.1 Battery Cell-Level State of Health Estimation

Unlike other battery state estimation such as the state of charge (SOC) or state of power (SOP) estimation, the SOH estimation belongs to a parameter identification problem in long-term use [68]. In typical SOC/SOP estimation, cell capacity and internal resistance are considered as a constant for capacity or as a function of SOC and temperature for internal resistance, but not varying with aging. If a cell degrades in long-term use the changes in cell capacity and internal resistance due to aging can adversely impact on estimating the SOC and SOP. Therefore, together with the battery SOC, SOP, and internal temperature, the battery SOH is one of the critical functionalities for battery management systems.

However, direct measurement of these cell-level SOH parameters is generally challenging because cells are rarely fully charged and discharged in practice. Instead, these parameters are esti-

mated from available measurements, such as cell voltage, current, and surface temperature. There have been several methods proposed for battery SOH estimation, which can be generally grouped into three categories: empirical model-based, electrochemical model-based, and data-driven approaches.

Firstly, equivalent-circuit models (ECMs) are the most common type of empirical modeling approach, which does not consider fundamental physics. The ECM uses circuit elements (e.g. voltage source, resistor, and capacitor) to predict the electrical behavior of a Li-ion battery [57]. With a given ECM structure, observers can be designed to estimate model parameters such as cell capacity and/or internal resistance [48, 84, 41]. In [15, 104], a genetic algorithm (GA) and recursive least squares (RLS) are applied to identify ECM's parameters. On the other hand, empirical degradation models can be directly constructed using simple regression models with historical battery degradation data. Cordoba-Arenas *et al.* [20] proposed an empirical capacity fade model using a power-law relation with ampere-hour (Ah) charge throughput associated with the relevant aging factors such as charging rate, temperature, operating mode, and minimum SOC bound. Guha *et al.* [36] adopted linear and exponential functions as a basis function to build a fused degradation model and estimate the remaining useful life (RUL) of batteries. Similar empirical degradation models can be found in literature [92, 103, 77]

Another widely used approach is the use of electrochemical models that are based on the mathematical description of the underlying physics of a battery cell such as mass and charge transfer kinetics that are closely related to aging. Fuller *et al.* developed a detailed Li-ion cell model based on porous electrode and concentrated solution theories, Ohm's law, and intercalation kinetics [30]. Ning and Popov [70] proposed the single-particle model (SPM) for Li-ion batteries to model the cycle life of batteries. These models provide insights into key electrochemical mechanisms such as diffusion, migration, and reaction kinetics inside the cell. Specifically for battery degradation, solid electrolyte interphase (SEI) film growth is widely known as the primary cause for capacity fade and impedance rise [102]. Reniers *et al.* provides a comprehensive comparison of mechanical-chemical degradation models for Li-ion batteries showing the impact of interplay of several degradation mechanisms in accelerating the overall degradation trend [85]. Electrochemical models are based on first principles and accurately covering a wide range of operations (e.g. up to 5C), but identifying a large number of model parameters is not an easy task [28] especially under real-world usage conditions, often making the electrochemical models intractable for onboard BMS.

Data-driven methods have been gaining more attention in battery SOH estimation with recent advancements in powerful machine learning algorithms and their model-free characteristics [56]. These data-driven methods take operational data and their corresponding SOH as input and output data and find a nonlinear relationship between them without first principles. Thus, these methods

require plenty of high-quality data for training, which is typically obtained in a laboratory setting. For instance, battery aging tests are standardized and performed consistently, and aging conditions such as current and temperature can be easily controlled. The ground truth battery SOH (e.g. cell capacity and internal resistance) is measured by conducting a characterization test. In literature, a variety of approaches can be found, such as support vector machine [112, 111], artificial neural network [43], and Gaussian process regression [110, 119]. Although the data-driven methods generally provide good estimation accuracy even with nonlinearity, it still has some issues in field applications such as data quality, missing features, and overfitting for the given training dataset.

1.2.2 Electrode-Specific Degradation Diagnostics

Compared to cell-level SOH estimation, relatively less attention has been given to estimation of the electrode-specific state of health (eSOH) inside the cell. Diagnosis of these degradation modes is performed by tracking changes in the electrode-SOH-related parameters (i.e. electrode capacity and utilization range), which are estimated from eSOH estimation techniques. In literature, existing approaches for eSOH estimation can be divided into two groups: 1) voltage fitting and 2) differential analysis.

Firstly, voltage fitting approaches use optimization algorithms such as nonlinear least-squares to find a parameter set that provides the best fit for the voltage curve between measured data and model prediction. Han *et al.* [37] proposed a battery model with electrode-specific parameters and identified those parameters by fitting the voltage curve using a genetic algorithm (GA). Birkl *et al.* [8, 7] performed degradation diagnostics by fitting the parameterized model to a measured low rate of pseudo-OCV data based on the model framework from [26].

On the other hand, differential analysis is another type of data-driven method that focuses on thermodynamic information from electrode materials. In this approach, an electrode-specific degradation diagnosis is performed by monitoring changes of distinct signatures in differential curves. The two most common types of differential technique are differential voltage (DV) analysis [11, 40, 109], and incremental capacity (IC) analysis [25, 3], which have an inverse relationship. The basic premise of differential analysis is that the valuable electrochemical features become noticeable in the differential data. The differentiation transforms voltage plateaus into clearly identifiable peaks in IC curves and valleys in DV curves. For example, a differential voltage curve can be obtained by taking a derivative of the voltage measurements with respect to capacity (i.e. dV/dQ vs. Q). Peaks in the DV curve (dV/dQ vs. Q) indicate phase transitions in the electrodes, whereas peaks in the IC curve (dQ/dV vs. V) represent the location of a phase equilibria [11]. Graphically speaking, IC curves are plotted to the cell voltage, which can be directly measured, whereas DV curves are plotted to the cell capacity, which is a secondary indicator that varies

with aging and loses reliability as a reference in the course of aging [26]. However, IC curves can be infinite due to division by zero in a two-phase equilibrium region for graphite versus Li. Furthermore, DV curves are more intuitive in analyzing each electrode's contribution graphically [11], since the contributions from the cathode and anode electrodes add linearly in DV curves.

The peaks in the DV curve are attributed to positive and negative electrodes by comparing them to half-cell data. Therefore, in differential analysis, the changes of local peaks in the differential curves are used to identify electrode-related degradation modes. To this end, very low rate charge/discharge currents (e.g. $C/20$ or lower) are typically used for quasi-equilibrium condition, as the peaks in the differential curves are more clear and the kinetic artifacts (e.g. polarization) are minimum.

IC/DV analysis is also a powerful tool for online SOH estimation [37]; it can be easily implemented in a BMS by measuring two quantities only, cell voltage and charge/discharge capacity. However, generally differential analysis is sensitive to measurement noise and sampling techniques. Especially, measurement noise can significantly deteriorate diagnostic accuracy when taking derivatives of noise. Therefore, data processing, such as smoothing and filtering, is recommended using moving average [11], Savitzky-Golay filter [91].

In summary, estimation of the electrode-specific state of health is essential in degradation diagnosis because it enables to maintain safe operation of Li-ion batteries and possibly to evaluate the accurate SOH of end-of-life batteries for second-life usage.

1.3 Contributions and Dissertation Organization

Based on the above summary and literature review, the following gaps have been identified in the practical aspect of implementing degradation diagnostics for Li-ion batteries.

- Electrode-specific degradation diagnostic approaches assume the invariant half-cell potential of individual electrodes with aging.
- A full-range of OCV measurements is rarely available in practice. With the limited data availability, the reliability of parameter estimation results needs to be considered.
- OCV-based eSOH estimations require low rate pseudo-OCV data (e.g. $C/20$), which is challenging in real-world applications due to the typical time constraints for data acquisition.
- Pure data-driven machine learning methods are often difficult to interpret the results because it does not use a first principle or physical knowledge.

The advancements contributed by this dissertation and relevant publications are summarized as follows:

In Chapter 3, a novel method for estimating the electrode-specific state of health under the consideration of positive electrode half-cell potential change is proposed. In the proposed method, the alignment of local peaks in the differential voltage curve are used to identify the contribution of individual electrodes to the cell OCV curve and the aged positive electrode half-cell potential is calibrated. The proposed method includes experimental data to provide valid estimates of the electrode parameters. The preliminary comparative fitting results were presented at the 2018 Dynamic Systems and Control Conference [53]. An article with the detailed algorithms and the calibration of the aged half-cell potential has been published in the Journal of The Electrochemical Society [54].

- S. Lee, J. B. Siegel, A. G. Stefanopoulou, J.-W. Lee, and T.-K. Lee, "Comparison of individual-electrode state of health estimation methods for lithium ion battery", in ASME 2018 Dynamic Systems and Control Conference, American Society of Mechanical Engineers Digital Collection, 2018.
- S. Lee, J. B. Siegel, A. G. Stefanopoulou, J.-W. Lee, and T.-K. Lee, "Electrode state of health estimation for lithium ion batteries considering half-cell potential change due to aging", Journal of The Electrochemical Society, vol. 167, no. 9, pp. 090531, 2020.

In Chapter 4, the reliability of electrode parameter estimation accuracy is analyzed with a focus on the limited data availability for the OCV of a cell. In this work, the Cramer-Rao Bound (CRB) and confidence interval are used for quantifying the estimate's error bound of the electrode parameters at different locations and sizes of the partial data window. It is demonstrated that the local slope of the half-cell potential of an individual electrode heavily influences on the identifiability of the corresponding electrode parameters. With the proposed method, a preferable data range is given for the required estimation accuracy. A preliminary identifiability study was presented at the 2018 American Control Conference [51], and detailed framework with numerical and experimental verification results were published in the IEEE Transactions on Industrial Informatics [52]:

- S. Lee, P. Mohtat, J. B. Siegel, and A. G. Stefanopoulou, "Beyond estimating battery state of health: identifiability of individual electrode capacity and utilization", in 2018 Annual American Control Conference (ACC), pp. 2288-2293, IEEE, 2018.
- S. Lee, P. Mohtat, J. B. Siegel, A. G. Stefanopoulou, J.-W. Lee, and T.-K. Lee, "Estimation error bound of battery electrode parameters with limited data window", IEEE Transactions on Industrial Informatics, vol. 16, no. 5, pp. 3376-3386, 2019.

In Chapter 5, a method to directly measure the equilibrium voltage of a battery cell is presented. The key idea is to allow bi-directional current applying (e.g. both charge and discharge pulses are available even when the battery is in charge) such that one can actively perturb a battery cell with a concatenation of charge and discharge pulses. By doing so, unlike the typical way of measuring the OCV of a cell waiting a long relaxation period when the terminal voltage reaches a steady-state, the proposed minimum-time current profile removes the relaxation period, and thus the total data acquisition time is reduced to less than half. A preliminary optimal control problem and the numerical solution was presented at the 2019 American Control Conference [50]. The theoretical analysis of the given minimum-time optimal control problem and the reformulated switching time problem with numerical and experimental validation results are submitted to a peer reviewed journal and under review:

- S. Lee, Y. Kim, J. B. Siegel, and A. G. Stefanopoulou, "Minimum-time measurement of open circuit voltage of battery systems", in 2019 Annual American Control Conference (ACC), pp. 884-889, IEEE, 2019.
- S. Lee, Y. Kim, J. B. Siegel, and A. G. Stefanopoulou, "Optimal control for fast acquisition of equilibrium voltage for lithium-ion batteries", Manuscript is submitted to a peer reviewed journal and under review.

In Chapter 6, the feasibility of the electrode SOH estimation is studied focusing on practical charging rates. Since the close-to-OCV data requires a very low rate (e.g. C/20 or lower) constant-current voltage measurement, it could limit the use of the electrode SOH estimation algorithm in real-world applications. In this work, first, the smoothing behavior of the peak in the differential voltage curve is analyzed with respect to increasing C-rate [66] and aging state. Since the peak is directly related to the graphite negative electrode, the peak smoothing at a high C-rate adversely affects the estimation accuracy for the electrode parameters. Secondly, the estimation of the internal resistance and its impact on the electrode SOH estimation accuracy is studied. At practical charging rates, pseudo-OCV data cannot be directly measured due to the overpotential from the internal resistance. Lastly, an adaptive algorithm that enables estimating the internal resistance and electrode parameter in a real-world battery usage scenario is proposed.

- P. Mohtat, S. Lee, J. B. Siegel, and A. G. Stefanopoulou, "Differential expansion and voltage model for Li-ion batteries at practical charging rates", Journal of The Electrochemical Society, vol. 167, pp. 110561, 2020.
- S. Lee, J. B. Siegel, A. G. Stefanopoulou, J.-W. Lee, and T.-K. Lee, "(tentative title) Peak behavior in differential voltage curve with increasing C-rates", Manuscript is in preparation.

In Chapter 7, two case studies are presented to show how physics can guide data-driven machine learning algorithms in battery degradation diagnostics and prognostics. The first case study is the electrode-specific degradation diagnostics using the generated aged data and electrochemical features extracted from the differential curves. In this example, the data-driven diagnostic model specifically benefits from training/testing dataset preparation and feature selection [49]. The second case study is about the early prediction of battery cycle life [101], where it only uses the first few cycle data to predict the lifetime of the battery down to end-of-life.

- S. Lee and Y. Kim, "Li-ion Battery Electrode Health Diagnostics using Machine Learning", in 2020 Annual American Control Conference (ACC), pp. 1137-1142. IEEE, 2020.
- V. Sulzer, P. Mohtat, S. Lee, J. B. Siegel, and A. G. Stefanopoulou, "Promise and Challenges of a Data-Driven Approach for Battery Lifetime Prognostics", arXiv preprint arXiv:2010.07460, 2020.

This dissertation is organized as follows. In Chapter II, a parametric OCV model is presented with individual half-cell potential functions. The OCV model parameters are electrode capacity and utilization range used for electrode-specific degradation diagnostics in the following chapters. Chapter III addresses an issue about half-cell potential change due to aging and its impact on electrode SOH estimation accuracy. An algorithm to use peak information in differential voltage curve to calibrate the aged positive electrode half-cell potential function is presented. Chapter IV discusses the estimation accuracy of the electrode parameters with a focus on partial data availability. With the findings from Chapter IV on the partial data window, Chapter V presents a method to move quickly to the desired OCV data range by allowing bi-directional charging and minimum-time optimal control. Chapter VI discusses the feasibility of the electrode degradation diagnostics under practical charging rates. An adaptive algorithm is presented explaining how to use the developed algorithm in a real-world battery usage scenario. Chapter VII discusses potential opportunities of the physics-guided machine learning for battery diagnostics and prognostics with two case studies. In this chapter, the machine learning algorithms are applied, focusing on how electrochemical knowledge can benefit feature selection and interpretation of the results. Finally, Chapter VIII summarized the main contributions of this dissertation and possible future extension.

CHAPTER 2

Li-ion Battery Models and Electrode-Specific Degradation Diagnostics

2.1 Introduction

To perform electrode-specific degradation diagnostics, relevant Li-ion battery models and corresponding electrode parameters are covered in this chapter. First, an overview of different Li-ion battery models are given with a focus on open-circuit voltage (OCV) of a cell, where the changes in the OCV curve with aging reflects the electrode-specific degradation. Diagnosis of the electrode-level degradation modes is performed by tracking changes in the electrode parameters, individual electrode capacity and utilization window. Estimation of these electrode parameters is formulated as a nonlinear least-squares problem and shown with an experimental result for a 5 Ah NMC/graphite pouch cell.

This chapter is organized as follows. Section 2.2 covers an overview of different Li-ion battery models. For electrode-specific degradation diagnostics, Section 2.3 presents an OCV model with the individual electrode potentials and their parameters, electrode capacity and utilization window. In Section 2.4, electrode-specific degradation diagnostics are presented based on changes in the electrode parameters. These parameters are identified using non-linear least squares for a Nickel-Manganese-Cobalt (NMC) oxide/graphite cell in Section 2.5. Finally, conclusions are drawn in Section 2.6.

2.2 Overview of Li-ion Battery Models

A variety of models have been proposed to predict the electrical, thermal, and mechanical responses of Li-ion batteries. These models are used not only to understand the internal dynamics of the battery systems but also to develop model-based estimation and control techniques.

The electrical behavior of Li-ion batteries, the most common type of battery response, is modeled with current and voltage as input and output response. The two existing approaches are equivalent-circuit models and electrochemical models, where the former is a phenomenological model, whereas the latter is a physics-based model. Equivalent-circuit models (ECMs) are widely adopted due to their simplicity and reasonable accuracy [57, 38, 42]. ECMs consist of electrical elements such as an OCV as a voltage source, an ohmic resistance, and one or more parallel resistor-capacitor pairs. The voltage source element OCV is characterized as a nonlinear static function of its state of charge (SOC) and temperature based on the slow rate charge and discharge voltage measurements. An ohmic resistance in series R_s explains an instantaneous cell's voltage drops when it is under load. The voltage of a cell also shows a dynamic response (non-instantaneous) to a step current or when it is allowed to rest, which are modeled with several pairs of parallel resistances and capacitances.

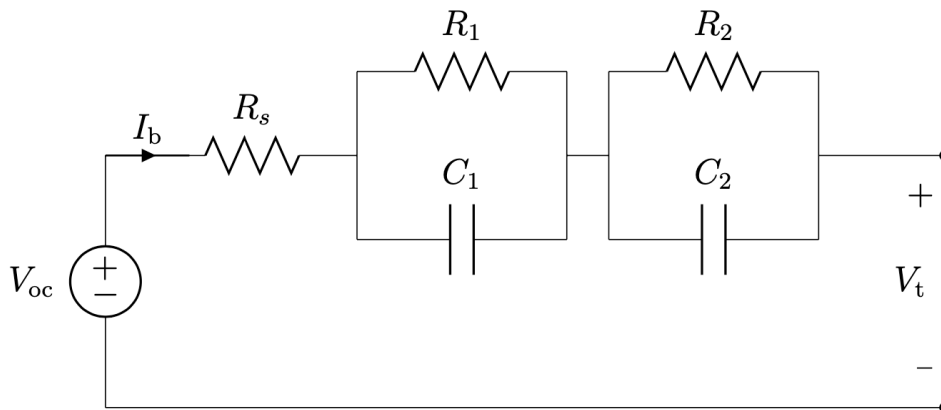


Figure 2.1: An example of the equivalent circuit model: OCV-R-RC-RC

On the other hand, to understand fundamental physics inside a battery cell, more complicated electrochemical models are used. The electrochemical models basically describe the distribution of lithium concentrations inside a cell. With a distribution of lithium, these models build their basis (equilibrium voltage, OCV) from each electrode's half-cell potential, which is a function of the normalized lithium concentration. When the current load is applied, overpotential is modeled on top of the OCV based on the porous electrode and concentrated solution theories, Ohm's law, and intercalation kinetics. Fuller *et al.* [30] developed a pseudo-two-dimensional (P2D) model assuming the electrode active materials as spherical particles across the electrode thickness. The developed model is capable of predicting the internal states of a cell, such as the distribution of lithium concentration, current, and potential in the solid and liquid phases. Although the P2D model provides very accurate model prediction as well as internal dynamics, the model complexity and resulting computational cost make this model difficult to be used in control applications. To

address the model complexity, many attempts have been made. Forman *et al.* [27] used quasi-linearization and Pade approximation of diffusion to decrease the complexity and numerical cost of the P2D model. In a different approach, Ning and Popov [70] proposed the single-particle model (SPM) for Li-ion batteries. The SPM assumes each electrode as a single-spherical particle with no electrolyte dynamics based on the uniform current distribution across both electrodes. Recently, there has been progress on extending the SPM to include electrolyte dynamics [35, 82].

Among these models, this dissertation focus on the physics-based model, starting from the OCV model for the electrode-specific degradation diagnostics. Generally, developing diagnostic tools based on the physics-based electrochemical model is challenging due to the complexity of the models [80]. To address this challenge, many researchers have focused on simple but accurate models at an equilibrium condition. Since the OCV is simply the potential difference between the half-cell potential of the positive electrode (PE) and negative electrode (NE), it provides a thermodynamic fingerprint of each electrode without complex electrochemical dynamics such as diffusion and lithium intercalation. Therefore, the OCV model presented here is composed of the half-cell potentials of both electrodes that can capture the changes of the OCV curve due to aging with the electrode parameters.

2.3 Open Circuit Voltage Model

The OCV is an important component of battery models as it contains information on the cell's SOC. As part of battery modeling, the OCV is typically parameterized as a function of SOC and temperature by fitting empirical functions to fresh cell's OCV data [113, 117]. However, since the degradation of Li-ion cells changes the cell capacity as well as OCV characteristics, we need an accurate but simple OCV model that can be used for the electrode degradation diagnostics. This section presents a parametric model for the OCV of the Li-ion battery cell based on two single electrode half-cell potentials. The OCV model developed in this chapter is the basis for diagnostic algorithms presented in Chapter 3 and Chapter 4, which identify and quantify the electrode-specific degradation modes (i.e. LAM and LLI).

2.3.1 Half-cell Potential Function

As the cell OCV is the potential difference between the half-cell potential of the two electrode, it can be written as follows,

$$V_{oc} = U_p - U_n.$$

where U_p denoting the positive electrode half-cell potential and U_n denoting the negative electrode half-cell potential.

The half-cell potential, also called open circuit potential (OCP), is the steady-state voltage of a half-cell consisting of one of the active electrode materials as a working electrode and lithium foil as a counter electrode. The potential of active materials varies with the extent of lithiation. Thus, the half-cell potential of an electrode is defined as a function of the Li stoichiometry. The measurement of the half-cell potential is performed on the fabricated coin cell by charging and discharging at a very low rate. The recorded voltage and cumulative Ah can be stored as a lookup table or used for curve-fitting based on different basis functions. In literature [97, 88, 79], a number of basis functions are presented for the development of the half-cell potential function for commonly used electrode materials. Common types of basis functions are exponential, hyperbolic tangent, polynomials, and cubic splines. However, these fits are all empirical modeling, which means they do not have physical relations. Karthikeyan *et al.* [47] and Birkl *et al.* [9] proposed a general fitting function with some theoretic interpretation based on Nernst equation [106]. One thing to note is that once the half-cell potential functions (U_p , U_n) are fitted, they stay fixed and are assumed not to change as the cell ages.

The basis functional form of NMC and graphite electrodes used in this work are:

- NMC, $U_p(y)$:

$$U_p(y) = a_0 + a_1y + a_2y^2 + a_3y^3 + a_4y^4 + a_5y^5 + a_6exp(a_7y + a_8),$$

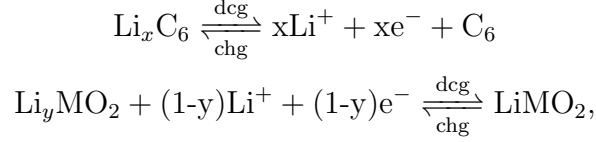
- Graphite, $U_n(x)$:

$$\begin{aligned} U_n(x) = & b_0 + b_1exp(b_2(x + b_3)) + b_4tanh\left(\frac{(x + b_5)}{b_6}\right) \\ & + b_7tanh\left(\frac{(x + b_8)}{b_9}\right) + b_{10}tanh\left(\frac{(x + b_{11})}{b_{12}}\right) \\ & + b_{13}tanh\left(\frac{(x + b_{14})}{b_{15}}\right) + b_{16}tanh\left(\frac{(x + b_{17})}{b_{18}}\right) \\ & + b_{19}tanh\left(\frac{(x + b_{20})}{b_{21}}\right). \end{aligned}$$

2.3.2 Parameterization with Electrode Parameters

This section describes the relationship of the OCV model and the electrode parameters that are related to the state of health of individual electrodes. For a Li-ion battery with lithium metal oxide $LiMO_2$ for the positive electrode (PE) and graphite C_6 for the negative electrode (NE), as a

cell is charging the normalized lithium concentration x in the graphite increases. This increase is balanced with a decrease in the normalized lithium concentration y in the metal oxide. Likewise, as a cell is discharging the forward reactions occur at each electrode as follows:



where forward reaction *dch* denoting discharge and backward reaction *chg* denoting charge of a cell.

The normalized lithium concentration is represented by x and y for each electrode. For example, a fully lithiated graphite anode is $x = 1$ for Li_xC_6 i.e., one lithium atom per six carbon atoms. When a cell is at equilibrium state, the terminal voltage of a cell is equal to the OCV, which is the difference between the half-cell potentials of PE ($U_p(y)$) and NE ($U_n(x)$),

$$V_{oc}(z) = U_p(y) - U_n(x), \quad (2.1)$$

where z is the state of charge of the cell.

In general, the battery manufacturer specifies the voltage limits to prevent overcharge or over-discharge:

$$V_{max} = U_p(y_{100}) - U_n(x_{100}), \quad (2.2)$$

$$V_{min} = U_p(y_0) - U_n(x_0), \quad (2.3)$$

where subscripts 100 and 0 indicate the utilization window of each electrode at upper and lower voltage limits, respectively. This utilization window is defined within a range of $[0,1]$ (i.e., $x \in [x_0, x_{100}] \subset [0, 1]$ and $y \in [y_0, y_{100}] \subset [0, 1]$).

As the cell SOC changes within the safe voltage limits, the normalized lithium concentration of individual electrode x and y change in a different ratio.

$$z = \frac{Q}{C} = \frac{y_0 - y}{y_0 - y_{100}} = \frac{x - x_0}{x_{100} - x_0}, \quad (2.4)$$

where Q is the charge Amp-hours (Ah) from fully discharged state found by coulomb counting and C denotes the cell capacity defined by the upper voltage limit, V_{max} , and lower voltage limit, V_{min} .

By defining the capacity of individual electrodes, C_p for PE and C_n for NE, we can write the

following equality equation for the cell capacity, C ,

$$C = C_p(y_0 - y_{100}) = C_n(x_{100} - x_0). \quad (2.5)$$

Combining Eq. (2.4) and Eq. (2.5), the normalized lithium concentration at each electrode can be written as a function of Q and the electrode parameters, $\theta = [C_p, C_n, y_0, x_0]$,

$$y = y_0 - \frac{Q}{C_p}, \quad x = x_0 + \frac{Q}{C_n}. \quad (2.6)$$

Finally Eq. (2.1) can be parameterized with the electrode parameters, electrode capacity and utilization window, $\theta = [C_p, C_n, y_0, x_0]$,

$$V_{oc}(Q; \theta) = U_p \left(y_0 - \frac{Q}{C_p} \right) - U_n \left(x_0 + \frac{Q}{C_n} \right). \quad (2.7)$$

Graphical interpretation of the OCV model is shown in Fig. 2.2. The upper utilization window of both electrodes y_0 and x_0 are aligned with the fully discharged state of the cell. The capacity of the individual electrode C_p and C_n scale the electrode half-cell potentials with respect to the cell capacity axis.

2.4 Electrode-Specific Degradation Diagnostics

For an aging diagnosis, we refer to commonly defined degradation modes: loss of lithium inventory (LLI) and loss of active material (LAM) at each electrode [26, 8]. LLI is the most common degradation mode for cell capacity fade where it represents irreversible lithium consumption from parasitic reactions such as surface film formation and lithium plating and the lithium loss associated with the loss of lithiated active materials. LAM indicates that active material is no longer available for lithium intercalation/extraction, which can occur at each electrode. Based on the associated electrode, LAM is further clustered into LAM_{PE} for positive electrode and LAM_{NE} for negative electrode. LAM_{PE} can be caused by structural disordering, metal ion dissolution, loss of electrical contact, and LAM_{NE} is due to particle cracking or the blocking of active sites by resistive surface layers.

Identification of an electrode SOH and its corresponding degradation mode is performed by tracking changes in the electrode parameters $\theta = [C_p, C_n, y_0, x_0]$ as a cell ages. A reduction in lithium inventory can describe LLI. At any DOD, total lithium inventory can be defined by the summation of lithium contents inside individual electrodes. Since x and y represent the degree of lithiation in the corresponding electrode, the lithium content in one electrode can be calcu-

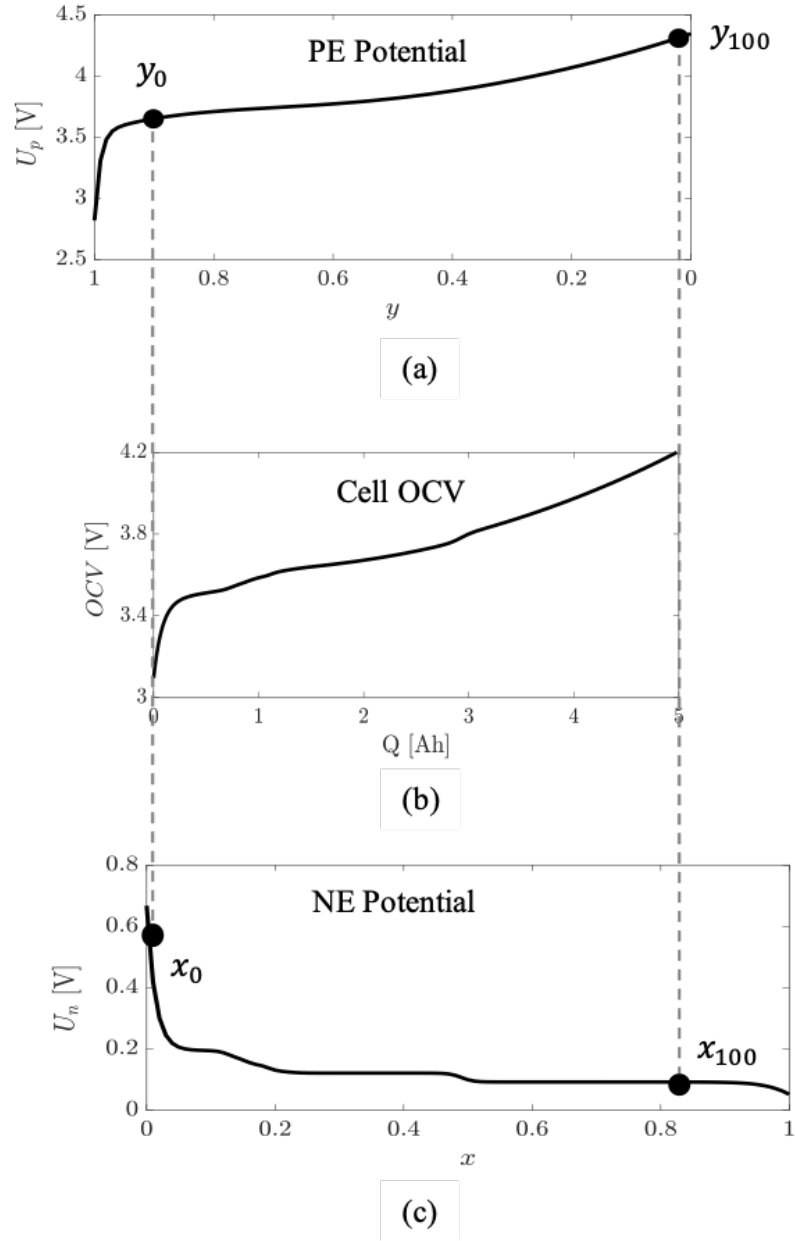


Figure 2.2: Open circuit voltage (OCV) of a cell aligned with the utilization window of individual electrodes. (a) half-cell potential of Nickel-Manganese-Cobalt (NMC) oxide positive electrode, (b) OCV of the full-cell with respect to the charge Ah Q , (c) half-cell potential of graphite negative electrode.

lated from multiplication of the normalized lithium concentration and the electrode capacity (e.g., $Li_{PE} = y \times C_p$). In this mode, the amount of intercalated lithium in both electrodes is given by

the following,

$$n_{Li} = \frac{3600}{F}(y_0 \times C_p + x_0 \times C_n). \quad (2.8)$$

Therefore, LLI is defined as the reduction in the above amount by

$$LLI = 1 - \frac{n_{Li}^a}{n_{Li}^f}, \quad (2.9)$$

where the superscript f represents the estimate from fresh cell and a for aged cell.

Similarly, the reduction in the electrode capacity C_p and C_n directly indicates LAM in each electrode as follows,

$$LAM_{PE} = 1 - \frac{C_p^a}{C_p^f}, \quad (2.10)$$

$$LAM_{NE} = 1 - \frac{C_n^a}{C_n^f}. \quad (2.11)$$

2.5 Experimental

2.5.1 Half-cell Potential Function Identification

To develop an OCV model, half-cell potential functions are firstly identified from coin-cells with electrode materials harvested from the $LiNi_{1/3}Mn_{1/3}Co_{1/3}O_2$ (NMC) /graphite full-cell. The electrode sheets were collected from the cell production line after going through the calendaring process. The active electrode material was coated on both sides of the current collector. To have a better electronic conductivity between the electrode and the coin cell base, the active material coated on one side of the electrode was carefully removed with N-Methyl-2-pyrrolidone (NMP), rinsed with dimethyl carbonate (DMC), and dried inside the glove box. Disks of 14 mm diameter were cut from the cleaned area of the electrode sheets using a puncher. The half-cell electrode disk was placed in a coin cell base (CR2032-type), followed by a glass fiber separator with the electrolyte ($LiPF_6$ solution in ethylene carbonate (EC) and ethyl methyl carbonate (EMC); 1 M $LiPF_6$ in EC/EMC = 30/70). Finally, lithium metal foil was used as the counter electrode, followed by a spacer, a spring for improved contact and the coin cell lid.

Initial formation cycles were performed for the coin cells. The NMC/Li coin cell was cycled at C/50 constant current between 2.8 V and 4.35 V for three times. Similarly, the graphite/Li coin cell was cycled at C/50 constant current between 0.005 V and 1.0 V for three times. The measurements from the last cycle were used for the half-cell potential function identification.

During the identification of half-cell potential function, the goodness of fit is determined based

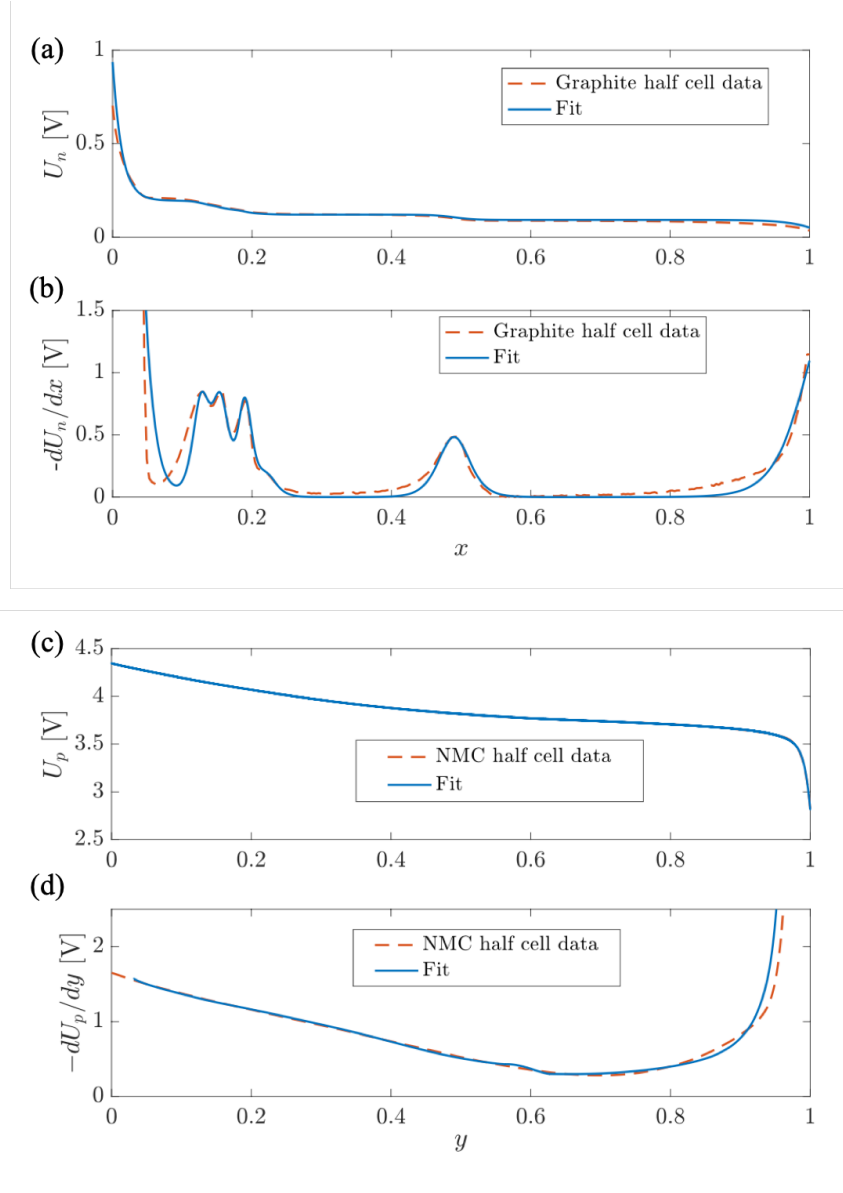


Figure 2.3: Half-cell potential of electrodes and their function fit. (a) The graphite half-cell potential and fit, (b) The differential voltage data and fit for the graphite/Li half-cell. (c) The NMC half-cell potential and fit, (d) The differential voltage data and fit for the NMC/Li half-cell.

on the error in voltage between the model and data as well as the agreement in the differential voltage curve for representing the phase transitions of electrode materials (e.g. graphite electrode). Fig. 2.3 shows the data and fit for graphite and NMC half-cell potentials, respectively. The data and model fit are in excellent agreement. Especially, distinct local peaks in the graphite differential voltage curve, so-called phase transitions, are well captured with the half-cell potential function, $U_n(x)$. On the other hand, the NMC electrode has a monotonic decrease as the stoichiometry y increases, showing no distinct peak in the differential voltage curve. These local peaks (i.e. phase

transitions) play a central role in the electrode-specific state of health estimation by providing distinct signatures in the cell differential voltage curve.

The identified half-cell functions are:

- NMC, $U_p(y)$:

$$U_p(y) = 4.345 - 1.652y + 1.623y^2 - 2.084y^3 + 3.515y^4 \\ - 2.217y^5 - 0.562e - 4\exp(109.451y + 100.006),$$

- Graphite, $U_n(x)$:

$$U_n(x) = 0.063 + 0.8\exp(-75(x + 0.001)) - 0.012\tanh\left(\frac{(x - 0.127)}{0.016}\right) \\ - 0.012\tanh\left(\frac{(x - 0.155)}{0.016}\right) - 0.004\tanh\left(\frac{(x - 0.220)}{0.020}\right) \\ - 0.010\tanh\left(\frac{(x - 0.190)}{0.013}\right) - 0.015\tanh\left(\frac{(x - 0.490)}{0.020}\right) \\ - 0.080\tanh\left(\frac{(x - 1.030)}{0.055}\right).$$

2.5.2 Electrode Parameter Identification

The full-cell used for the electrode parameter identification is pouch type 5 Ah NMC/graphite cells that were fabricated at the University of Michigan Battery Lab (UMBL). After the fabrication, the cells were cycled for initial formation to ensure stabilization of the cell. The detailed specification is shown in Table 2.1.

The identification of electrode parameters is conducted via a non-linear least-square optimization with the OCV measurement of the full-cell. The cell was cycled at C/20 rate constant current to approximate the OCV measurement. Since the cell operates between the predefined voltage limits, V_{max} is used as an equality constraint in Eq. (2.12b), which provides additional information to find the unknown parameters. Then, from the OCV model in Eq. (2.7), the least-square problem is formulated with an equality constraint to find the electrode parameters, $\theta = [C_p, C_n, y_0, x_0]$ as follows.

$$\underset{\theta}{\text{minimize}} \quad \sum_{i=1}^n \|V_{oc}(Q_i; \theta) - V_{oc,i}^{data}\|^2 \quad (2.12a)$$

$$\text{subject to} \quad V_{max} = U_p(y_{100}) - U_n(x_{100}). \quad (2.12b)$$

Table 2.1: The NMC/graphite pouch cell specification.

Full-cell (pouch type)	
Nominal capacity	5.0 Ah
Operating voltage	3.0-4.2 V
Thickness	4.0 mm
Length	132 mm
Width	90 mm
Positive electrode	
Material	NMC:CB:PVDF (94:3:3)
Number of double sided electrode sheets	14
Negative electrode	
Material	Graphite:PVDF (95:5)
Number of double sided electrode sheets	15
Separator	
Material	Polyethylene (PE)
Electrolyte	
Material	1 M $LiPF_6$
Organic solvent in electrolyte	2% EC:EMC (3:7)

The minimization problem is solved by using the *fmincon* function in MATLAB. Due to the nonlinearity of the OCV model, the parameter identification problem becomes a non-convex optimization problem with respect to the electrode parameters, thus local minima could exist. To find an optimum solution, multiple initial guesses are generated within feasible bounds for the electrode parameters and provided to optimization solver. A parameter set providing the smallest cost function value is determined as an estimate. For instance, out of 100 randomly generated start points, we have observed that 55 start points converged to the same solution providing the minimum function value. The feasible bounds were given for the electrode parameters $\theta = [C_p, C_n, y_0, x_0]$ that are $x, y \in [0, 1]$ and $C_p, C_n \in [C, 2C]$ (i.e. electrode capacity is typically larger than cell capacity).

The fitting results shows an excellent agreement in the full-cell with the RMSE of 5.4 mV. The alignment of local peaks between the data and model fit in the differential voltage curve in Fig. 2.4 indicates the correct identification of negative electrode parameters. The identified electrode parameters are summarized in Table 2.2.

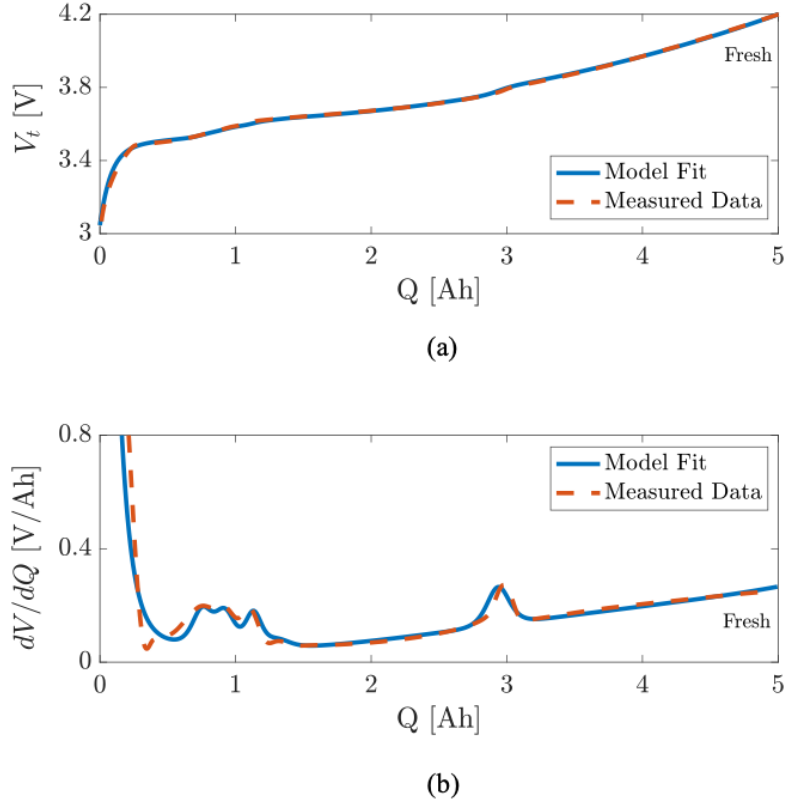


Figure 2.4: Full-cell C/20 data and the OCV model fit. (a) The voltage curve, (b) The differential voltage curve.

Table 2.2: The identified electrode parameters for fresh NMC/graphite pouch cell.

Parameters	Values
C_p	5.8 Ah
$[y_{100}, y_0]$	[0.03, 0.89]
C_n	6.0 Ah
$[x_{100}, x_0]$	[0.85, 1.4e-3]
$RMSE_V$	5.4 mV

This approach requires accurate knowledge of the half-cell potentials of both electrodes. In general, these half-cell potentials can be directly measured from coin-cell terminal voltage or found from literature. The coin-cell takes one of the electrodes as a cathode and a thin lithium metal as a reference electrode. In case the half-cell potentials are not accurate (e.g., cell- to-cell variance, aging), the model will cause additional error in the parameter estimation.

Furthermore, it is worth mentioning that the cell capacity C can be also estimated by incorporating the lower voltage limit V_{min} constraint. Once the electrode parameters are identified, it is possible to find a specific Amp-hours $Q = C$ that satisfies the lower voltage limit as shown below

$$V_{min} = U_p \left(\hat{y}_0 - \frac{C}{\hat{C}_p} \right) - U_n \left(\hat{x}_0 + \frac{C}{\hat{C}_n} \right). \quad (2.13)$$

Once the four electrode parameters and the cell capacity are identified, the utilization window of each electrode at the upper voltage limit can be estimated with the following relations:

$$\hat{y}_{100} = \hat{y}_0 - \frac{\hat{C}}{\hat{C}_p}, \quad (2.14a)$$

$$\hat{x}_{100} = \hat{x}_0 + \frac{\hat{C}}{\hat{C}_n}. \quad (2.14b)$$

2.6 Conclusion

In this chapter, a parameterized OCV model was presented with the individual electrode half-cell potentials, which is an accurate representation of the cell's OCV. The basis function for the half-cell potentials of the electrode materials were introduced with the literature review. Section 2.5 described the procedure of identifying the half-cell potential function from the coin cell measurement and their experimental preparation. Furthermore, the electrode SOH parameters, electrode capacity and utilization window, were identified for the 5 Ah UMBL NMC/graphite pouch cell with an excellent agreement. Lastly, Section 2.4 explained how the identified electrode parameters could be used for electrode-specific degradation diagnostics. With the proposed OCV model and framework for the electrode parameter identification, the baseline is established for the electrode-specific degradation diagnosis.

CHAPTER 3

Estimation Considering Positive Electrode Half-Cell Potential Change Due to Aging

3.1 Introduction

Estimation of electrode state of health (eSOH) is essential to understanding battery degradation status in detail. This is accomplished by considering electrode capacity and a utilization range as eSOH parameters. Several studies are available in the literature exploring eSOH estimation. Existing approaches can be divided into two groups: 1) voltage fitting and 2) differential analysis. The voltage fitting approach adopts optimization algorithms to find a parameter set that provides the best fit for the voltage curve between measured data and model prediction. On the other hand, differential analysis focuses on thermodynamic information from electrode materials. The basic premise of differential analysis is that the valuable electrochemical features become noticeable in the differential data (e.g. dV/dQ vs. Q). The peaks in the differential voltage curve are attributed to positive and negative electrodes by comparing them half-cell data. Therefore, the changes of local peaks in the differential curves are used to identify electrode-related degradation modes. It is noteworthy that the aforementioned conventional eSOH estimation approaches share a common assumption that the half-cell potential of an electrode (U_p or U_n) with respect to lithium concentration (stoichiometry y or x) is invariant to aging, but the electrode capacity and utilization window vary with aging.

In this chapter, a novel eSOH estimation method is proposed based on a hypothesis that the NMC positive electrode half-cell potential could change due to aging. The rationale for this hypothesis is supported by comparing the experimental results of eSOH estimation and findings from the literature.

3.2 Estimation of Electrode State of Health Parameters

In this section, eSOH estimation methods are presented with detailed algorithms. The OCV model developed in Chapter 2 is used for the estimation but with a change in the direction of Q from the charge Ah to the discharge Ah of the cell:

$$V_{oc}(Q; \theta) = U_p \left(y_{100} + \frac{Q}{C_p} \right) - U_n \left(x_{100} - \frac{Q}{C_n} \right). \quad (3.1)$$

where Q is the discharge Ah from fully charged state and the electrode parameters are $\theta = [C_p, C_n, y_{100}, x_{100}]$.

3.2.1 Conventional Voltage Fitting Method

Under the assumption of the invariance of the half-cell potential, parameters to be estimated are only the electrode capacity and utilization window, $\theta = [C_p, C_n, y_{100}, x_{100}]$. The identification of these parameters is finding the best reconstruction of the battery data, such as voltage or dV/dQ curves, with a given battery model and parameters, which is typically formulated as a nonlinear least-squares problem. The least-squares based voltage fitting (VF) approach has been commonly applied for battery parameter identification and degradation diagnostics [37, 8].

Algorithm 5 summarizes the detailed procedures. The electrode parameters $\theta = [C_p, C_n, y_{100}, x_{100}]$ are estimated by minimizing the summation of the squares of the voltage error between the model and measured data ($P1$). Cell voltage data can be measured from a low rate constant current (e.g. $C/20$ rate) as a pseudo-OCV, and it can be further processed with filtering and down-sampling using interpolation for computational benefit. Note that the optimization problem $P1$ has an equality constraint for the maximum voltage limit V_{max} , which results in providing additional information for estimating the parameters. In this work, *fmincon* solver with a sequential quadratic programming (SQP) algorithm in MATLAB is used to solve optimization problems ($P1, P2, P3, P4$).

Due to the nonlinearity of the OCV model, the estimation problem becomes a non-convex optimization problem with respect to the electrode parameters. Thus local minima could exist and optimization solution is affected by initial guess. In order to find an optimum solution, multiple initial guesses are generated within feasible bounds of the electrode parameters. Feasible bounds can be determined by assumptions or preliminary knowledge of cell parameters. The electrode capacities, C_p and C_n are designed to be larger than the cell capacity C . Typical energy cells have roughly 10% excess of negative electrode capacity than positive electrode capacity. The utilization window x and y are bound to be between 0 and 1 since those are the normalized lithium concentration of the individual electrode. This practice provides reasonable initial conditions for the unknowns. Once the electrode parameters are estimated, the cell capacity C is computed by

applying the minimum voltage limit V_{min} as explained in $P2$.

Algorithm 1: Voltage Fitting (VF)

Data : Discharge Amp-hours Q_i and cell pseudo-OCV $V_{oc,i}$ for $i = 1, \dots, n$

Model : OCV model V_{oc} in Eq. (3.1)

Estimate: Electrode parameters $\theta = [C_p, C_n, y_{100}, x_{100}]$ and cell capacity C

Procedure

- 1 **Preprocess** voltage data e.g., interpolation and filtering
- 2 **Generate** multiple initial guesses $\theta_0 = [C_p, C_n, y_{100}, x_{100}]_0$
- 3 **Estimate** the electrode parameters $\hat{\theta}$ by solving the following non-convex optimization problem,

$$\min_{\theta} \sum_{i=1}^n \|V_{oc}(Q_i; \theta) - V_{oc,i}\|^2. \quad (P1)$$

subject to $V_{max} = U_p(y_{100}) - U_n(x_{100})$.

- 4 **Estimate** the cell capacity C such that satisfying the lower voltage limit V_{min} constraint,

$$V_{min} = U_p \left(\hat{y}_{100} + \frac{C}{\hat{C}_p} \right) - U_n \left(\hat{x}_{100} - \frac{C}{\hat{C}_p} \right),$$

$$\min_C \|V_{oc}(C; \hat{\theta}) - V_{min}\|^2. \quad (P2)$$

- 5 **Estimate** the utilization range at fully discharged state (y_0, x_0) ,

$$\hat{y}_0 = \hat{y}_{100} + \frac{\hat{C}}{\hat{C}_p}, \quad \hat{x}_0 = \hat{x}_{100} - \frac{\hat{C}}{\hat{C}_n}.$$

Yet, besides the electrode parameters, another essential component in the OCV model is the half-cell potential of each electrode. With the assumption on the invariance of the half-cell potential of the electrode with respect to lithium concentration (i.e. $U_p(y)$ or $U_n(x)$), half-cell potential functions identified from fresh electrode materials are continuously used for electrode-level state of health estimation through the course of aging.

Generally, the invariance of a half-cell potential curve is a reasonable assumption. Experimental studies have shown no distinct changes in the half-cell potential curves with respect to Li

concentration for aged electrode materials of Li-ion batteries compared to pristine electrode materials. Authors in [62] compare the fresh and aged half-cell potentials of Lithium Iron Phosphate (LFP) positive and graphite negative electrodes and show no apparent changes. Especially for the graphite negative, it is shown in [10] that half-cell potentials (vs. Li) and differential voltage curves of unaged and aged anode materials are unchanged with respect to normalized Li concentration. Furthermore, based on this invariance assumption, many studies [37, 8, 7] have shown that eSOH estimation methods work well for aged cells. Although this is true for graphite and LFP, aging could influence the Nickel-Manganese-Cobalt (NMC) positive electrode half-cell potential, where the proposed method becomes crucial.

3.2.2 Proposed Peak Alignment Method

The overall flowchart of the proposed peak alignment method is summarized in Fig. 3.1. The proposed method is a refinement of existing approaches in that it combines least-squares voltage fitting and differential voltage analysis (DVA) for robust and accurate estimation. Furthermore, the proposed method is capable of identifying shape changes in the half-cell potential curve and calibrating the aged half-cell potential function when needed.

Electrode materials undergo several phase transitions during lithium intercalation, and their potentials show a staircase curve. Plateaus correspond to the coexistence of two phases, and steps between the plateaus represent the single-phase stage when the phase transition completes [21]. This sharp change at the step appears as a local peak in a differential voltage curve (dV/dQ vs. Q). Hence, a derivative of the voltage allows the electrochemical features to be seen clearly as peaks in the dV/dQ curve. Differential voltage analysis (DVA) uses the dV/dQ curve to identify the electrode-level degradation modes [11, 109]. Since OCV is the potential difference between two electrodes, electrode parameters can be identified by matching electrochemical features to corresponding electrodes. For example, a utilization window of the electrode is identified by aligning peak locations in the dV/dQ curve of the cell with respect to electrode's half-cell dV/dQ curve (i.e. dU_p/dy , dU_n/dx). The electrode capacity, C_p and C_n , are scaling factors that determine the ratio of the half-cell potential curve to the cell capacity axis.

Algorithm 9 presented here is formulated to utilize the graphite anode and its electrochemical feature (i.e. phase transitions). One of the key contributions of this method is that it allows PE parameter estimation to be successful using voltage fitting even when the PE material does not have distinct peaks to be used for the conventional DVA. As shown in Fig. 3.2(a), since NMC does not have distinct peaks, the peaks in the cell dV/dQ curve in Fig. 3.2(b) are all attributed to the graphite NE as shown in Fig. 3.2(c). Estimation of NE parameters uses this unique peak information (refer to Eq. (3.2)). Furthermore, aligning the local peaks (e.g. Q^1 and x^1) by shifting

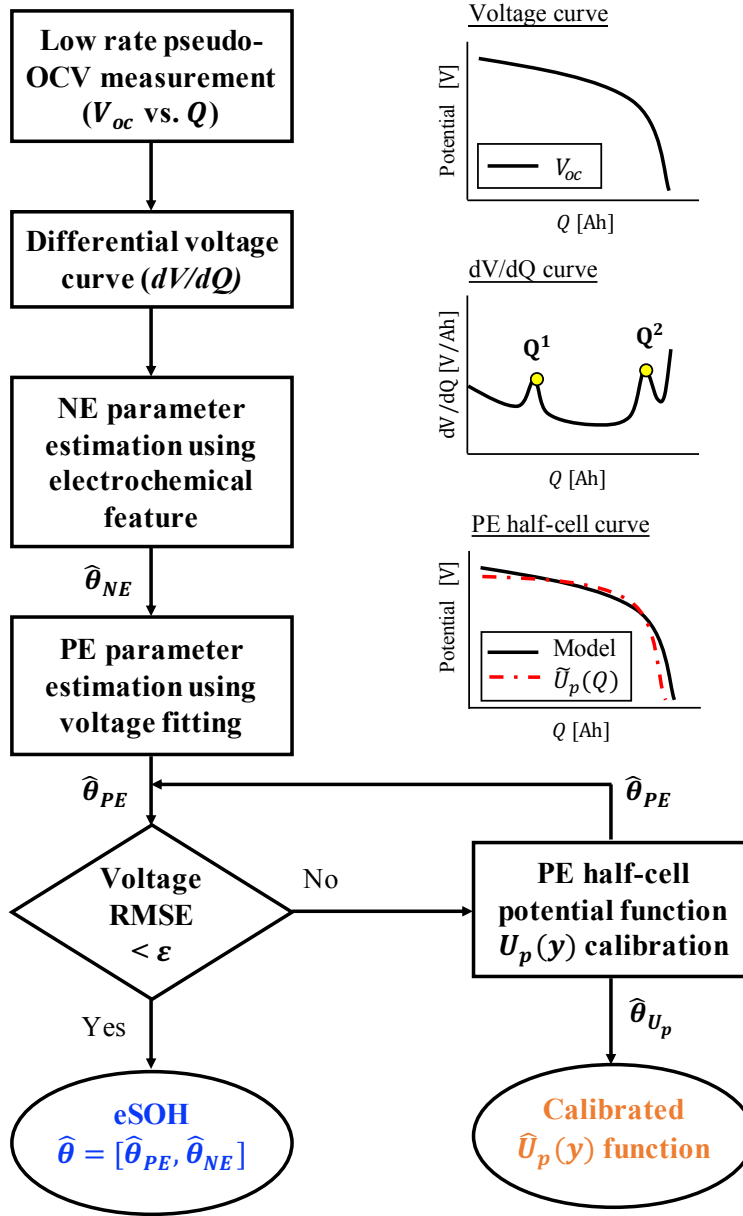


Figure 3.1: Flowchart for the proposed peak alignment method. The proposed algorithm is for an electrode-specific state of health estimation associated with the positive electrode half-cell potential change.

the scaled half-cell potential provides an estimate of the utilization window x_{100} . Identifying NE parameters allows the separation of the PE potential from the cell OCV by Eq. (3.3); then, the PE parameters are estimated by the least-squares based voltage fitting for the extracted PE potential $\tilde{U}_p(Q)$ as formulated in P3.

However, battery degradation can result from two different ways of variation in battery parameters. One is a quantitative change in lumped parameters such as cell capacity or electrode

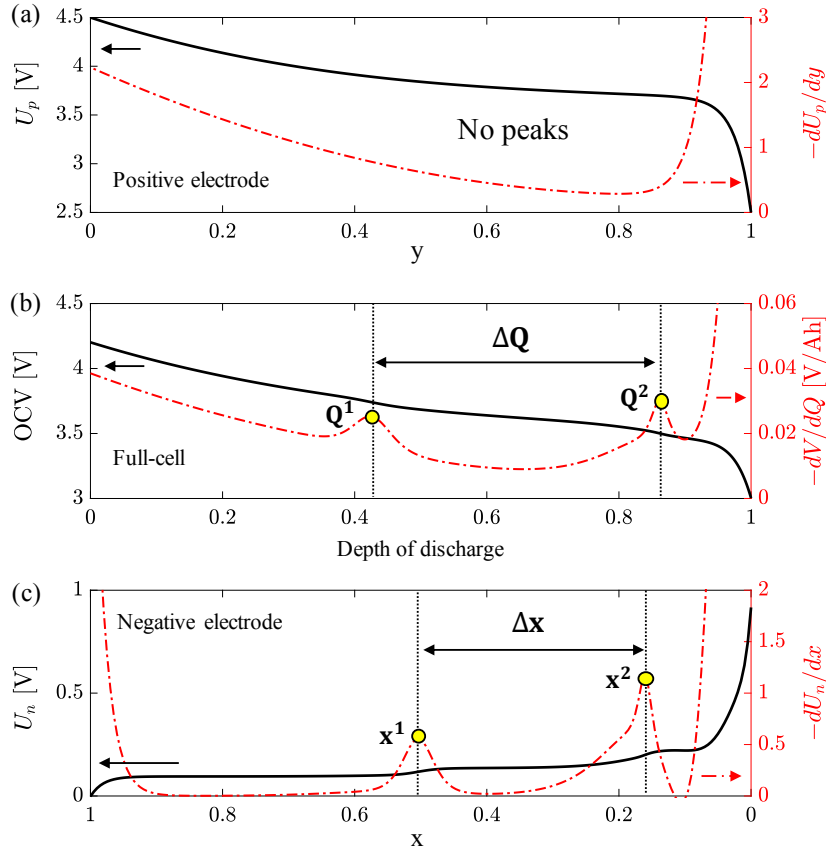


Figure 3.2: Voltage curve and differential voltage curve for an NMC/graphite cell. (a) NMC positive electrode, (b) full-cell, (c) graphite negative electrode

SOH (eSOH) parameters $\theta = [C_p, C_n, y_{100}, x_{100}]$. Changes, especially those in eSOH parameters are useful to identify the degradation modes of the cell, such as LLI and LAM. On the other hand, qualitative changes that can occur in an electrode active material structure could affect its electrochemical characteristics, including half-cell potential.

Changes in the half-cell potential profile of an electrode's material affect the accuracy of the eSOH estimation because conventional eSOH estimation methods use the half-cell potential function obtained from a fresh cell over the life of a cell. This is more likely to happen when the life of the aged cell is close to its end of life (EOL). Therefore, we need a method that can identify the qualitative degradation in the half-cell potential curve and calibrate it, if needed, as well as estimate the electrode state of health accurately. In this study, the assumption on the invariance of half-cell potential is relaxed only for the NMC positive electrode, not for the graphite negative electrode. It is reported in the literature that a graphite anode does not show apparent changes from aging in the

half-cell potential profile [10, 62, 98].

The procedure of calibrating the PE half-cell potential function is explained in Algorithm 9: Peak Alignment (PA) - step 10. When the half-cell potential function becomes uncertain with aging, the fitting problem is extended to not only identifying the electrode parameters but also finding the half-cell potential function. To deal with this, the fitting parameters are now both the PE parameters θ_p and the coefficients of the half-cell potential function θ_{U_p} . Therefore, the solution of the optimization problem $P4$ includes an estimate of the PE SOH parameters $\hat{\theta}_p$ and the calibrated aged half-cell potential function $\tilde{U}_p(y)$. The half-cell potential function considered in this study for the NMC positive electrode is

$$U_p(y) = a_0 + a_1y + a_2y^2 + a_3y^3 + a_4 \exp(a_5y + a_6), \quad (3.4)$$

where $\theta_{U_p} = [a_0, \dots, a_6]$.

In solving $P4$, two additional constraints are considered here for $U_p(y)$ at $y = 0$ and $y = 1$ assuming the upper and lower voltage limits of the electrode material do not change at fully lithiated and delithiated states. In general, $U_{p,max}$ and $U_{p,min}$ are available from the literature reporting various half-cell potentials of positive electrode materials [79].

3.3 Experimental Results

In this section, the eSOH estimation results are compared for a fresh and an aged NMC/graphite cell using the conventional VF method and the proposed PA method. Since peaks in the cell differential voltage (dV/dQ) curve provide a proof of the correct alignment of the graphite negative electrode, the validity of the estimation results is checked by the alignment of the peaks in the dV/dQ curve between the measured data and model prediction.

3.3.1 Test Cell and Aging Condition

Samsung SDI's prismatic NMC/graphite cells were used. The half-cell potential functions of each electrode were characterized by coin cell measurements made with pristine electrode materials. Since the proposed PA method uses local peaks in the differential voltage curves, the graphite NE half-cell potential function considers the phase transitions; thus, it captures the two most apparent peaks in dU_n/dx curve, as shown in Fig. 3.2(c). For pseudo-OCV data for the cell, constant current discharge voltage data was measured at $C/20$ rate from the fully charged state at the upper voltage limits of 4.2V at 25°C.

Algorithm 2: Peak Alignment (PA)

Data : Discharge Amp-hours Q_i and cell pseudo-OCV $V_{oc,i}$ for $i = 1, \dots, n$

Model : Half-cell potential functions $U_p(y), U_n(x)$

Estimate: Electrode parameters; PE $\theta_p = [C_p, y_{100}]$, NE $\theta_n = [C_n, x_{100}]$, and cell capacity C

Procedure

- 1 **Preprocess** voltage data and get dV/dQ curve
- 2 **Locate** the distinct peak position Q^j from the cell dV/dQ curve where j is the peak number.
- 3 **Locate** the distinct peak positions x^k from the graphite NE differential voltage dU_n/dx curve where k is the peak number.
- 4 **Match** the pair of peaks Q^j from the cell with the corresponding peaks x^k from the NE (see Fig. 3.2),

$$(Q^1, x^1), (Q^2, x^2).$$

- 5 **Estimate** the NE parameters,

$$\hat{C}_n = \frac{|Q^1 - Q^2|}{|x^1 - x^2|}, \quad \hat{x}_{100} = x^1 + \frac{Q^1}{\hat{C}_n}. \quad (3.2)$$

- 6 **Extract** the PE utilized potential $\tilde{U}_p(Q)$,

$$\tilde{U}_p(Q) = V_{oc} + U_n \left(\hat{x}_{100} - \frac{Q}{\hat{C}_n} \right). \quad (3.3)$$

- 7 **Generate** multiple initial guesses $\theta_{p,0} = [C_p, y_{100}]_0$

- 8 **Estimate** the PE parameters θ_p by solving the following optimization problem,

$$\min_{\theta_p} \sum_{i=1}^n \left\| U_p \left(y_{100} + \frac{Q_i}{C_p} \right) - \tilde{U}_p(Q_i) \right\|^2. \quad (P3)$$

- 9 **Calculate** the root mean square error (RMSE) of the PE potential fit in P2.
-

9 Procedure (continued)

- 10 **If** PE Potential Fit RMSE > threshold, then calibrate the PE half-cell potential function $U_p(y)$ by refitting the coefficient of the basis function,

$$\min_{\theta_p, \theta_{U_p}} \sum_{i=1}^n \left\| U_p(Q_i; \theta_p, \theta_{U_p}) - \tilde{U}_p(Q_i) \right\|^2. \quad (P4)$$

$$\text{subject to } U_p(y=0) = U_{p,max} \ \& \ U_p(y=1) = U_{p,min}.$$

where θ_{U_p} are the coefficients of the PE half-cell potential function $U_p(y)$. (see Eq. (3.4)).

- 11 **Estimate** the cell capacity C such that satisfying the lower voltage limit constraint (see P2).;

- 12 **Estimate** the utilization range at fully discharged state (y_0, x_0) ,

$$\hat{y}_0 = \hat{y}_{100} + \frac{\hat{C}}{\hat{C}_p}, \quad \hat{x}_0 = \hat{x}_{100} - \frac{\hat{C}}{\hat{C}_n}.$$

Cycling test conditions that were conducted for inducing a specific aging path for the test cell are summarized in Table 3.1. The aged cell has 66% of cell capacity compared to the fresh cell, which is well beyond the typical definition of end of life (i.e. EOL is defined when the cell capacity has decreased by 20% from fresh status). Different rates of continuous charge/discharge currents have been applied to the test cell: 0.5C for charging and 1.5C for discharging between 15% to 95% SOC under the high temperature at 45°C. Note that there are more aged cells that have gone through similar aging conditions that produce similar estimation results. Thus, one aged cell case is presented in this section.

3.3.2 Fresh cell

The estimation results of fresh and aged cells are summarized in the following. In each figure, results obtained from the conventional VF method are plotted on the left column and the results from the proposed PA method are on the right side. At each row, voltage curves of the measured data and model prediction are plotted on top, dV/dQ curves are in the middle, and lastly, the utilized potentials of individual electrodes along with their estimated parameters are described at bottom. The estimated cell capacity C is compared to the measured $C/20$ discharge capacity, and its error is inside the parenthesis. Note that all capacity values are normalized by the fresh cell capacity C_{fresh} for clarity (i.e. $C = 1.00$ for the fresh cell).

Fig. 3.3 shows the result of the fresh cell case. First, the voltage curves of measured data and

Table 3.1: Test cells and aging condition

	Fresh Cell	Aged Cell
Capacity Retention	100%	66%
Operating Temperature	-	45°C
Cycling Current	-	0.5C/1.5C
SOC Swing	-	95%-15%

model fit are plotted in Fig. 3.3(a) and Fig. 3.3(b) along with the RMSE for the voltage. In the fresh cell case, data and model show an excellent agreement (i.e. the RMSE values are below 5 mV for both methods). The validity of the estimation result is tested by checking the alignment of the peaks in the dV/dQ curves as shown in Fig. 3.3(c) and Fig. 3.3(d). As can be seen in Fig. 3.3(c), the VF method does not guarantee a perfect alignment of the peaks (local peaks are a little off by 1.2% to the normalized capacity). This is because the VF method does not take peak information into account in parameter estimation. However, the VF method shows a reasonable alignment of the peaks in the dV/dQ curve for the fresh cell case.

The identified electrode parameters decouple individual electrode potentials, as shown in Fig. 3.3(e) and Fig. 3.3(f). The dashed line of each electrode potential represents the full range, and the solid line indicates the actual utilization range in the cell illustrated by $[y_{100}, y_0]$, $[x_{100}, x_0]$. The electrode capacities associated with the full range are of PE C_p and NE C_n , respectively. A typical battery contains an excess amount of electrode capacity over cell capacity, and NE has a larger capacity than PE. The slight misalignment in Fig. 3.3(c) explains the difference between the estimated parameter values from the two methods, but the difference is tiny that can be neglected.

Lastly, it is shown that the cell capacity is very accurately estimated, less than 0.1% error for both methods. Here, to maximize the estimation accuracy for electrode parameters, a full-range of C/20 discharge data is used, producing an accurate estimation of cell capacity.

3.3.3 Aged cell

The estimation results of the aged cell are summarized in Fig. 3.4. In estimation, the same OCV model is used (i.e. no changes in the half-cell potentials are considered). The RMSE values in Fig. 3.4(a) and Fig. 3.4(b) have increased in both methods, but the PA method shows a significant

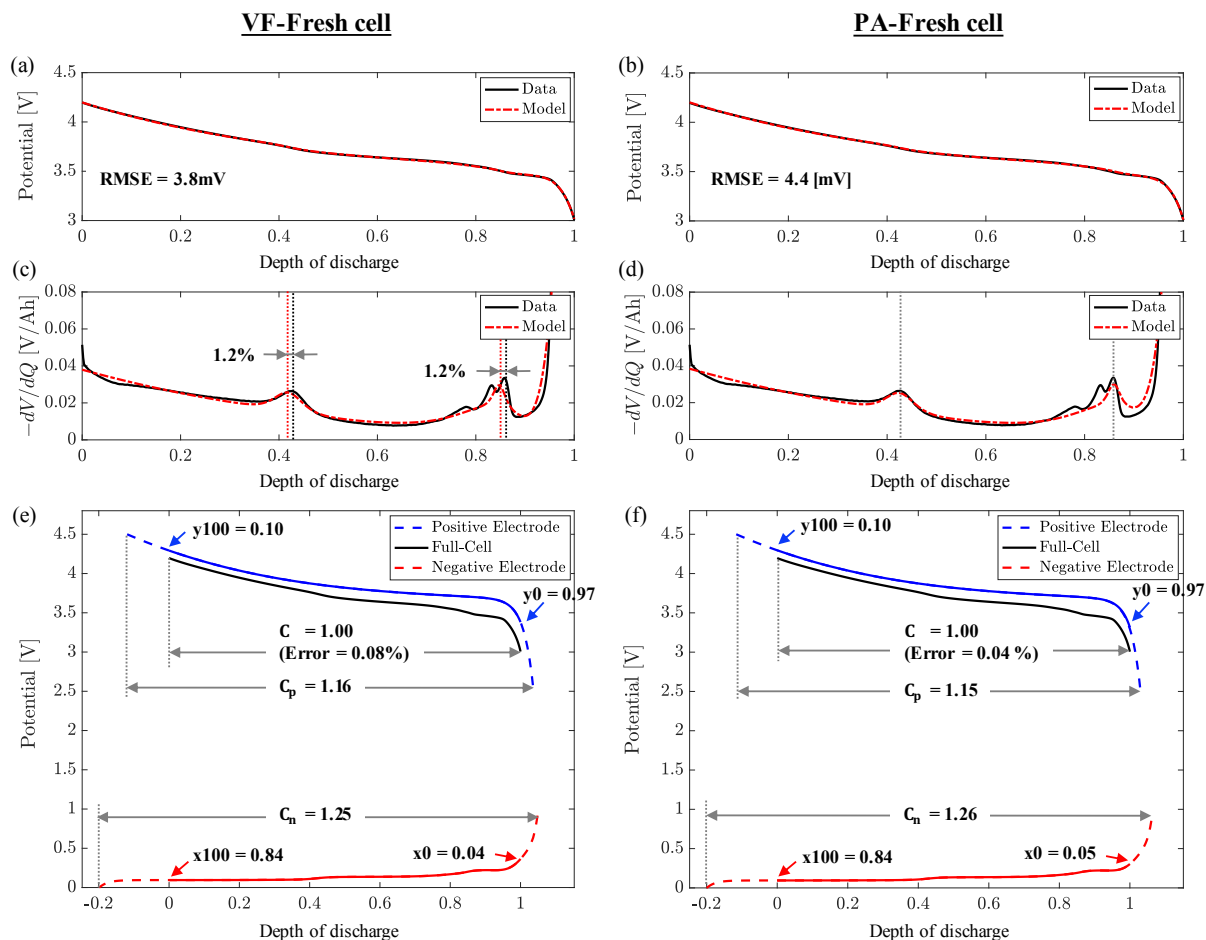


Figure 3.3: Results of the fresh cell from the conventional voltage fitting (VF) method and the proposed peak alignment (PA) method. (a)&(b) voltage curves, (c)&(d) differential voltage curves, (e)&(f) parameter estimates.

increase (from 4.4 mV at the fresh cell to 23.9 mV at the aged cell) while the VF method still shows a relatively good agreement between data and model. Even so, the VF method exhibits a substantial misalignment of the peaks in the dV/dQ curves in Fig. 3.4(c). The peak at higher SOC is drifted by 5.14% in the normalized cell capacity, even though the cell capacity is still estimated very accurately. Recall that the alignment of peaks implies the correct estimation of the NE contribution in the full-cell and the observed misalignment from the VF method indicates the estimation results are incorrect. To be specific, the NE capacity C_n shows a 17% discrepancy between the two methods, and consequently, the utilization range of the NE becomes considerably different. Note that the NE utilization at the fully discharged state x_0 is critical to identifying the utilized graphite anode potential, as can be seen in Fig. 3.4(e), the estimate from the VF method on $x_0 = 0.01$ corresponds to an abrupt increase of the graphite half-cell potential. This graphite

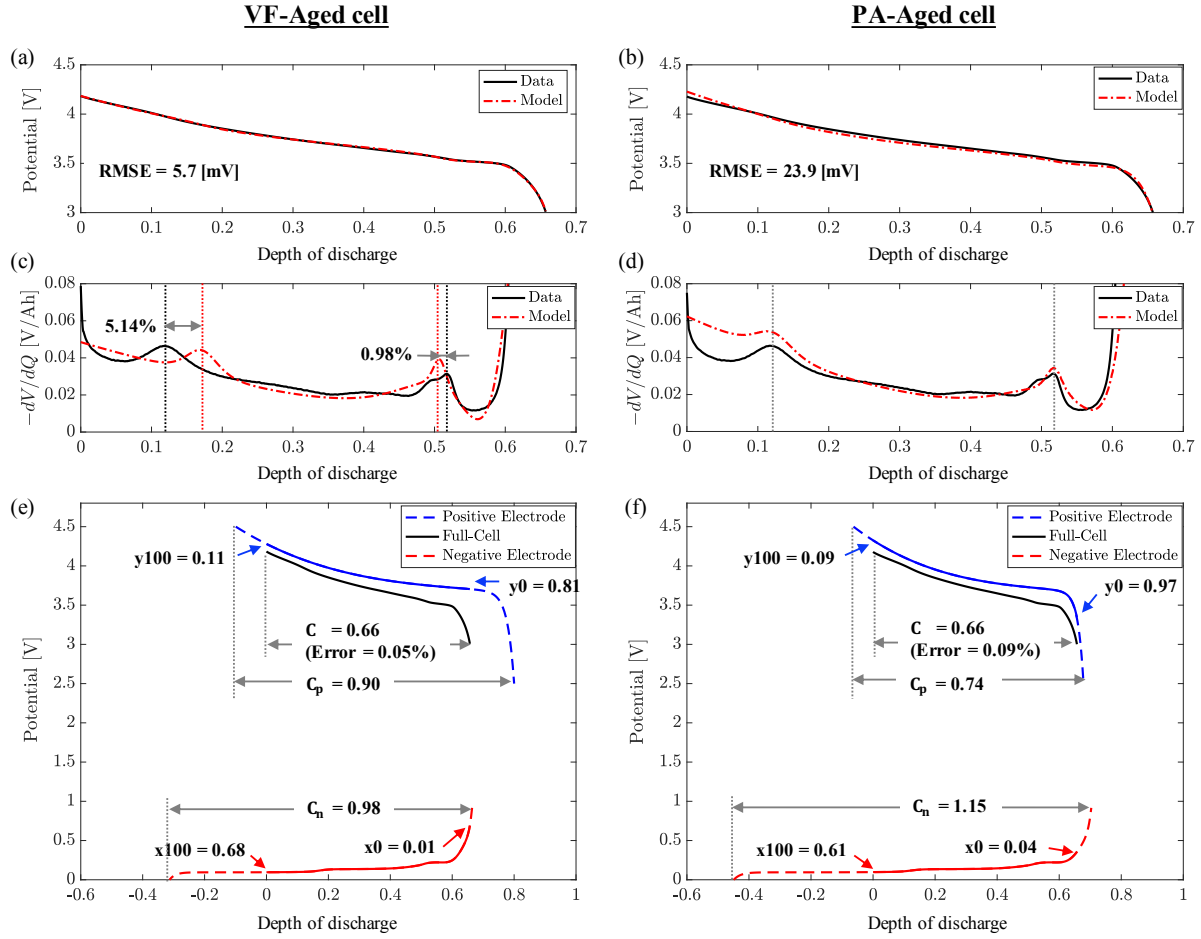


Figure 3.4: Results of the aged cell from the conventional voltage fitting (VF) method and the proposed peak alignment (PA) method. (a)&(b) voltage curves, (c)&(d) differential voltage curves, (e)&(f) parameter estimates showing a substantial disagreement between the two methods. Depth of discharge is normalized based on the fresh cell capacity.

potential attributes the knee of the NMC/graphite cell's OCV curve. Consequently, the identified NE shows a smaller utilization range and less capacity reduction in PE for the VF method, showing a 16% difference in the PE capacity C_p from two methods. Throughout this comparison, we find that a good agreement in the voltage curve (small voltage fit error), along with a precise cell capacity estimation from the conventional VF method, does not always promise an accurate electrode-specific parameter estimation.

On the other hand, in the proposed PA method (results are summarized in the right column of Fig. 3.4), the peaks are forced to be aligned between the measured data and model prediction. For this reason, the NE parameters can be accurately estimated using Eq. (3.2). The NE estimates imply the knee of the cell OCV curve comes from both electrode potentials, and leads to the

estimate of the PE capacity reduction by 36% from the fresh cell indicating LAM_{PE} as one of the main degradation modes. However, an obvious mismatch was observed in the dV/dQ curves around the high SOC region, as shown in Fig. 3.4(d) contributing a large voltage error. According to the PA method, once the NE parameters are identified the PE parameters $\theta_p = [C_p, y_{100}]$ are estimated by fitting to the extracted PE potential $\tilde{U}_p(Q)$ as described in P3. At this step, like conventional eSOH estimation approaches, $U_p(y)$ characterized by the fresh cell positive electrode material is used, assuming no change in the half-cell potential profile due to aging. However, it was not able to obtain a good fit in the voltage curve by only tuning the PE parameters $\theta_p = [C_p, y_{100}]$, which suggests another possible aging effect, i.e., change in the half-cell potential curve. In order to mitigate this mismatch, calibration of the half-cell potential function is further considered here.

3.3.4 Aged cell with Half-cell potential calibration

From the previous results, the invariance assumption of electrode half-cell potentials show limitations with aforementioned methods. Misalignment of the peaks is found in the VF method, indicating an incorrect electrode parameter estimation result. Substantial increases in voltage fit error are observed from the PA method without calibration. In order to rectify these shortcomings, we propose calibrating the half-cell potential function is proposed. With calibration, the refitted $\hat{U}_p(y)$ function is believed to reflect the changes in the half-cell potential profile due to aging, and consequently, these estimated PE parameters become more accurate than the case without such calibration. This refitted $\hat{U}_p(y)$ function is then fed to update the OCV model as well as the VF method. With this update, electrode parameter estimation results in Fig. 3.5 show an excellent agreement in the voltage curves between the measured data and model fit, and no more apparent mismatch is observed in the dV/dQ curves as well. Likewise, the estimated electrode parameters obtained from the two methods agree.

3.4 Discussion

The analysis of the aged cell shows that without considering the shape change of the half-cell potential, the VF method produced misalignment of the local peaks in the differential voltage dV/dQ curve, and the PA method showed an increased voltage fit error. This mismatch caused differences in the identified electrode parameters, thus making it challenging to analyze the electrode state of health accurately. In an ideal case, the two different methods have to provide the same results, such as in the fresh cell case.

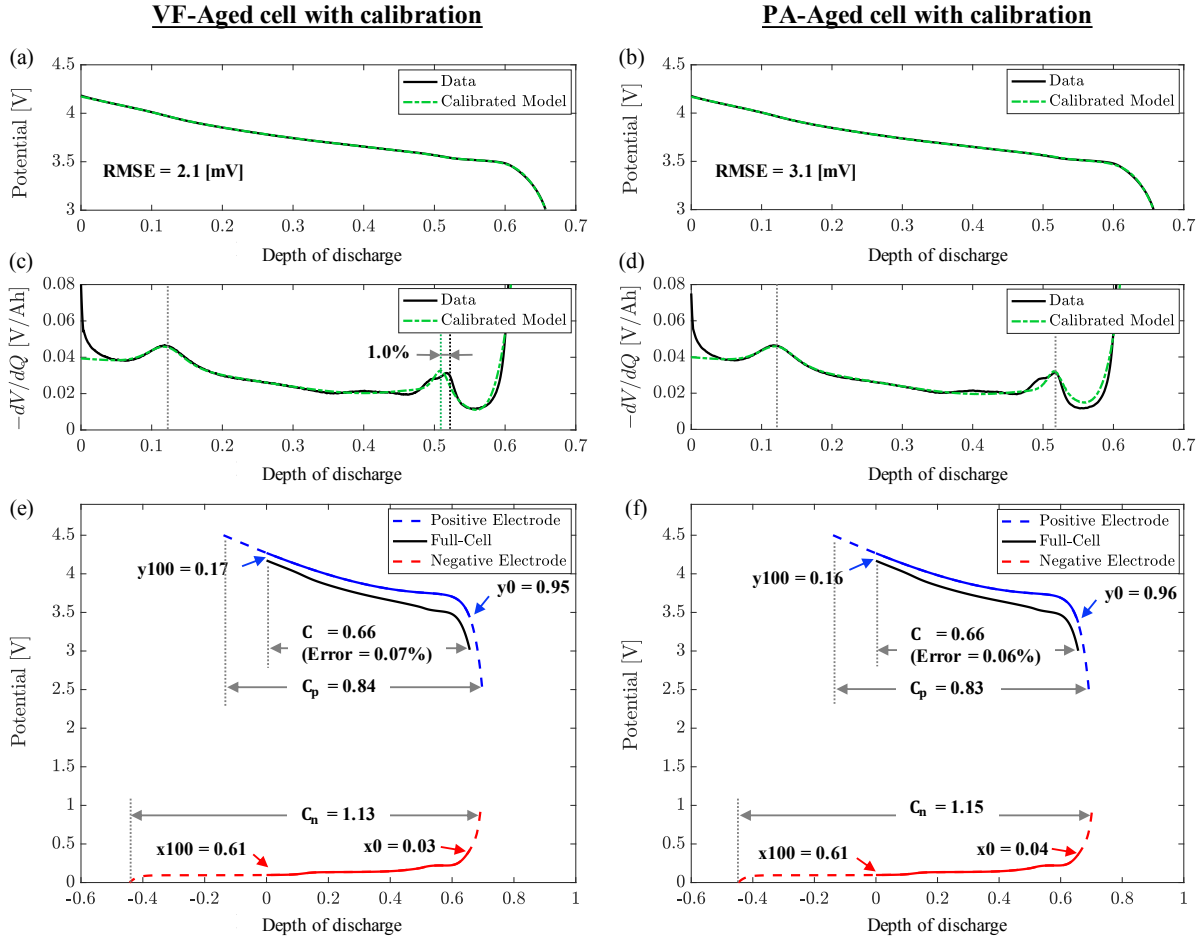


Figure 3.5: Results on the aged cell from the conventional voltage fitting (VF) method and the proposed peak alignment (PA) method after updating the positive electrode potential function $U_p(y)$ from the calibration. (a)&(b) voltage curves, (c)&(d) differential voltage curves, (e)&(f) normalized parameter estimates show excellent agreement in the results and verifying the proposed method. Depth of discharge is normalized based on the fresh cell capacity.

3.4.1 Half-cell potential change

What makes the proposed PA method superior to the VF method is that the PA method is capable of separating each electrode's potential from the full-cell OCV by utilizing its electrochemical features. With prior knowledge of the half-cell potential of the electrode materials, we can attribute the mismatch in the voltage curve, or the differential voltage curve, to the positive electrode half-cell potential for a cell composed of a graphite negative electrode. The separation allows for the calibration by re-fitting the coefficient of commonly used half-cell potential functions. After calibration, the two methods produce well-agreed upon results.

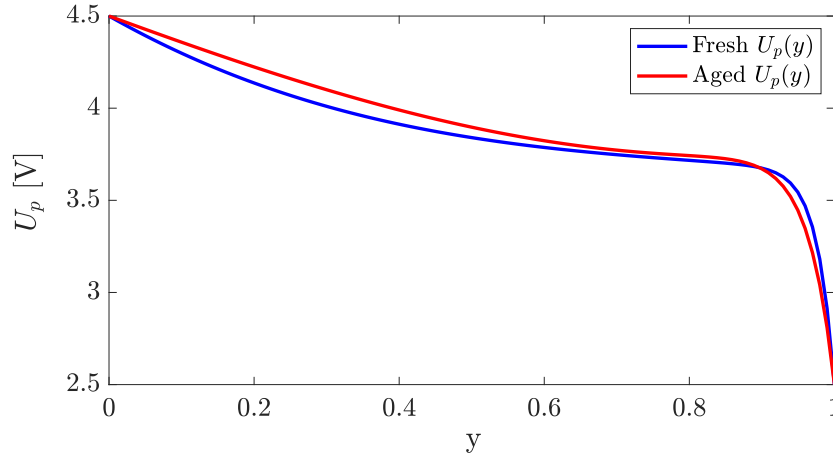


Figure 3.6: Positive electrode half-cell potential change is identified from the proposed peak alignment (PA) method with $U_p(y)$ calibration. Overall, the aged $U_p(y)$ is shifted up and to the left slightly.

It should be noted that the calibration of the half-cell potential is only considered for the NMC positive electrode, not for the graphite negative electrode. This selection is based on findings in the literature. Especially in the field of electrochemistry, the aging effect of various electrode materials has been extensively studied through experiments [115, 46, 62, 10, 98, 16, 124, 108, 96, 45]. One finding on the graphite anode in [10, 62, 98] is that, even with cycle-aging, it does not show apparent changes in the half-cell potential profile and peak locations in the differential voltage curve. On the other hand, transition metal (TM) dissolution is a well-studied degradation mechanism for cathode materials [16]. Moreover, as a cell composed of a NMC cathode degrades toward its end of life (EOL) from long-term cycling, degradation is accelerated due to the increased dissolution of its active material into the electrolyte at the high charge state [124]. More importantly, it is found in [108, 96, 45] that TM dissolution is accelerated at elevated temperatures as the test cells were cycle-aged under high temperature conditions. Other crucial degradation mechanisms for the cathode are structural disordering and surface film modification. Authors in [108] showed a significant lattice expansion for the thermally aged NMC cathode as well as SEI film thickness growth, indicating impedance rise of the cell. Therefore, assuming the invariance of half-cell potentials for eSOH estimation might not be valid for certain circumstances.

The calibrated PE half-cell potential curve is plotted in Fig. 3.6 showing the evolution of an aged half-cell potential curve. Compared to a fresh half-cell potential, the aged one is shifted up overall and slightly to the left. Specifically, the voltage curve above 3.8 V shows an upward drift. This overall shift of the average potential agrees with a study [33] on the aging pattern of a NCM/graphite cell.

3.4.2 Electrode state of health diagnostics

We can quantify the degradation of each mode and understand the impact of aging conditions to the degradation pathway associated with the identified electrode SOH parameters summarized in Table 3.2.

One of the most significant changes of the electrode parameters in Table 3.2 is a decrease of the PE capacity, C_p . This decrease indicates the loss of active material at the positive electrode, LAM_{PE} . Similarly, the utilization window of the negative electrode has changed by 28%, which is mostly attributed to the shifting of the upper utilization window, x_{100} , from 0.84 to 0.61. Loss of lithium inventory (LLI) requires computing the loss of the total amount of intercalated lithium in the electrodes. After such half-cell potential calibration, the voltage fit error (in RMSE) reduces to 3.1 mV from 23.9 mV using the proposed peak alignment method. Consequently, the half-cell potential calibration causes differences in the estimated parameters, especially of the PE parameters (i.e. electrode capacity C_p and utilization window $[y_0, y_{100}]$). However, the NE parameter estimation is robust in estimation since these are directly identified from the peak information (i.e. peak location and distance between two local peaks). As a summary of electrode state of health diagnostics, Fig. 3.7 presents the degradation of each mode obtained from the proposed PA method. For the selected NMC/graphite cell aged under a high operating temperature of 45°C, we observe 28% LAM_{PE} , 9% LAM_{NE} , and 28% LLI out of 34% of cell capacity loss.

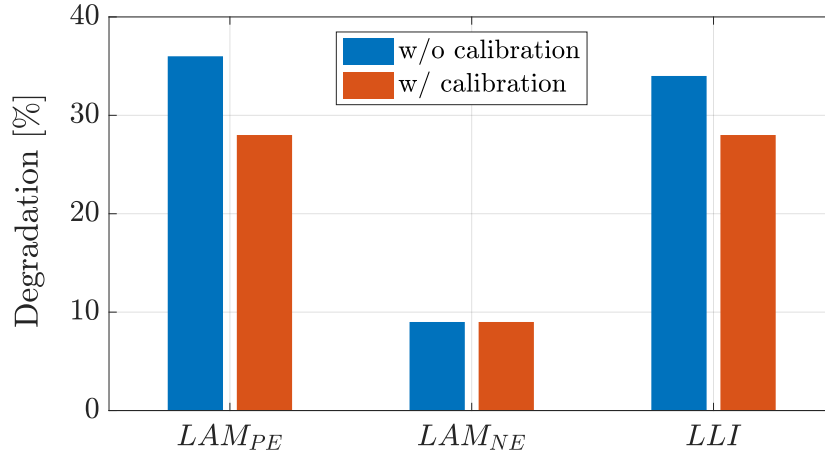


Figure 3.7: Electrode state of health (eSOH) diagnostic results with degradation modes. Quantification of each degradation mode is based on the estimated electrode parameters obtained from the proposed peak alignment method.

3.5 Conclusion

This chapter proposed a novel electrode state of health (eSOH) estimation method to overcome some limitations of the conventional approaches and provide accurate estimates. Some limitations of the conventional voltage fitting (VF) method are:

- no guarantee on the alignment of the peaks in the differential voltage curve, because the least-squares voltage fitting does not explicitly consider peak information.
- since the graphite negative electrode has a relatively low and flat voltage curve, it suffers poor identifiability in the electrode parameter estimation.

The proposed peak alignment (PA) method explicitly uses the peak information to estimate eSOH parameters for electrodes that have distinct local peaks in the dV/dQ curve. At the same time, it leverages the VF method for an electrode that has no peaks in the differential voltage curve. Moreover, the PA method is capable of separating the individual electrode potentials from the full-cell voltage measurement. For example, graphite negative electrode parameters can be directly estimated by scaling and sliding local peaks in the dV/dQ curve. Once the negative electrode is identified, the utilized potential of the positive electrode can be extracted by adding the cell pseudo-OCV (e.g. C/20 rate voltage measurement) and the identified negative electrode potential. Even if the positive electrode such as NMC does not have distinct peaks to be used, the proposed PA method still can estimate the positive electrode SOH parameters by applying the least-squares

fitting only for the extracted positive electrode potential. Therefore, this separation of individual electrodes enables the developed PA method to be more robust for electrode SOH estimation.

Table 3.2: The parameter estimates and their changes from the fresh to aged cells using the two methods

Parameter Estimates	Fresh Cell			Aged Cell			Aged Cell with Calibration		
	Voltage Fitting	Peak Alignment	Voltage Fitting	Peak Alignment	Voltage Fitting	Peak Alignment	Voltage Fitting	Peak Alignment	
C_p	1.16	1.15	0.90 (-22%)	0.74 (-36%)	0.84 (-28%)	0.83 (-28%)			
$[y_0, y_{100}]$	$[0.97, 0.10]$	$[0.97, 0.10]$	$[0.81, 0.11]$ (-19%, range)	$[0.97, 0.09]$ (+1%, range)	$[0.95, 0.17]$ (-10%, range)	$[0.96, 0.16]$ (-8%, range)			
C_n	1.25	1.26	0.98 (-22%)	1.15 (-9%)	1.13 (-10%)	1.15 (-9%)			
$[x_0, x_{100}]$	$[0.04, 0.84]$	$[0.05, 0.84]$	$[0.01, 0.68]$ (-16%, range)	$[0.04, 0.61]$ (-28%, range)	$[0.03, 0.61]$ (-28%, range)	$[0.04, 0.61]$ (-28%, range)			
C	1.00	1.00	0.66 (-34%)	0.66 (-34%)	0.66 (-34%)	0.66 (-34%)			
Voltage RMSE	3.8 mV	4.4 mV	5.7 mV	23.9 mV	2.1 mV	3.1 mV			
Peak Matching	aligned	aligned	misaligned	aligned	aligned	aligned			

CHAPTER 4

Estimation Accuracy with Limited Data Availability

4.1 Introduction

Advanced battery management system, which leverages an in-depth understanding of the battery state of health, can improve efficiently and safely. To this end, we introduce the electrode-level battery state of health (eSOH) estimation problem with open-circuit voltage (OCV) data. In real-world applications, collecting the full-range OCV data is difficult since the battery is not deeply discharged. When the available data is limited, the estimation accuracy deteriorates.

In this chapter, the uncertainty of the electrode parameter estimation is analyzed with a consideration of partial data availability using on the Cramer-Rao bound and confidence interval. By introducing a voltage constraint in the estimation problem, the positive electrode parameters can be estimated with sufficient accuracy over a wide range of SOC. However, the estimation accuracy of the negative electrode parameters is more sensitive to the depth of discharge. The proposed framework can be used as a guideline for selecting proper data windows and understanding the impact on parameter estimation.

This chapter is organized as follows. Section 4.2 presents the derivation of error bound for the electrode parameters using Cramer-Rao bound and confidence interval. In Section 4.3, analytic error bound calculation is summarized, and the results are validated over numerical simulation and experiment in Section 4.4. Conclusions are drawn in Section 4.5.

4.2 Methodology

4.2.1 OCV model and parameter estimation

In this chapter, the OCV model is written as a function of the discharge Amp-hours Q (or depth of discharge, DOD, depends on the normalization) with the electrode parameters (i.e., electrode

capacity and utilization range) $\theta = [C_p, C_n, y_{100}, x_{100}]$,

$$V_{oc}(Q; \theta) = U_p \left(y_{100} + \frac{Q}{C_p} \right) - U_n \left(x_{100} - \frac{Q}{C_n} \right). \quad (4.1)$$

The parameter estimation is formulated as a nonlinear least-squares problem shown in Eq. (4.2a) since the OCV model in Eq. (4.1) is a nonlinear static equation. The cell operates between the pre-defined voltage limits, thus V_{max} is used as an equality constraint in Eq. (4.2b), which provides additional information to find the unknown parameters. The impact of the equality constraint on the estimation accuracy will be discussed.

$$\underset{\theta}{\text{minimize}} \quad \sum_{i=1}^n \|V_{oc}(Q_i; \theta) - V_{oc,i}^{data}\|^2 \quad (4.2a)$$

$$\text{subject to} \quad V_{max} = U_p(y_{100}) - U_n(x_{100}). \quad (4.2b)$$

4.2.2 Error bound of parameter estimation

The purpose of the identifiability analysis is twofold. One is to address whether it is possible to determine unknown model parameters and, if it is observable, the second goal is to provide a measure of the reliability of the estimates out of the noisy measurements. The former is called structural identifiability analysis, which decides whether the model parameters are uniquely determinable based on the model formulation. This can be used to select a set of model parameters to be estimated based on ill-conditioning of the Fisher information matrix (FIM) [18]. The latter is known as practical identifiability, investigating whether the parameter value can be determined with precision, associated with limitations in the available data. In general, the goodness of fit does not guarantee how reliable the parameter estimates are. For instance, if the experimental data is very noisy or the number of data points is insufficient, the estimated parameter values could vary drastically without a significant difference in the goodness of fit. Therefore, providing a quantitative metric for the reliability of the parameter estimate is essential in parameter estimation.

Another use of the identifiability analysis is to evaluate a relative estimability between the parameters. As the typical number of unknown parameters is more than one, the notion of relative estimability is commonly used to partition a set of parameters to be estimated into several groups. In literature, sensitivity analysis and FIM are widely used [28, 122, 64, 72]. Suitable linear transformation of FIM reveals the linear dependence between parameters and enables grouping them for the best estimation strategy. As the linear dependence between the parameter sensitivity vectors makes the entire electrochemical parameter vector weakly identifiable [93], Park *et al.* [72] apply

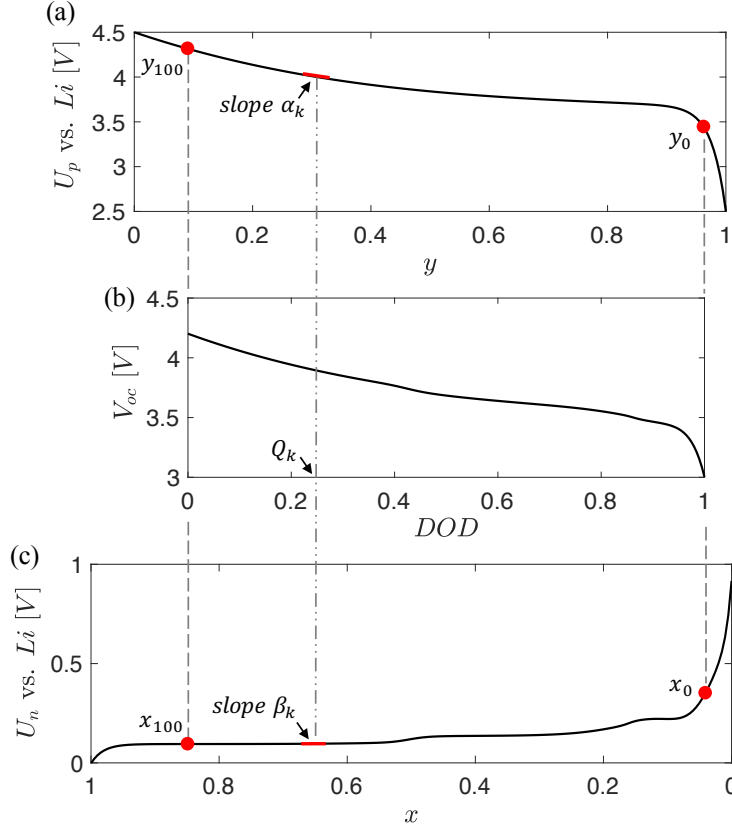


Figure 4.1: Half-cell potential of individual electrodes and OCV of a cell. The utilization range is denoted with $[y_{100}, y_0]$, $[x_{100}, x_0]$. (a) half-cell potential of Nickel-Manganese-Cobalt (NMC) oxide for the positive electrode, (b) cell OCV with respect to depth of discharge (DOD), (c) half-cell potential of graphite for the negative electrode. Local slopes of half-cell potential α_k, β_k are depicted associated with the cell DOD Q_k .

the Gram-Schmidt orthogonalization on FIM to reveal the linear dependence between the dynamical parameters and organize them into groups to avoid non-unique solutions during the parameter identification process. Similarly, Mohan *et al.* [64] propose an online estimator with a partitioning of battery states and parameters based on their relative significance on the measurement by applying principal component analysis (PCA) on FIM. The use of PCA on FIM allows us to quantify the reflection of the physical parameters to the principal components (PCs) and compute the relative significance. The proposed significance measure indicates the difficulty of estimating each parameter and is used to design a cascading structure of the online state-parameter estimator.

The PCA is commonly used for dimensionality reduction by projecting data points onto the first few orthonormal basis called principal components (PCs) that explain the majority of data variability. Essentially, PCA finds a new coordinate system based on the variance of data such that the largest variance comes to lie on the first coordinate, the second-largest variance on the second

coordinate, and so on.

As the inverse of the FIM is related to the lower bound on the covariance of the parameter vector (i.e. Cramer-Rao bound, CRB), one can find an interesting connection between PCA and FIM/CRB. In the process of principal component decomposition, eigenvectors of FIM and the diagonal matrix of corresponding eigenvalues are obtained. The eigenvectors or PCs of FIM represent linear combinations of physical parameters to be estimated from the data. And the corresponding eigenvalues reflect the variance of the sensitivity values along with the PCs. As the variance quantifies parameter estimation precision, the eigenvalues from the PCA on the FIM provide us information on which parameter can be determined with what accuracy from a given data set [69]. For instance, large eigenvalue means higher sensitivity of the corresponding parameter to the measured output such that small change of parameter is noticeable in the output measurement. Hence, the descending order from the largest eigenvalue to smallest eigenvalue explains the relative estimability of parameters.

In this work, the Cramer-Rao bound is used for quantifying the estimates' error bound for the electrode parameters. The error bound defined here is a quantitative measure for evaluating the relative identifiability of the parameters with respect to various data conditions. Note that the Cramer-Rao bound is the lower bound of the variance for any unbiased estimator, thus the error bound in this paper is the best-case scenario.

Suppose that a series of n observations $Y = [y_1, y_2, \dots, y_n]$, in our case the terminal voltage measurements of the cell, are represented by the statistical model

$$y_j = f_j(\theta_0) + \epsilon_j, \quad j = 1, 2, \dots, n \quad (4.3)$$

where f_j is the model in terms of the true parameter vector $\theta_0 \in \mathcal{R}^m$, in our case f_j is the OCV model in Eq. (4.1) and $\theta_0 \in \mathcal{R}^4$ represents the capacity and utilization range of the individual electrodes. It is assumed the observation error ϵ_j are independent and identically distributed random variables with a zero mean and variance $var[\epsilon_j] = \sigma_0^2$. Then, with a series of measured output, the least square estimator $\hat{\theta}_{LS}$ becomes also a random variable following a sampling distribution, and the uncertainty of the estimation can be quantified from this distribution. Nonlinear regression approximation theory [94] describes that the estimator $\hat{\theta}_{LS}$ approximately follows a Gaussian distribution as sample size increases (i.e., asymptotically) under several regularity conditions and sampling conditions are met [4]

$$\hat{\theta}_{LS} \sim \mathcal{N}_m(\theta_0, \sigma_0^2(\chi^T(\theta_0)\chi(\theta_0))^{-1}) = \mathcal{N}_m(\theta_0, \Sigma_0), \quad (4.4)$$

where $\chi_{ij}(\theta)$ is $n \times m$ sensitivity matrix with elements that corresponds to the sensitivity of the

measured terminal voltage on each of the electrode parameters,

$$\chi_{ij}(\theta) = \frac{\partial f_i(\theta)}{\partial \theta_j}. \quad (4.5)$$

Here, the true parameter θ_0 and the observation error variance σ_0 are unknown, the covariance matrix Σ_0 called unconstrained Cramer-Rao bound (CRB) must be approximated,

$$\Sigma_0 = F^{-1} \approx \Sigma(\hat{\theta}) = \hat{\sigma}^2 (\chi^T(\hat{\theta})\chi(\hat{\theta}))^{-1}, \quad (4.6)$$

where the matrix F is known as the Fisher information matrix and $\hat{\theta}$ is a parameter estimate obtained from the nonlinear least squares in Eq. (4.2a), and the approximation of the observation error variance $\hat{\sigma}^2$ of σ_0^2 is given by

$$\sigma_0^2 \approx \hat{\sigma}^2 = \frac{1}{n-m} \sum_{j=1}^n (f_j(\hat{\theta}) - y_j)^2. \quad (4.7)$$

Now, the sampling distribution of the estimator can be approximated with $\hat{\theta}$ as

$$\hat{\theta}_{LS} \sim \mathcal{N}_m(\theta_0, \Sigma_0) \approx \mathcal{N}_m(\hat{\theta}, \Sigma(\hat{\theta})). \quad (4.8)$$

Standard error (SE) to be used in the confidence interval calculation is defined as

$$SE(\hat{\theta}_k) = \left[\sqrt{\Sigma(\hat{\theta})} \right]_{kk}, \quad k = 1, 2, \dots, m. \quad (4.9)$$

Finally, since both θ_0, Σ_0 are unknown and approximated as Eq. (4.8), the approximate confidence interval is constructed with t -distribution [4]

$$\hat{\theta}_k - t_{1-\alpha} SE(\hat{\theta}_k) \leq \theta_k \leq \hat{\theta}_k + t_{1-\alpha} SE(\hat{\theta}_k), \quad (4.10)$$

where $t_{1-\alpha}$ is the critical value of the t -distribution with the confidence level $(1 - \alpha)\%$. The confidence level is the probability that the confidence interval contains the true parameter. Here, $t_{1-\alpha} = 2$ is used for 95% confidence level (i.e., $\alpha = 0.05$). Note that the interval in Eq. (4.10) is composed of the point estimate $\hat{\theta}_k$ and the margin of error that determines the uncertainty in the parameter estimation. Hence, the estimation error bound e_{θ} can be defined by the margin of error

$$e_{\theta_k}(\%) = t_{1-\alpha} \frac{SE(\hat{\theta}_k)}{\hat{\theta}_k} \times 100. \quad (4.11)$$

Observe that the SE term is divided by the least square estimate $\hat{\theta}_k$ for normalization, which enables the evaluation of the relative identifiability among all four electrode parameters.

If the estimation problem includes constraints to satisfy, the following procedure has to be additionally considered to determine the constrained CRB. The CRB under the parametric constraints can be found by a reparameterization of the original problem to remove redundancies in the parameter vector [99]. Consider a continuously differentiable constraint and its gradient matrix

$$h(\theta) = 0, \quad H(\theta) = \frac{\partial h(\theta)}{\partial \theta^T}. \quad (4.12)$$

If the gradient matrix $H(\theta)$ is full row rank, then one can find an orthogonal matrix U ($U^T U = I$) whose columns form an orthonormal basis for the nullspace of $H(\theta)$. That is

$$H(\theta)U = 0. \quad (4.13)$$

If $U^T \Sigma^{-1} U$ is nonsingular, then the parameters are identifiable and the constrained CRB (i.e., the error covariance matrix) can be obtained with some modifications,

$$\Sigma'(\hat{\theta}) = U(U^T \Sigma^{-1}(\hat{\theta})U)^{-1}U^T. \quad (4.14)$$

Then the SE term in Eq. (4.9) is recomputed with $\Sigma'(\hat{\theta})$ instead of $\Sigma(\hat{\theta})$. In our case the voltage limit constraint Eq. (4.2b) ties up the utilization range of each electrode (y_{100} and x_{100}). And the gradient matrix $H(\theta)$ is full row rank where the first and third column entries are the nonzero local slope of the half-cell potential,

$$\begin{aligned} H(\theta) &= \begin{bmatrix} \frac{\partial U_p}{\partial y} \cdot \frac{\partial y}{\partial y_{100}} & 0 & -\frac{\partial U_n}{\partial x} \cdot \frac{\partial x}{\partial x_{100}} & 0 \end{bmatrix} \\ &= [\alpha|_{y_{100}} \quad 0 \quad -\beta|_{x_{100}} \quad 0]. \end{aligned} \quad (4.15)$$

4.3 Results and Discussion

In this section, the error bound of each electrode parameter is presented, and the dependence on different data window is investigated. For simulation, nominal parameters in Table 4.1 are used. The electrode parameters are estimated by fitting the OCV model to the full range of voltage data for a 5 Ah NMC/graphite cell. The details can be found in the experimental validation section.

Table 4.1: Nominal parameters for the selected NMC/graphite cell

	Parameters	Values
Full-Cell	C	4.95 Ah
	V_{max}	4.2 V
	V_{min}	3.0 V
Positive Electrode	C_p	5.78 Ah
	$[y_{100}, y_0]$	[0.10, 0.95]
Negative Electrode	C_n	6.24 Ah
	$[x_{100}, x_0]$	[0.81, 0.02]

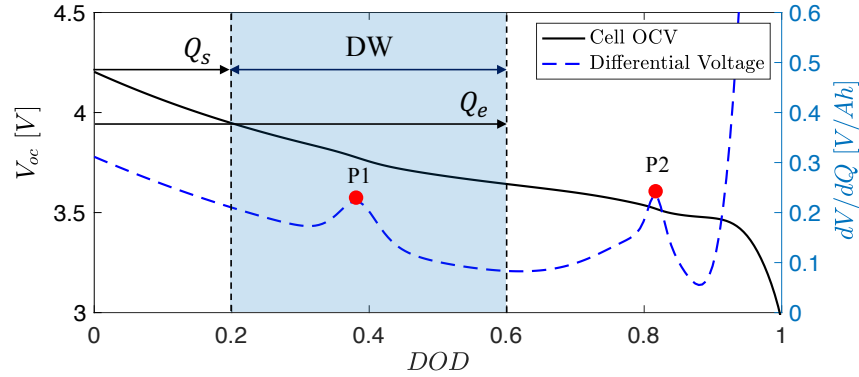


Figure 4.2: Definition of data window. Data window $DW = [Q_s, Q_e]$ of open circuit voltage (OCV) is illustrated with respect to depth of discharge (DOD) to represent when only partial OCV curve data is available for parameter estimation.

4.3.1 Data window

The concept of data window (DW) is defined to represent the partial availability of the OCV in the parameter estimation problem. Two points determine the location and size of the DW; starting-point Q_s and end-point Q_e of the window, i.e., $DW = [Q_s, Q_e]$, as shown in Fig. 4.2 by the blue shaded region. The differential voltage (dV/dQ) curve is plotted on the right side of the y-axis with the indication of the two distinct peaks representing the phase transitions of the graphite NE.

Various data windows are considered here with an assumption that the OCV data is partially available. For instance, if an electrified vehicle is used only for short commutes assuming full overnight charging is available, the battery would operate at high SOC range with small depth of discharge (DOD). Similarly, range anxiety tends to make battery electric vehicle (BEV) drivers

stay away from low SOC. Typical lower bound for the plug-in hybrid electrode vehicle (PHEV) is designed to be around 30% SOC of the battery to protect against over-discharge and possible degradation. Thus, four different DWs are defined for a quantitative identifiability analysis on the electrode parameters: DW-shallow, medium, non-full, and deep as shown in Fig. 4.3. DW-shallow represents the battery is used down to 80% SOC. DW-medium and non-full demonstrate 40% of the battery capacity usages but utilized at different locations in the OCV curve where the non-full represents not fully charged. Lastly, DW-deep represents almost full range of the OCV curve is available.

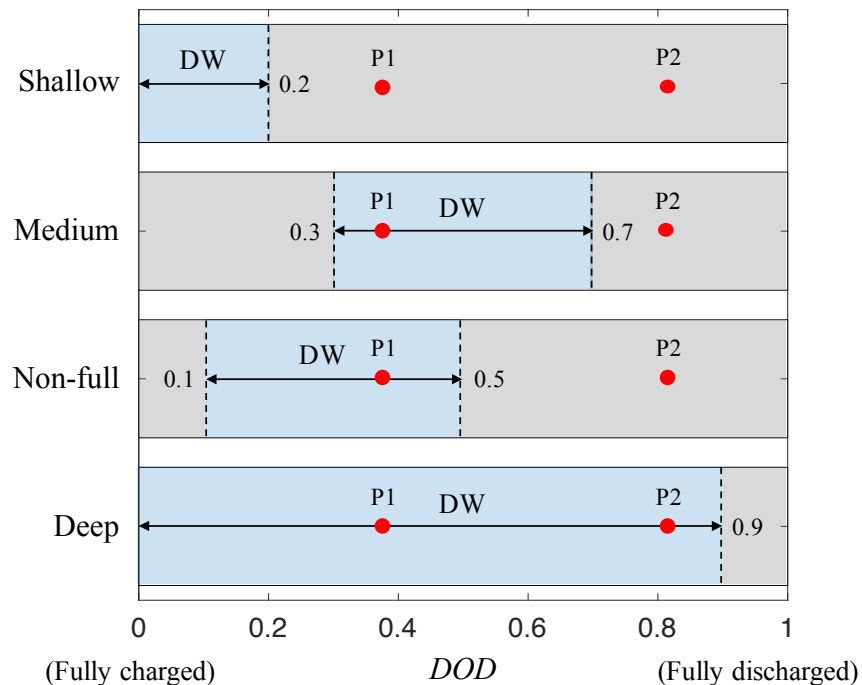


Figure 4.3: Data windows (DWs) for different battery usage patterns. The peak locations (P1, P2) are also depicted.

4.3.2 Analytic error bounds of electrode parameters

Here, the error bounds, of which the SE term in Eq. (4.9) is defined by either Eq. (4.6) for the unconstrained case or Eq. (4.14) for the constrained case, are computed for all combination of the sizes and locations of DWs. Since the starting and end-points are interchangeable and corresponding results are symmetric, the error bound results are drawn in a triangular-shaped plot with Q_s as y-axis and Q_e as x-axis in Fig. 4.4. It is assumed that the data points are evenly distributed with 0.5% DOD intervals and the observation error ϵ_j , Gaussian white noise with a standard deviation of 10 mV, is added. Note that the error bound is proportional to the observation error as shown

from Eq. (4.6) to Eq. (4.11), thus a larger measurement noise leads to larger error bounds making the estimation unreliable. A logarithmic scale color bar is adopted to highlight the transitions in the error bounds (e.g., the transition from the yellow to dark blue indicates a decrease of the error bound, and hence the more accurate estimation).

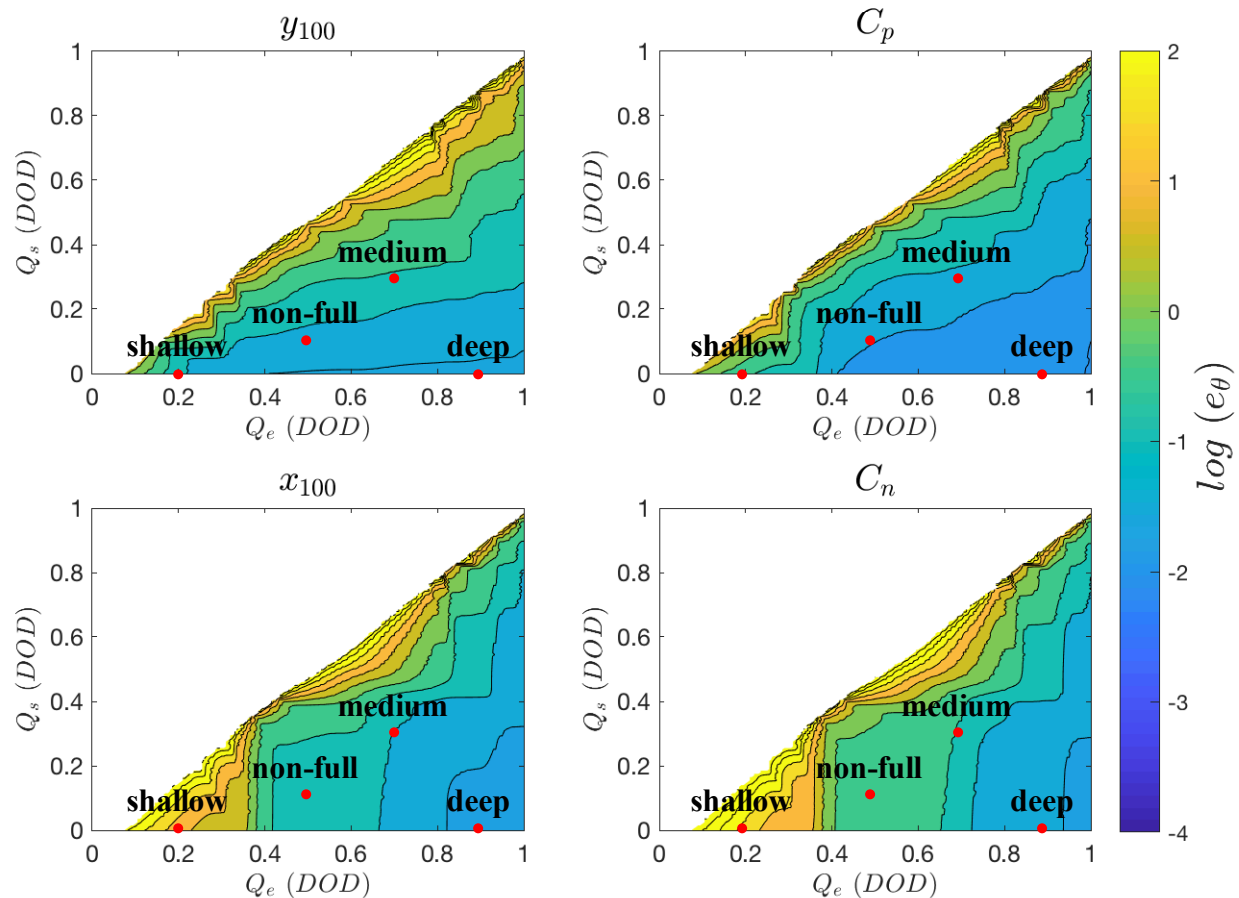


Figure 4.4: The analytic error bound of each electrode parameter in a logarithm scale. Triangular plots for the analytic error bound of each electrode parameter in a logarithm scale. Four predefined data windows are indicated by red dots. Data points are evenly distributed with 0.5% depth of discharge (DOD) intervals and noise standard deviation $\sigma = 10$ mV. No voltage constraint is considered.

In terms of the DW, size and location are essential. First, a large size DW provides a small estimation error bound and thus more accurate estimation can be achieved. Graphically speaking, as the DW becomes wider (i.e., $Q_s \rightarrow 0$ and $Q_e \rightarrow 1$), it approaches to right bottom corner in the triangular plot in Fig. 4.4 which indicates the small error bound. Furthermore, for a quantitative analysis, the error bounds of the four predefined DWs are summarized in Fig. 4.5. The results in Fig. 4.5 are from the unconstrained and constrained CRBs verifying the impact of the voltage limit constraint on the estimation accuracy. The unconstrained case is discussed first in the following.

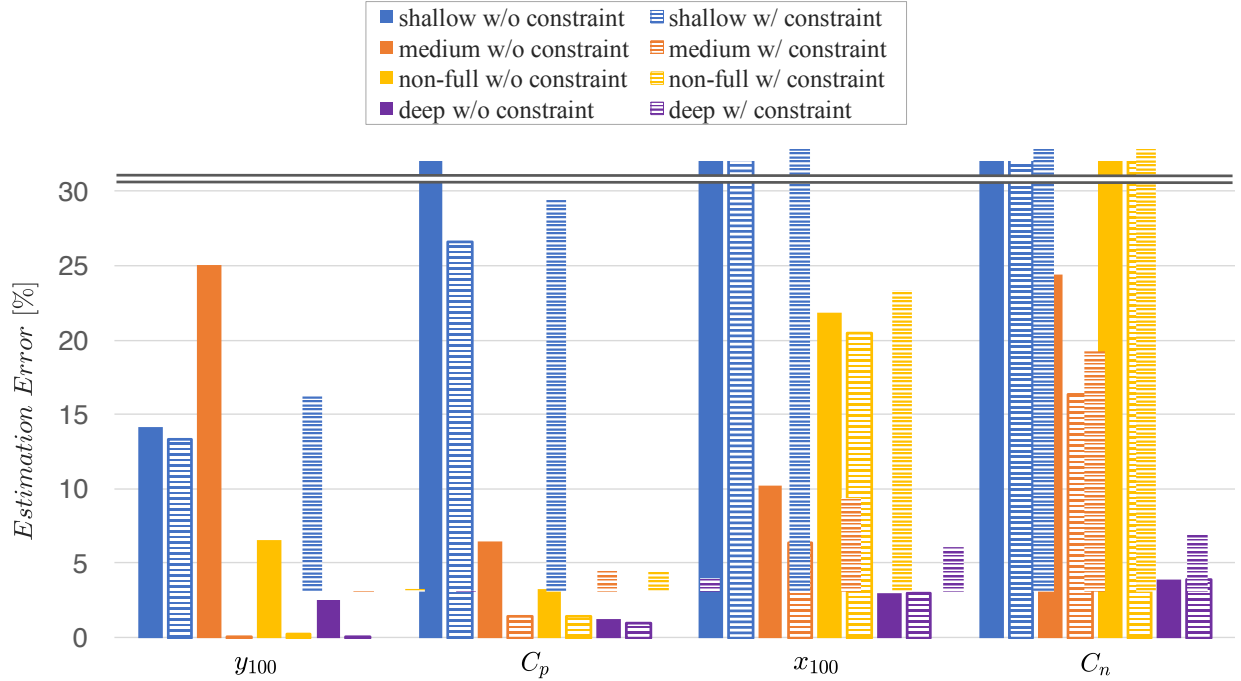


Figure 4.5: The analytic error bound of each electrode parameter for various data windows. Results of both unconstrained (solid) and constrained (stripe pattern) cases are shown. Voltage limit constraint improves all the electrode parameters, especially for the positive electrode parameters.

It is found that the half-cell potential slopes drives the identifiability of the electrode parameters. The cell with NMC/graphite chemistry, the NMC positive electrode (PE) potential has a relatively steeper slope than that of the graphite negative electrode (NE) potential, which suggests better identifiability of the PE parameters (y_{100}, C_p) than that of the NE parameters (x_{100}, C_n), e.g., the PE parameters show green color around the left bottom corner in Fig. 4.4, meanwhile the NE parameters show yellow color indicating the PE parameters have smaller error bounds than that of the NE. For the chemistry of LFP, it has a flat half-cell potential in the middle, thus when only the flat voltage portion is utilized in a certain data window the positive electrode parameters are not observable. Meanwhile, when it is utilized over the range for the given data window that includes the very top charge level or deep discharge level, also known as knee or shoulder of the potential, the abrupt slope change provides ample information and makes the parameter estimation feasible [51, 65]. This observation explains the poorer estimation error for the DW-shallow than the others. When only the upper 20% range of battery capacity is used, all electrode parameters are not identifiable because of a lack of information. Large errors (above 30% break line) are obtained, except for the PE upper utilization range y_{100} as shown in Fig. 4.5. Even more so, the NE parameters are almost not identifiable due to large errors for the DW-shallow and non-full cases. This becomes understandable when the battery is depleted to the low SOC area, such as the DW-medium and

deep cases where the NE half-cell potential increases and consequently the slope of the potential changes. Especially, for the DW-deep case, the utilized graphite anode potential rises significantly when the battery is almost fully depleted, making the estimation error of all electrode parameters less than 5%.

This improvement is also a benefit from the inclusion of the peaks inside the DW. As [51] explained, the slope change of the half-cell potential due to the phase transition improves the identifiability of the electrode parameters. Along with the phase transition, the potential undergoes a rapid change and results in the peak in the dV/dQ curve as shown in Fig. 4.2 that provides ample information on the associated electrode parameters. Therefore, having a data range that includes these peaks provides better identifiability. For the graphite NE, distinct vertical transitions are observed in the NE parameters (x_{100}, C_n) as the end point Q_e increases in Fig. 4.4.

In regard to the location of the DW, the comparison between two same size of DWs, DW-medium vs. DW-non-full. The non-full operates around a higher SOC region than that of the medium where the PE potential has a relatively steeper slope, hence it provides better identifiability of the PE parameters for the non-full than that of the medium case. Similarly, when the relatively low SOC region is utilized as in the medium case, the relatively steeper slope of the graphite NE provides better identifiability of the NE parameters in the medium.

4.3.3 Impact of voltage constraint

The optimization problem in Eq. (4.8) has a nonlinear equality constraint for the upper voltage limit. In this case, the constrained CRB is used for computing the error bound. The voltage constraint ties the upper utilization ranges of each electrode (y_{100} and x_{100}), which provides the parameter dependency between the positive and negative electrodes that reducing the number of unknown parameters and consequently improves the estimation accuracy (see Fig. 4.5; the error bounds of the PE parameters become significantly improved, especially the utilization range y_{100} becomes less than 0.3% for all the DWs except the DW-shallow case). Parameter dependency can be explained by using the Taylor series expansion of the voltage constraint about the nominal parameters,

$$\sigma_y \left. \frac{\partial U_p}{\partial y} \right|_{y_{100}} = \sigma_x \left. \frac{\partial U_n}{\partial x} \right|_{x_{100}}. \quad (4.16)$$

Comparing local slope of the half-cell potentials ($\alpha = \left. \frac{\partial U_p}{\partial y} \right|_{y_{100}}$ and $\beta = \left. \frac{\partial U_n}{\partial x} \right|_{x_{100}}$ in Fig. 4.1), β is smaller than α due to the flat voltage curve of the graphite NE. Hence, the error bound σ_x is larger than σ_y . Furthermore, since the parameters from the same electrode are correlated, the improvement in the estimation accuracy of y_{100} is beneficial to the estimation accuracy of C_p as

well. More clear effects of the size of the data window and the peak information can be found in Fig. 4.6. Here, the estimation error bounds of each electrode parameters are plotted with respect to DOD. All of the error bound decreases as more data points are included in the DW, which indicates the impact of the provided information on the estimation accuracy. Moreover, the error bound decreases with the transition around the peaks. Especially, the estimation error bounds of the PE parameters show a sharp transition at P1 location, $DOD = 0.4$. Similarly, the transitions occur at both peak points for the NE parameters. Since the slope of the graphite NE potential starts to change before P2 location, the transitions of the error bound in the NE parameters occur around $DOD = 0.7$.

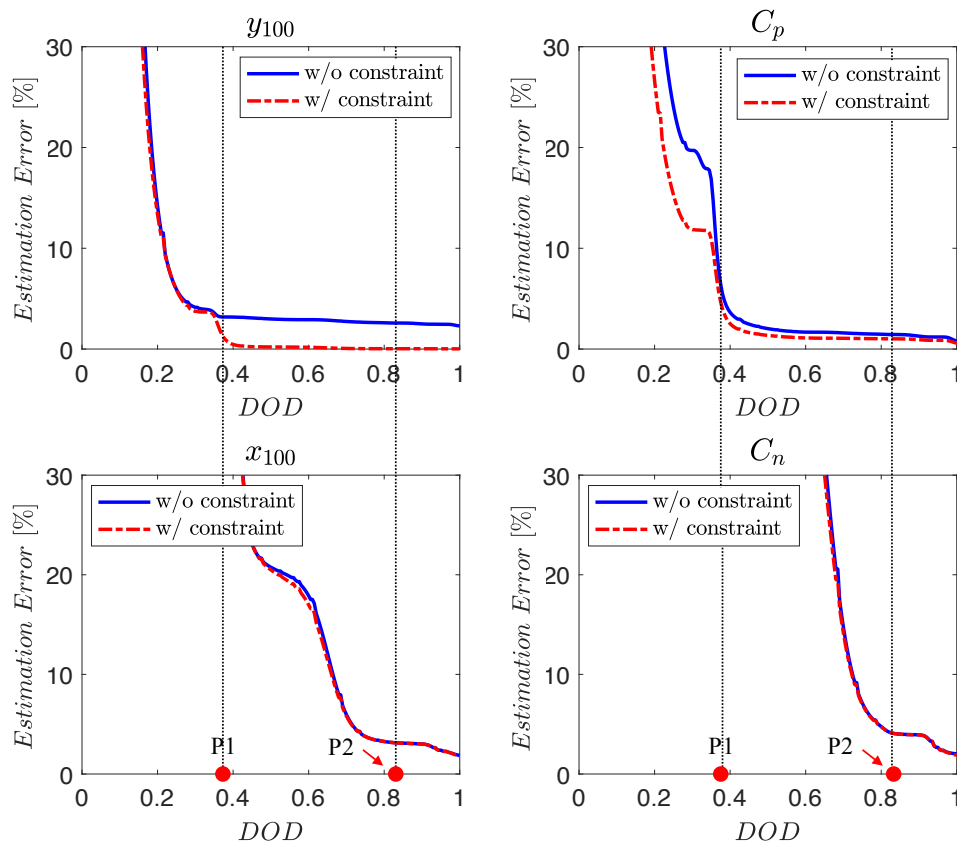


Figure 4.6: Analytic error bound with respect to depth of discharge (DOD). As the size of data window increases, the error bound decreases with transitions around the peaks (P1, P2).

4.4 Validation

4.4.1 Numerical validation

Given the error bound based on the CRB, this section presents numerical simulation results obtained from a Monte Carlo simulation (MC) to verify the analytic derivation. The parameter estimation has been repetitively conducted for 1,000 times for both the unconstrained case and the constrained case. The voltage data is simulated by the OCV model in Eq. (4.1) with the nominal electrode parameters in Table 4.1 and the additive zero-mean Gaussian voltage error with a standard deviation of $\sigma = 10$ mV. The DW-deep case is selected that utilizes 90% of the battery capacity from the fully charged state.

From the MC simulation, the estimation errors of each electrode parameters are calculated based on the nominal parameters in Table 4.1. Then, these errors are drawn on scatter plots along with a histogram in Fig. 4.7 verifying the distribution of the estimated electrode parameters is approximately a Gaussian, which agrees with the aforementioned approximation theory. Observe that the estimation errors are centered at near zero indicating the estimates are unbiased. Since the estimator is unbiased, the error bound obtained from the CRB can be considered as a proper metric for our electrode parameter estimation problem. The error bounds of all four electrode parameters at the 95% confidence level show a good agreement with the numerical MC simulation results for both the unconstrained and constrained cases (see Table 4.2 and Table 4.3). Hence, this agreement verifies the derivation of the analytic error bound. In addition to that, for the unconstrained case, a strong correlation has been observed among the parameters from the same electrode, either from the PE or NE, as shown in the top left ($e_{y_{100}}$ vs. e_{C_p}) and bottom right ($e_{x_{100}}$ vs. e_{C_n}) plots in Fig. 4.7. Whereas, the parameters from the different electrodes do not show any correlation. Comparing Table 4.2 and Table 4.3, the parameter dependency in Eq. (4.16) improves the estimation accuracy, especially for the PE parameters.

Table 4.2: Estimation error bound for unconstrained case

w/o constraint	Error bound e_{θ_k} (%)			
	$\theta_1 = y_{100}$	$\theta_2 = C_p$	$\theta_3 = x_{100}$	$\theta_4 = C_n$
MC simulation	2.5	1.3	3.0	3.9
Analytic derivation	2.5	1.3	3.0	3.9

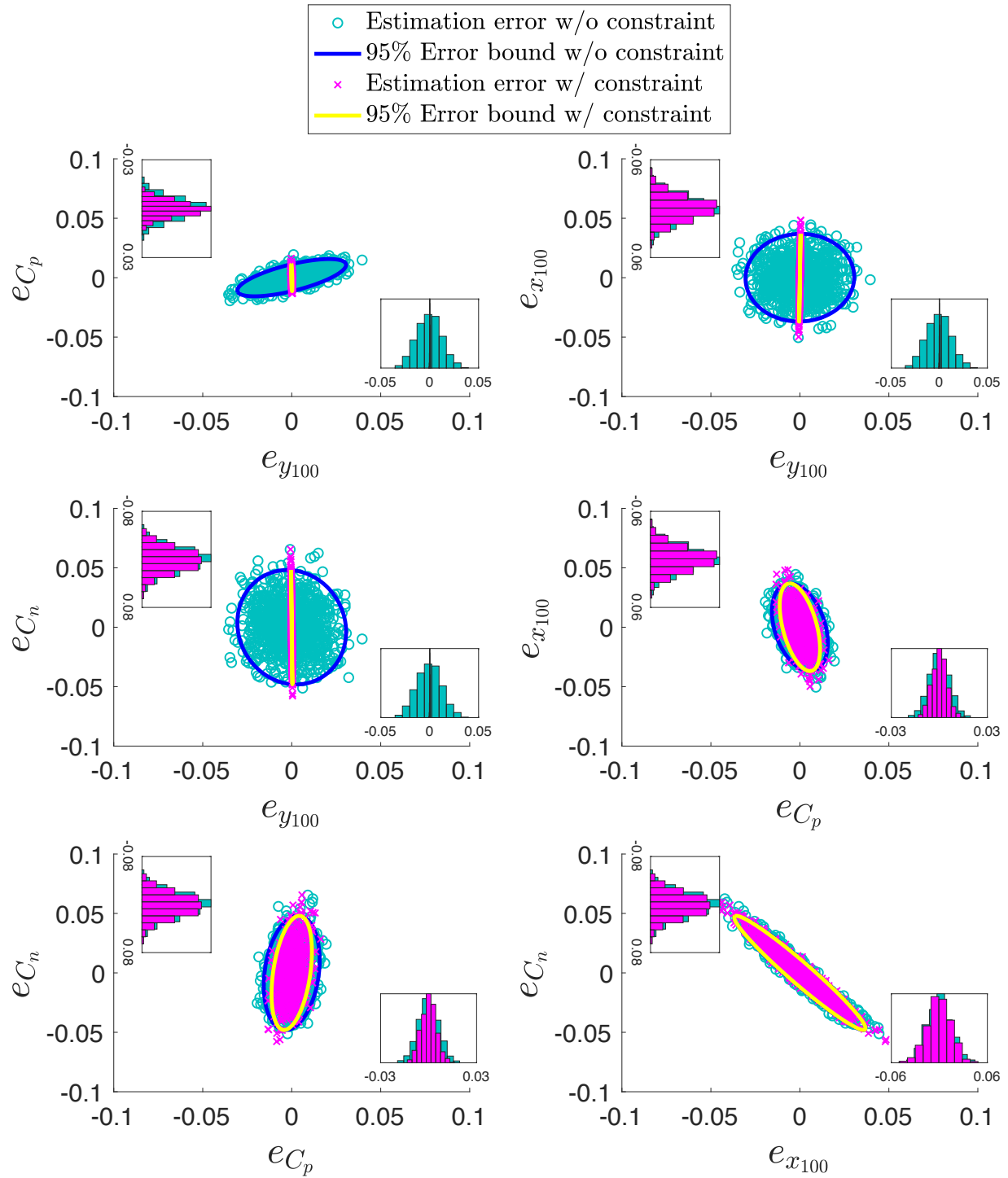


Figure 4.7: Scatter plot of the electrode parameter estimation errors from Monte Carlo simulation for the DW-deep case. Estimation errors show approximate normal distribution. The 95% confidence-level error bound (solid line) agrees with the simulation results.

Table 4.3: Estimation error bound for constrained case

w/ constraint	Error bound e_{θ_k} (%)			
	$\theta_1 = y_{100}$	$\theta_2 = C_p$	$\theta_3 = x_{100}$	$\theta_4 = C_n$
MC simulation	3.2e-2	0.9	3.0	3.9
Analytic derivation	3.0e-2	0.9	3.0	3.9

4.4.2 Experimental validation

In this section, the parameter estimation is done for a 5 Ah NMC/graphite cell at different data availabilities to experimentally validate the proposed analytic error bounds. Pseudo-OCV data is measured at $C/20$ rate of constant current from fully charged state and the half-cell potentials of each electrode are also individually measured from a coin cell referenced by the lithium metal counter electrode. Then, the electrode parameter values are estimated by fitting the OCV model to the voltage data using a nonlinear least-squares estimation as illustrated in Eq. (4.8) including the voltage equality constraint.

To validate the proposed results, the estimates from full-range data are set as a baseline and compared with the estimated parameter values from the predefined data windows to quantify estimation errors. In Fig. 4.8(a), the measured data and the model estimate show a good fit. The voltage errors are spread symmetrically centered at zero such that the assumption on the zero-mean observation error holds. Fig. 4.8(b) shows decoupled voltage curves for both electrodes with an indication for the utilized range (solid lines) along with the full electrode capacity range (dashed lines). Here, the graphite NE has more total electrode capacity; thus the electrode capacity range (red dashed line) is larger than that of the NMC PE (blue dashed line). More detailed information on the parameter estimation can be found in [53, 51, 37].

Fig. 4.9 and Table 4.4 summarize the relative estimation errors obtained from the predefined data windows. Fig. 4.9 shows that most of the errors are inside the error bounds except $e_{y_{100}}$ for the DW-shallow case. Note that the error bounds do not necessarily predict exact error values for a given data window, but describe a boundary for error statistics. From Fig. 4.9 and Table 4.4, not only the inclusion of the estimation errors is validated, but also the effects of different data windows can be found. The DW-deep shows the smallest estimation errors where almost all data range is available. Like in the analytic error bound results in Fig. 4.5, comparing two data windows, the medium and the non-full, that have the same span but at different location, the medium case shows relatively smaller estimation errors especially for the negative electrode parameters (x_{100} and C_n) because the utilization range of the electrode becomes more informative as the DW gets closer to a deeper discharged area.

4.5 Conclusion

In this chapter, the estimation uncertainty of the electrode parameters was quantified with a focus on the limited availability of the OCV data. In realistic scenarios, OCV data is difficult to measure due to the time limit; hence, OCV data is likely limited to an incomplete data window. When such data is limited, the reliability of the estimation accuracy needs to be analyzed.

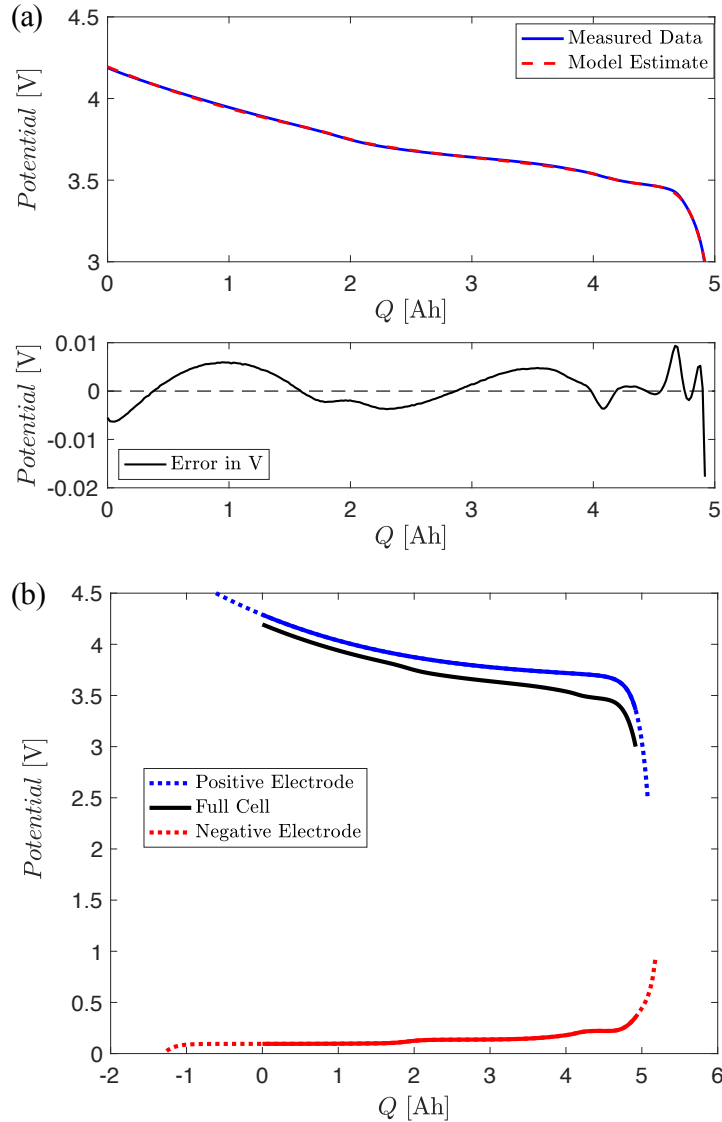


Figure 4.8: The OCV model fit for the given full-range data of a NMC/graphite cell. (a) Measured data and model fit with an error plot, (b) decoupled voltage curves for each electrode; utilized range is marked with solid line and full electrode range is represented by dashed line.

To this end, an analytical error bound of the electrode parameters was derived based on the Cramer-Rao bound and confidence interval. The derived error bounds agreed with the numerical Monte Carlo simulation as well as the experimental results obtained from 5 Ah NMC/graphite cell. The results showed that the data window plays a vital role in the estimation accuracy associated with the local slope of the half-cell potential. Furthermore, the PE parameters can be even more accurately estimated by introducing a voltage constraint in the estimation problem. On the other hand, when only a small portion of data is available, the graphite NE parameters' estimation accuracy is reduced, resulting in a large error bound. Therefore, one must consider estimation

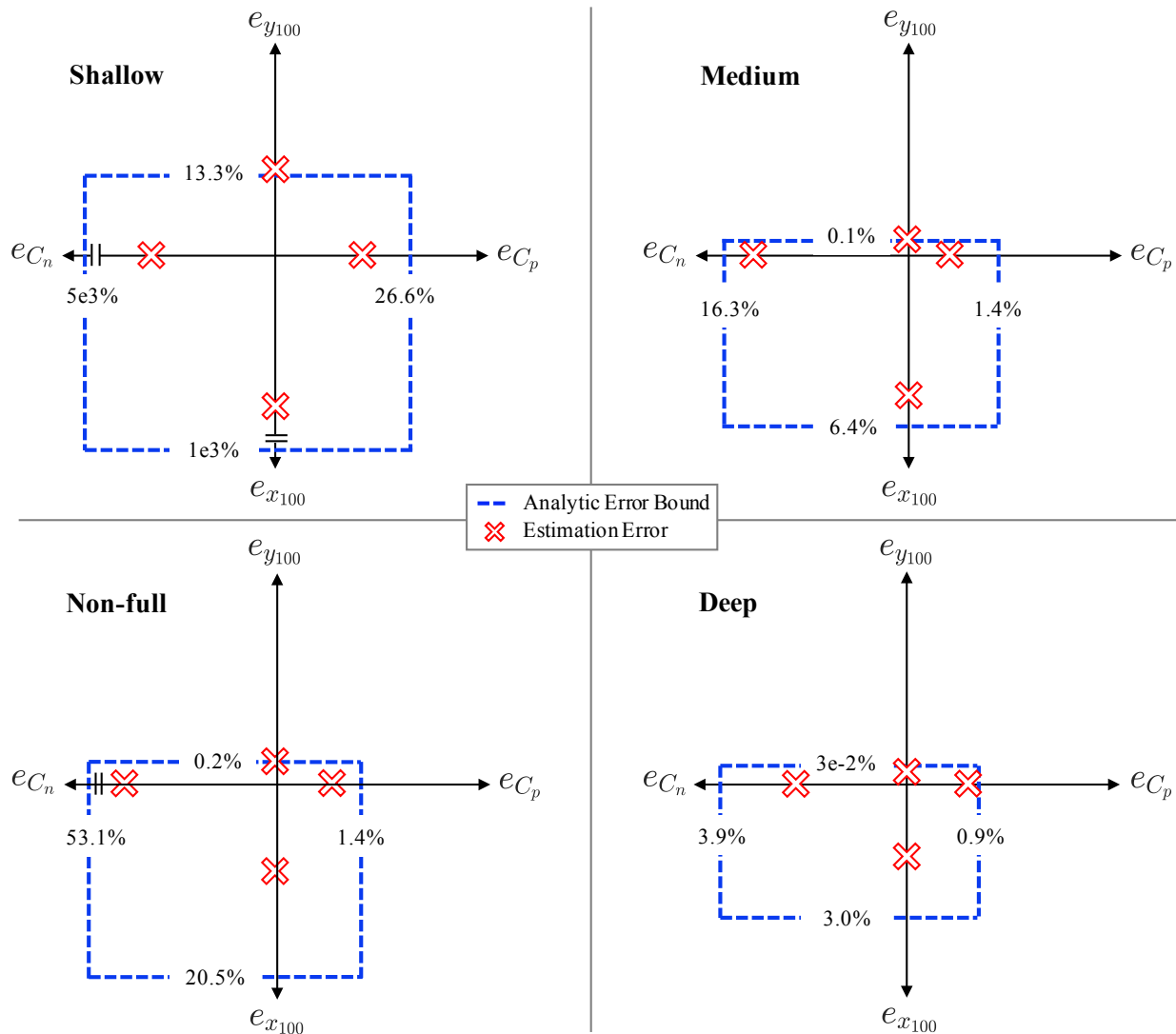


Figure 4.9: Experimental estimation errors for the electrode parameters under different data windows. Most of the estimation errors are inside the analytic error bounds validating the proposed results (graph is not to scale).

uncertainty when the data window is limited.

Table 4.4: Estimation errors for the experimental validation under different data windows.

Data Window ID	Data Window Range	Experimental Estimation Error e_θ (%)			
		$\theta_1 = y_{100}$	$\theta_2 = C_p$	$\theta_3 = x_{100}$	$\theta_4 = C_n$
Shallow	[0.0, 0.2]	14.9	16.8	38.3	24.1
Medium	[0.3, 0.7]	0.1	0.4	4.9	14.5
Non-full	[0.1, 0.5]	0.2	0.9	10.0	24.1
Deep	[0.0, 0.9]	0.0	0.8	1.6	1.8

CHAPTER 5

Minimum-Time Measurement of Open Circuit Voltage of Battery Systems

5.1 Motivation and Connection to Electrode Degradation Diagnostics

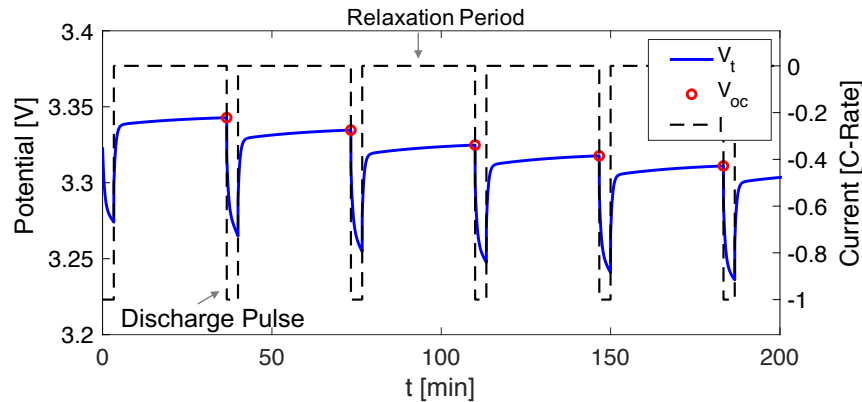


Figure 5.1: Example of incremental open-circuit voltage (OCV) measurement.

The traditional way of measuring open-circuit voltage (OCV) of batteries uses pulse and relaxation, which is time-consuming due to its intrinsic dynamics and corresponding long relaxation period. Typically, rest voltage (i.e., after long hours of relaxation with no current applied) is considered as the OCV at given SOC. For a laboratory test without restriction on testing time, accurate and exhaustive characterization of the OCV-SOC curve can be achieved by applying a series of pulse currents followed by a long relaxation repeatedly, as illustrated in Fig. 5.1. This pulsing procedure is called incremental OCV measurement or Galvanostatic Intermittent Titration Technique (GITT). As one can see in Fig. 5.1, the total amount of time performing the measurement mainly consists of relaxation time, which is simply an elapsed time for terminal voltage goes to a

steady-state. During the relaxation, the terminal voltage varies even though the current is cut-off. Hence, predetermined relaxation time affects the measured voltage value. In literature [55, 5, 87], it has been shown that rest voltage measured with less relaxation time induces error in OCV measurement. Moreover, in many cases, the relaxation time is empirically determined by exploring extensive test cases [78]. For this reason, measurement of exact OCV after long relaxation is time-consuming and not possible to be used in real-world applications.

Instead, it has been shown that very slow rate constant current measurements (e.g., $C/20$: a current rate of 20 hours from a fully charged to a fully discharged state) are close enough to the incremental OCV data. Thus, voltage data obtained from slow rate constant current is generally used as a pseudo-OCV measurement in many studies [8, 11, 37]. However, the $C/20$ rate still requires roughly 20 hours to scan the full range of OCV curve, which is not practical when the given time is limited. Therefore, if only small-time is allowed for data acquisition, we need a strategy in order to maximize opportunity.

We can come up with a two-stage charging strategy for a partial pseudo-OCV measurement, as illustrated in Fig. 5.2. A slow-rate constant current can be applied at Stage II in order to obtain partial pseudo-OCV measurements so that the measured data can be used for electrode-level degradation diagnostics [52, 65]. However, the key to success for Stage II measurement depends on the initial condition at the end of Stage I. Stage I is commonly adopted in electric vehicles (EV) to meet the high demand for fast charging capability. However, due to high current at Stage I, Stage II can not be directly followed unless the battery is at equilibrium state at the end of Stage I. Therefore, we need a method that enables fast charging while satisfying steady-state voltage at the end of Stage I as shown in Fig. 5.2.

In this chapter, a minimum-time optimal control problem is proposed to find an input current profile for direct measurement of pseudo-OCV of lithium-ion batteries such that the relaxation is not required to reach a steady-state voltage. The problem is studied both numerically and analytically with variable-order Gaussian quadrature collocation method and Pontryagin's minimum principle (PMP). The PMP analysis is adopted to show the solution of the problem is either bang-bang or bang-off-bang control by allowing a bi-directional charging, depending on the additional state constraint. The proposed minimum-time input current profile reduces the total testing time by 69% compared to the conventional pulse-relaxation method by removing the relaxation step. The problem is taken one step further by converting it into a finite-dimensional switching-time optimization problem. With the reformulation, the proposed minimum-time optimal control problem shows that it is even computationally tractable for real-time applications. Finally, the proposed method is experimentally validated with a 4.5 Ah NMC/graphite cell showing 69% of time reduction.

The organization of this section is as follows: In Section 5.2, the formulation of the minimum-

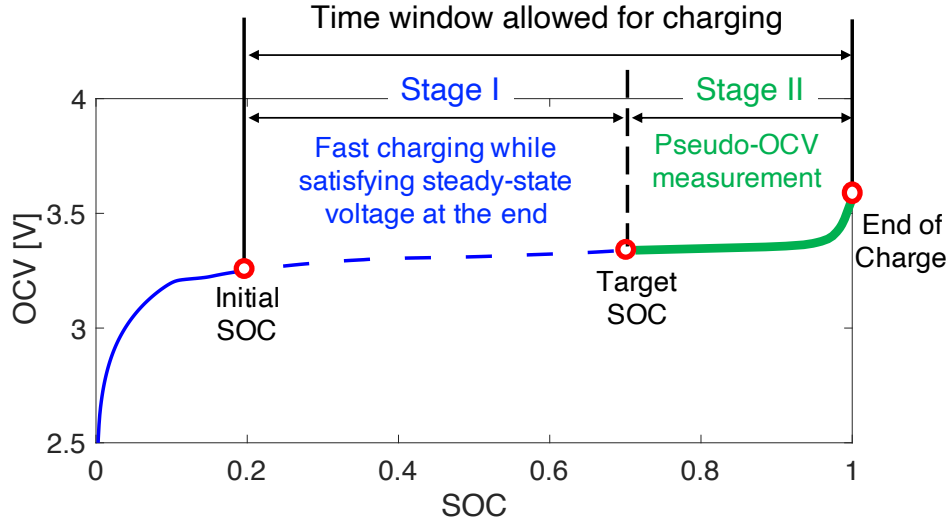


Figure 5.2: Schematic of two-stage OCV measurement strategy. Stage I is the main contribution of this chapter.

time optimal control problem is provided. In Section 5.3, the Pontryagin analysis is applied to explain the sequence of the optimal control solution (i.e., bang-bang and bang-off-bang controls). Section 5.4 introduces the reformulation of a switching-time optimization problem based on the PMP analysis. In the switching-time optimization, we seek the finite number of control discontinuity points with a fixed control sequence in order to obtain fast computation. Section 5.5 presents the simulation results for the proposed minimum-time optimal control trajectory, which is obtained by variable-order adaptive orthogonal collocation methods using the software package GPOPS-II. The results of the reformulated switching time optimization problem are also compared to the solution of the original optimal control problem in terms of computational cost. In Section 5.6, experimental results are presented to validate the proposed method, and Section 5.7 summarizes contributions.

5.2 Minimum-Time Optimal Control Problem

5.2.1 Battery model

For the problem of determining an optimal control input current profile, an equivalent circuit model (ECM) with double RC pairs is considered to capture the battery's voltage dynamics. The ECM is widely used for control-oriented applications owing to its simplicity and reasonable accuracy [42]. The schematic of an equivalent circuit model is shown in Fig. 5.3. Under a current I (positive for charge), the terminal voltage V_t is modeled with three parts,

- The open-circuit voltage, V_{oc} , which is usually a nonlinear function of SOC
- The voltage drop across a series of parallel RC circuits, $V_{1,2}$, which are used to approximate the voltage dynamics during transients
- The voltage drop over a series resistor R_s , accounting for the Ohmic resistance

The voltage dynamics are described as follows:

$$\begin{aligned}
 \frac{dSOC}{dt}(t) &= \frac{1}{3600C_{bat}}I(t), \\
 \frac{dV_1}{dt}(t) &= -\frac{1}{R_1C_1}V_1(t) + \frac{1}{C_1}I(t), \\
 \frac{dV_2}{dt}(t) &= -\frac{1}{R_2C_2}V_2(t) + \frac{1}{C_2}I(t), \\
 V_t(t) &= V_{oc}(SOC) + V_1(t) + V_2(t) + R_sI(t),
 \end{aligned} \tag{5.1}$$

where C_{bat} is the cell capacity. Typically, the equivalent resistance R_i and capacitance C_i vary with SOC, current direction, and temperature; however, they are assumed to be a constant in the following analyses.

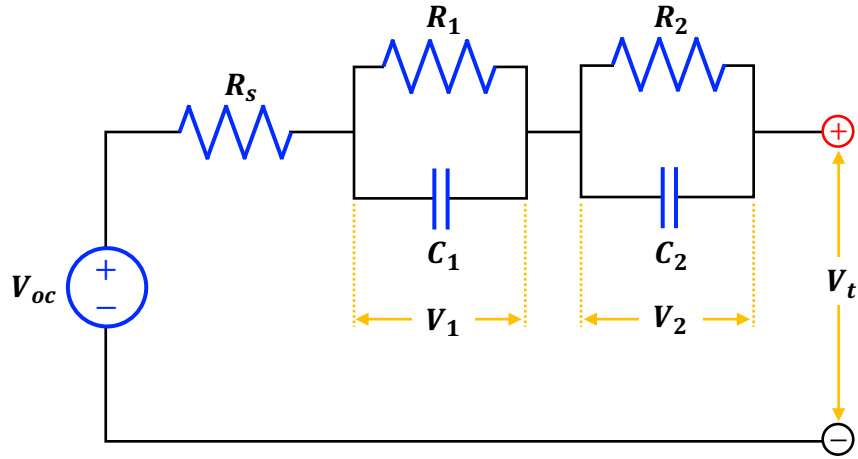


Figure 5.3: Schematic of equivalent circuit model (ECM) with double RC pairs.

By defining the state vector $x = [SOC, V_1, V_2]^T$, input current $u = I$, and output variable $y = V_t$, Eq. (5.1) can be written in a state-space form as given by,

$$\begin{aligned}
 \dot{x} &= Ax + Bu, \\
 y &= h(x, u),
 \end{aligned} \tag{5.2}$$

where the nonlinear function $h(x, u)$ is from the OCV-SOC relationship and voltage elements.

5.2.2 Formulation of minimum-time optimal control problem

This section presents the formulation of an optimal control problem considered in this study. As mentioned earlier, the objective is to change the current SOC to the desired SOC as quickly as possible while satisfying input and state constraints; thus, the considered problem becomes a typical minimum-time optimal control problem. According to Eq. (5.1), when there is no current applied, the steady-state of the terminal voltage, V_t , is determined by the two polarization voltages V_1 and V_2 and hence V_1 and V_2 have to be zero at the final time to reach an equilibrium so that no relaxation period is required. With all these considered, the following optimal control problem can be formulated:

$$\begin{aligned}
\min_{I(t)} \quad & J = \int_0^{t_f} 1 dt = t_f \\
\text{subject to} \quad & \dot{x} = Ax + Bu, \\
& y = h(x, u), \\
& x(t_0) = x_0, x(t_f) = x_f, \\
& G(x, u) \leq 0, \\
& u_{\min} \leq u \leq u_{\max},
\end{aligned} \tag{5.3}$$

where t_f is the final time and $G(x, u)$ denote inequality constraints including state, control, and output variables.

More specifically, the considered constraints are summarized as follows:

$$\begin{aligned}
SOC_{\min} &\leq SOC \leq SOC_{\max}, \\
I_{\min} &\leq I \leq I_{\max}.
\end{aligned}$$

Note that I_{\min} and I_{\max} here can be either discharge and charge current assuming a bi-directional charging is available.

Initial condition x_0 and the target state at the final time x_f are given,

$$\begin{aligned}
SOC(t_0) &= SOC_0, \quad V_1(t_0) = V_2(t_0) = 0, \\
SOC(t_f) &= SOC_f, \quad V_1(t_f) = V_2(t_f) = 0.
\end{aligned}$$

5.3 Pontryagin Analysis for Optimal Control Sequence

Pontryagin's minimum principle (PMP) is a powerful computational and analytical tool to solve an optimal control problem, especially with the constrained control inputs. The PMP analysis provides a set of necessary conditions that the optimal control must satisfy while minimizing the Hamiltonian function.

In general, the optimal control solution cannot be uniquely obtained only with necessary conditions. However, it is still useful and effective in reducing the number of possible control actions to a finite-dimensional subset, and thus, enabling the fast computation of an optimal trajectory. In this paper, the PMP analysis is adopted to understand the structure of solutions to the considered minimum-time optimal control problem.

5.3.1 Minimum-Time control without active state constraints

Consider a minimum time control problem in Eq. (5.3) with system dynamics given in Eq. (5.1). Then, the Hamiltonian \mathcal{H} is defined as,

$$\begin{aligned}\mathcal{H} &= 1 + \lambda^T[Ax + Bu] \\ &= \left(\frac{\lambda_1}{3600C_{bat}} + \frac{\lambda_2}{C_1} + \frac{\lambda_3}{C_2} \right) u + 1 - \frac{\lambda_2}{R_1C_1}x_2 - \frac{\lambda_3}{R_2C_2}x_3,\end{aligned}\tag{5.4}$$

where λ is a co-state vector.

The corresponding co-state equations are written as

$$\begin{aligned}\dot{\lambda}_1 &= -\mathcal{H}_{x_1} = 0, \\ \dot{\lambda}_2 &= -\mathcal{H}_{x_2} = \lambda_2 \frac{1}{R_1C_1}, \\ \dot{\lambda}_3 &= -\mathcal{H}_{x_3} = \lambda_3 \frac{1}{R_2C_2}.\end{aligned}\tag{5.5}$$

In Eq. (5.4), the control inputs u appears as linear; that is, the optimal control input u^* can be determined based on the values of the switching function $\phi = \lambda^T B$, as follows:

$$u^* = \begin{cases} u_{\max} & \phi \leq 0, \\ u_{\min} & \phi > 0, \end{cases}\tag{5.6}$$

with

$$\phi = \lambda^T B = -\lambda_1/3600C_{bat} + \lambda_2/C_1 + \lambda_3/C_2.$$

Eq. (5.6) states that the optimal control u^* minimizing the Hamiltonian \mathcal{H} takes either the upper or lower bound values for control depending on the sign of the switching function ϕ . If the optimal control switches from one extreme to the other within bound (i.e., never in between the bounds), it is referred to as a *bang-bang control*.

The schematic of the bang-bang control trajectory is illustrated in Fig. 5.4 for the battery charging case (i.e. target SOC $>$ initial SOC). As one can see, the obtained optimal input current profile is a concatenation of charge and discharge pulse currents. As a result, the corresponding SOC trajectory Fig. 5.4(b) is non-monotonic piecewise linear, where the value of SOC can go higher than the target SOC along the trajectory.

The resulting optimal current profile and non-monotonic SOC trajectory confirm that the bi-directional charge/discharge capability is required. This means that when the discharge current pulse is applied, the stored energy has to be drawn away from the battery. For instance, when the battery is at charging operation under the proposed two-step charging strategy, the discharged energy can be moved to another energy storage device and charged back to the battery following the bang-bang current profile shown in Fig. 5.4 in order to minimize the energy consumption.

5.3.2 Minimum-time control with active state constraints

The above analysis is based on the assumption that none of the state inequality constraints are active. However, the state constraint for the battery SOC can be active in the considered problem, i.e., $SOC_{\min} \leq SOC \leq SOC_{\max}$. When the state constraints are active for a finite time $t_1 \leq t \leq t_2$, optimal state x^* has to slide along the boundary of the state constraint set $\Omega_x(t)$ and the minimization of the Hamiltonian with respect to control u does not provide useful information. Therefore, the solution in that time interval needs to be found from other considerations. In this study, we adopt the method introduced in [32] for the analysis under the presence of additional state constraint. Further details can be found in Appendix A.1.

Since only one of the bounds can be active at a time, we can define $G(x, t) = x_1 - SOC_k$ where SOC_k is a constant value of either SOC_{\min} or SOC_{\max} . For instance, for the charging case $G(x, t) = x_1 - SOC_{\max}$. According to Appendix A.1, the derivative of the constraint function $G(x, t)$ with respect to time is computed until the control u appears explicitly for the first time in $G^{(j)}$ as follows:

$$\begin{aligned} G^{(0)} &= G(x, t) = x_1 - SOC_k, \\ G^{(1)} &= \frac{d}{dt}G(x, t) = \dot{x}_1 = \frac{1}{3600C_{bat}}u. \end{aligned} \tag{5.7}$$

The control input u appears in the first derivative of the state constraint function $G(x)$; thus, $j = 1$. When the state constraint is active within a time interval $t_1 \leq t \leq t_2$, the following

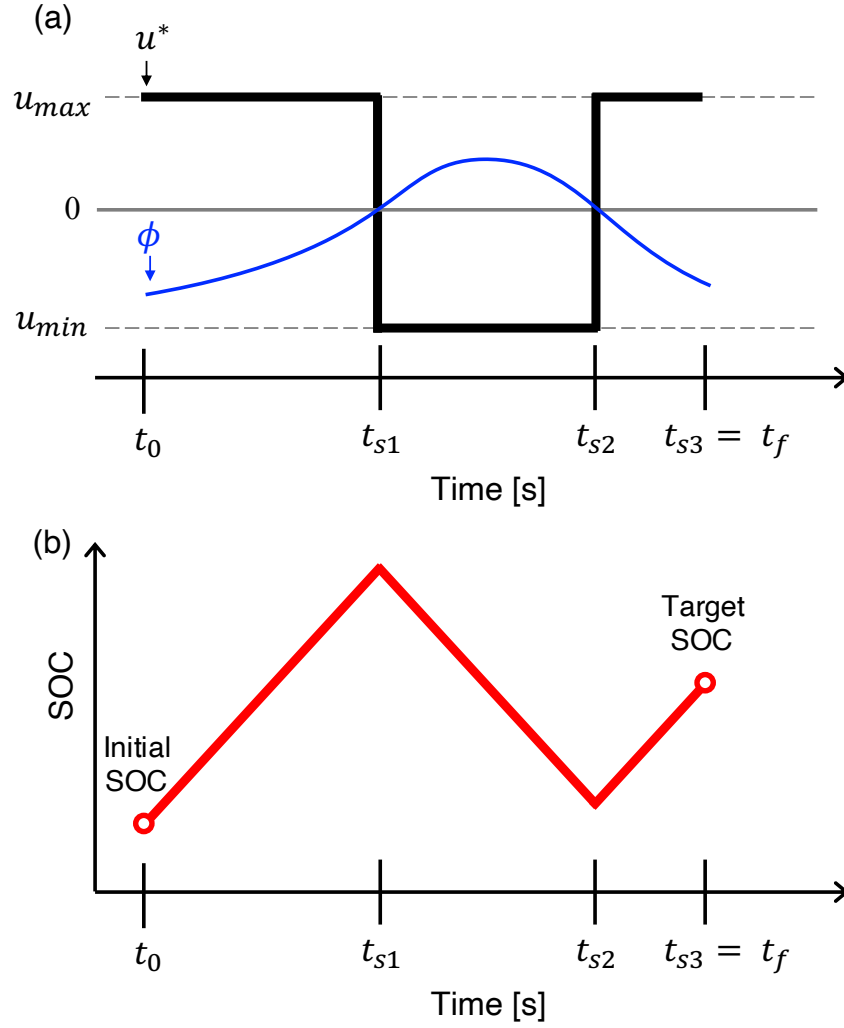


Figure 5.4: Schematic of bang-bang control trajectory. (a) the optimal control u^* takes only upper or lower bound values depending on the sign of the switching function ϕ , (b) SOC trajectory according to the optimal control.

modifications needs to be satisfied:

$$\begin{aligned}
 \bar{H} &= H(x^*, u, \lambda^*, t) + \mu^* G^{(j)}, \\
 \dot{\lambda}^*(t) &= -\bar{H}_x \\
 &= -H_x - \mu^* G_x^{(j)}, \\
 G^{(j)}(x^*, t) &= 0.
 \end{aligned} \tag{5.8}$$

From Eq. (5.8), $G^{(1)} = 0$ is obtained, leading to a solution for control $u = 0$ for the given time interval. Therefore, when SOC hits the bound, the control input current has to be zero, which is a

relaxation step in battery testing terminologies. Given the analysis above, we can conclude that the time-optimal trajectory is a concatenation of bang and off or so-called *bang-off-bang control* with a finite number of switching.

5.3.3 Optimal input current sequence

According to the PMP analysis, it is found that the values of the optimal input current u^* can take are $u^* \in [u_{\min}, 0, u_{\max}]$. However, the possible control sequence also has to be considered. A piecewise continuous function $u^*(t)$ on an interval $[t_0, t_f]$ can only have a finite number of discontinuities. First, when no state constraints considered, the number of switching points can be analyzed by referring a problem of the number of zeros of an exponential polynomial. Moreover, if all eigenvalues of the matrix A from state equation are real-valued, i.e., $A \in \mathbb{R}^n$, then the number of switching points of the optimal control is at most $n - 1$ [105] (See Appendix A.2 for more information).

In this problem, the dimension of matrix A in Eq. (5.2) is $n = 3$ and hence it is expected at most $n - 1 = 2$ switching points along the optimal control trajectory as illustrated in Fig. 5.4. Thus, when the battery SOC state constraint is inactive, two possible control sequences can be considered:

- Charge-Discharge-Charge (CDC): low SOC level to high SOC level
- Discharge-Charge-Discharge (DCD): high SOC level to low SOC level

where the value of input current is chosen from the control upper and lower bounds.

Now, when the SOC-related state constraint is being active during a time interval $t_1 \leq t \leq t_2$, the optimal control is off, i.e., $u^* = 0$, and SOC does not change. However, the other states V_1, V_2 still vary during the time interval until the next optimal control sequence is involved. In this case, it has to be analyzed where the *off* control step can be placed in the entire control sequence. For the case of charging (i.e., the baseline control sequence is CDC), three different control sequences can be considered depending on the location of the *off* control when the battery SOC state constraint is active:

- Charge-Off-Discharge-Charge (Bang-Off-Bang-Bang)
- Charge-Discharge-Off-Charge (Bang-Bang-Off-Bang)
- Charge-Discharge-Charge-Off (Bang-Bang-Bang-Off)

Since only one of the bounds can be active at a time, SOC_{max} is considered for the charging case. Then, the second case can be dropped since the discharge current cannot make the SOC to be bounded by the upper SOC constraint. The third case can also be taken out because *off* at the end of the control sequence, which corresponds to relaxation, is not a finite optimal control solution where the final state is fixed. The third case means waiting for $V_1(t_f) = V_2(t_f) = 0$ by applying zero current, but V_1, V_2 decay exponentially; thus, theoretically, it takes infinite time to converge to 0, which is not a finite solution. Therefore, only possible sequence among three is the first case where the *off* control step is located right after the first charge current is applied as illustrated in Fig. 5.5.

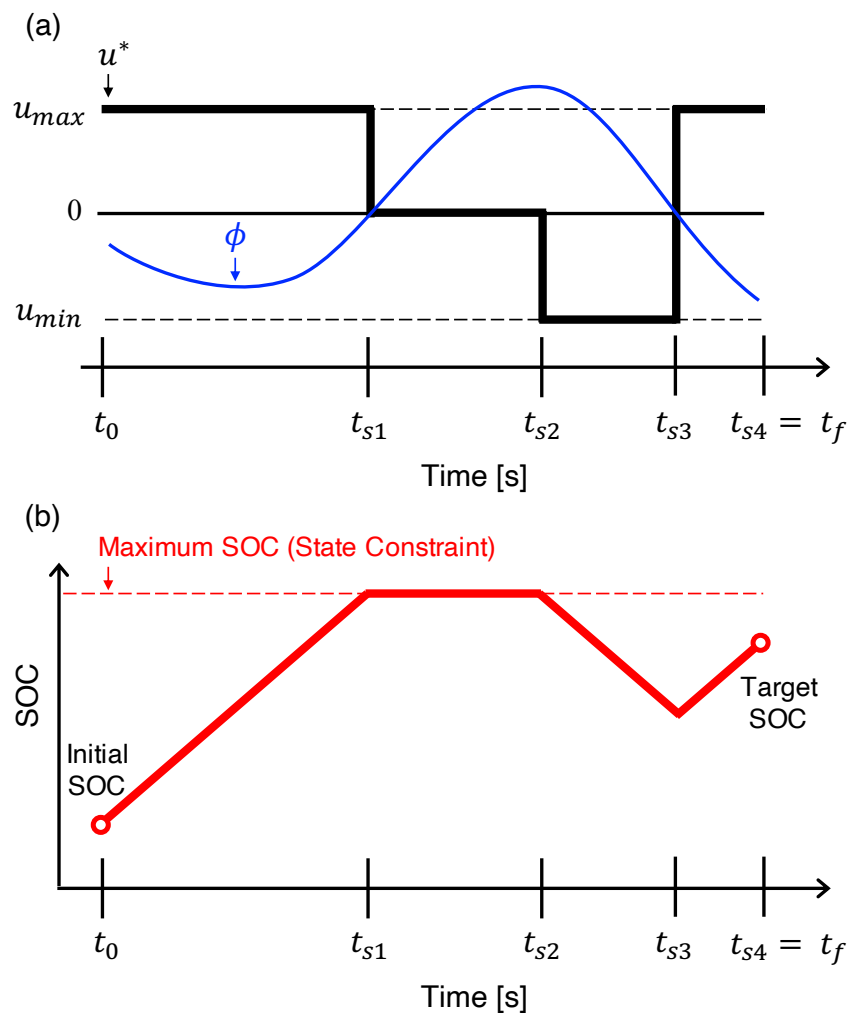


Figure 5.5: Schematic of bang-off-bang control trajectory. (a) the optimal control u^* takes upper or lower bound values and when the state constraint being active the optimal control $u^* = 0$, (b) SOC trajectory according to the optimal control with the maximum SOC active state constraint.

5.4 Conversion to Switching Time Optimization

Based on the PMP analysis that the solution of the optimal control problem is either a bang-bang control or bang-off-bang control, the original control problem can be converted into a finite-dimensional optimization problem of finding proper switching timings of the control sequence [107]. Converting to a switching time optimization problem reduces computational cost considerably, and thus, the proposed method can be implemented in real-time applications.

5.4.1 Switching time optimization for inactive state constraint

Given the control sequence and its value, the optimal control problem can be reformulated into a finite-dimensional optimization problem. Note that the possible control sequence can be either CDC or DCD. In this study, we seek a control input that changes the initial SOC to a higher target SOC without any constraints violation. Thus, the CDC (Charge-Discharge-Charge) is chosen as the optimal control sequence. By keeping the convention of positive current for charge, Eq. (5.3) can be re-written into an optimization problem with new variables $t_k \in [t_{s1}, t_{s2}, t_f]$ (refer to Fig. 5.4) as follows.

$$\begin{aligned}
 & \min_{t_k} J = t_f \\
 & \text{subject to } \dot{x} = Ax + Bu^*, \\
 & \quad x(t_0) = x_0, \\
 & \quad x(t_f) = x_f, \\
 & \quad u^* = \begin{cases} |u_{max}| & t_0 < t \leq t_{s1} \\ -|u_{max}| & t_{s1} < t \leq t_{s2} \\ |u_{max}| & t_{s2} < t \leq t_f \end{cases}
 \end{aligned} \tag{5.9}$$

where the target states at the final time $x_f = [SOC_f, 0, 0]^T$.

5.4.2 Switching time optimization for active state constraint

Switching time optimization problem is generalized for a bang-off-bang control. When it comes to a bang-off-bang control, a relaxation period is included in the control sequence due to the active state constraint. Based on the result in Section 5.5, we can determine the generalized control sequence with the optimization variable $t_k \in [t_{s1}, t_{s2}, t_{s3}, t_f]$ (refer to Fig. 5.5) as follows.

$$\begin{aligned}
& \min_{t_k} J = t_f \\
& \text{subject to } \dot{x} = Ax + Bu^*, \\
& \quad x(t_0) = x_0, \\
& \quad x(t_f) = x_f, \\
& \quad SOC_{\min} \leq x_1(t) \leq SOC_{\max}, \\
& \quad u^* = \begin{cases} |u_{max}| & t_0 < t \leq t_{s1} \\ 0 & t_{s1} < t \leq t_{s2} \\ -|u_{max}| & t_{s2} < t \leq t_{s3} \\ |u_{max}| & t_{s3} < t \leq t_f \end{cases}
\end{aligned} \tag{5.10}$$

where the target states at the final time $x_f = [SOC_f, 0, 0]^T$.

5.5 Simulation Results

This section presents the effectiveness of the proposed current profile in reducing the total testing time through simulation studies. First, the solution to the original optimal control problem is obtained and its results are compared to those from traditional pulse-relaxation. Then, the impact of the active battery SOC constraint and parameter uncertainty on the performance is also investigated. Finally, the solutions to the reformulated switching-time optimization problem are compared to those from the original control problem. Note that, for computing a numerical solution, this study uses a general-purpose MATLAB software package GPOPS-II [74], which is featured by the Legendre-Gauss-Radau (LGR) pseudo-spectral method with adaptive multi-mesh-interval collocation. More detailed theoretical information on this method can be found in [31, 22].

5.5.1 Comparison between ordinary pulse-relation profile and minimum-time current profile

To simplify the analysis, parameters in the equivalent circuit model are assumed constant instead of a function of temperature and SOC. Especially, temperature change was less than 2° in experiment; therefore, the temperature effect is neglected hereinafter.

In simulation study, nominal battery parameters used are as follows:

$$\begin{aligned}
 C_{bat} &= 2.3 \text{ Ah}, \quad R_s = 10.5 \text{ m}\Omega \\
 R_1 &= 17.3 \text{ m}\Omega, \quad C_1 = 1.9e3 \text{ F} \\
 R_2 &= 22.2 \text{ m}\Omega, \quad C_2 = 6.5e4 \text{ F}
 \end{aligned}$$

The constraint boundaries and the initial and final conditions are specified as follows:

$$\begin{aligned}
 SOC_{\min} &= 0, \quad SOC_{\max} = 1 \\
 I_{\min} &= -1C, \quad I_{\max} = 1C \\
 V_{t,\min} &= 2.5V, \quad V_{t,\max} = 3.6V \\
 SOC(t_0) &= 0.2, \quad SOC(t_f) = 0.48, \\
 V_1(t_0) &= V_2(t_0) = 0, \quad V_1(t_f) = V_2(t_f) = 0.
 \end{aligned}$$

Here, the input current is limited for a bound of 1C rate (a C-rate is a measure of the rate at which a battery is discharged relative to its maximum capacity) that can charge and discharge the battery. Target SOC is chosen, such that the battery is charged for 1,000 seconds at a 1C rate. To validate the time reduction, two cases are compared; the first case is the ordinary pulse-relaxation profile where the constant charging current pulse is applied, followed by a relaxation period. The second case is where the minimum-time current profile is applied.

5.5.1.1 Ordinary Pulse-Relaxation Profile

We can monitor voltage dynamics across the two RC pairs (V_1, V_2), accounting for the relaxation time, as shown in Fig. 5.6. Here, the battery model is simulated at a 1C rate charging current for 1,000 seconds. The terminal voltage is dropped instantaneously when the current is cut-off, and then, the voltage relaxation period follows. Since the 2nd RC pair has a larger time constant, its slow voltage response V_2 dominates voltage dynamics and the relaxation time as shown in Fig. 5.6(d)). The total testing time is about 140 minutes for one OCV point, mostly spent on the long-relaxation period.

5.5.1.2 Minimum-Time Current Profile

The minimum-time optimal current profile and corresponding voltage dynamics are summarized in Fig. 5.7. The optimal current profile consists of charge, discharge pulse, and a short duration of charge pulse with no relaxation period (i.e., control sequence is Charge-Discharge-Charge). Initial SOC is changed to the target SOC and the RC pairs' voltage reach zero at the final time, i.e.,

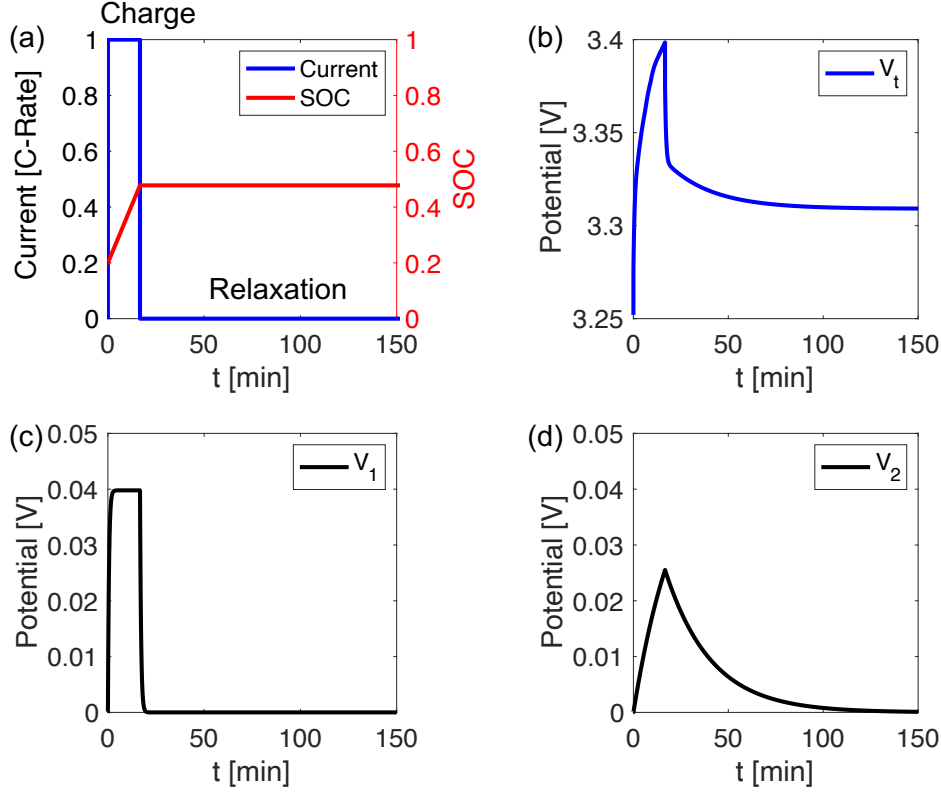


Figure 5.6: Ordinary pulse-relaxation for OCV measurement. (a) current profile (Charge-Relaxation) and SOC variation, (b) terminal voltage, (c) voltage across 1st RC pair, (d) voltage across 2nd RC pair. Total testing time for one OCV point measurement is about 140 min.

$V_1(t_f) = V_2(t_f) = 0$ (see Fig. 5.7(c) and Fig. 5.7(d)). With the minimum-time profile, it takes 43 minutes in total to achieve the goal, which is only 31% of the previous testing time (69% reduction) at the ordinary pulse-relaxation case as summarized in Table 5.1.

In optimal control problems, control is typically set to be between lower and upper bounds, and if the optimal control switches from one extreme to the other without taking a value in between, then it is referred to as a bang-bang control. As shown in Fig. 5.7(a), the current values are either positive or negative 1C, which are the maximum allowable current extremes, indicating the minimum-time current profile is a bang-bang control. Another interesting observation is that the SOC trajectory is now non-monotonic. Along the trajectory, the SOC goes beyond the target value, and the excessive amount of SOC is then balanced by a discharge pulse followed. When the 1st switching occurs, as shown in Fig. 5.7(c) and Fig. 5.7(d), V_1 drastically switches from positive to negative value due to the relatively fast time constant compared to V_2 . Meanwhile, 2nd RC pair's voltage V_2 gradually decreases until it is close to zero. And then, the 2nd switching occurs from the discharge pulse to a short duration of the charge pulse in order to make both voltages equal

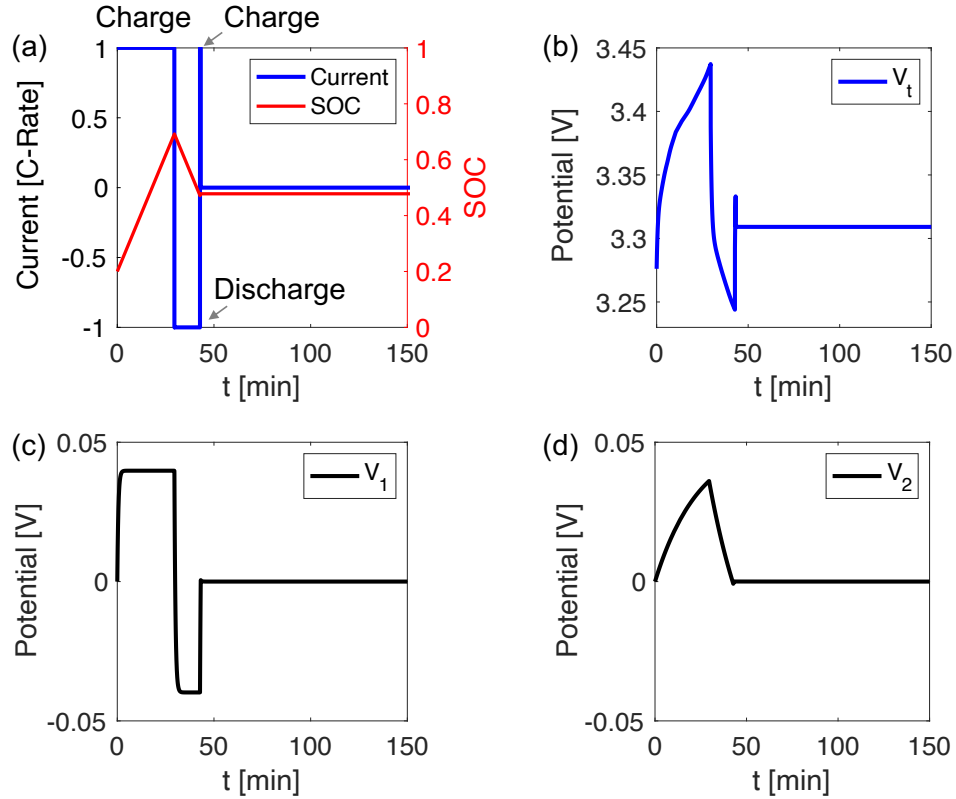


Figure 5.7: Minimum-time current profile for OCV measurement. (a) current profile (Charge-Discharge-Charge) and SOC variation, (b) terminal voltage, (c) voltage across 1st RC pair, (d) voltage across 2nd RC pair. Total testing time for one OCV point measurement is 43 min (69% time reduction).

to zero. Finally, the voltages of both RC pairs V_1, V_2 converge to zero, and the terminal voltage becomes a steady state.

Electrochemically speaking, this decaying pattern of the relaxation voltage is from a slow diffusion process of lithium inside the solid particles. When a constant current flows, Li concentration inside the solid particle has a gradient from the center of the particle to the surface. When the current is cut-off, the gradient of Li concentration tries to find a uniform distribution so-called diffusion phenomenon, which causes changes in the overall Li concentration inside particles. Moreover, since the surface concentration of the lithium determines the open-circuit potential of the electrode particle, the terminal voltage we measure changes slowly along with the re-distribution of the Li concentration.

On the other hand, the proposed minimum-time current profile applies a concatenation of charge and discharge pulses, which essentially perturbs the lithium concentration distribution inside the electrode particles. In other words, the optimal current profile makes the surface Li con-

Table 5.1: Comparison of total testing time without active state constraint

Total Testing Time		Time Reduction
Pulse-Relaxation	Minimum-Time	
140 [min]	43 [min]	-69%

centration closer to the average concentration over a particle, thus no need for a long period of re-distribution step. Needless to say that these pulses do not guarantee a perfect uniform distribution; hence, the relaxation voltage of an actual Li-ion cell might oscillate around the steady-state.

5.5.2 Minimum-time current profile with active state constraint

In this section, an active state constraint and its impact on total testing time are presented. As shown in Fig. 5.7(a), the SOC trajectory is non-monotonic such that it exceeds the target value along its path. In case the given bound constraint for SOC is violated, the original optimal current profile needs to be altered under the presence of an active state constraint. In order to study the impact of the different level of active state constraint, we change the upper bound of SOC constraint SOC_{\max} while keeping the initial and target SOC's the same as follows:

$$\begin{aligned}
 SOC_{\min} &\leq SOC \leq SOC_{\max}, \\
 SOC_{\min} &= 0, \quad SOC_{\max} = 0.60 \\
 SOC(t_0) &= 0.2, \quad SOC(t_f) = 0.48.
 \end{aligned}$$

Table 5.2: Comparison of Total testing time with Active State Constraint

Total Testing Time		Time Reduction
Pulse-Relaxation	Minimum-Time	
140 [min]	46 [min]	-67%

The modified problem is solved, and the results are summarized in Fig. 5.8 and Table 5.2.

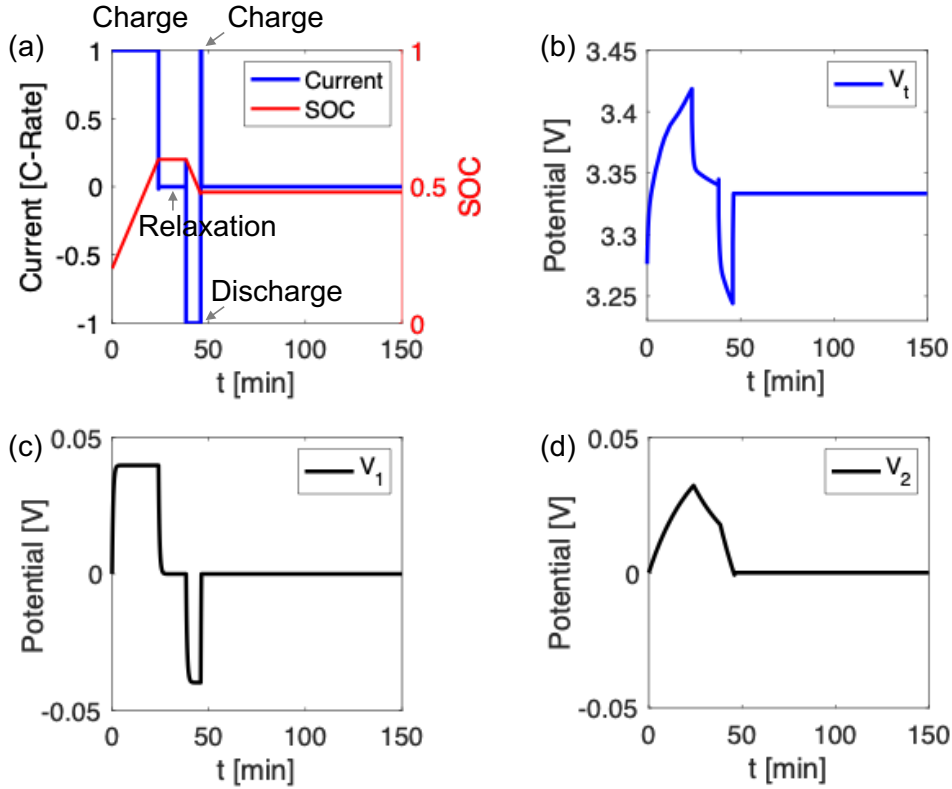


Figure 5.8: Minimum-time current profile for OCV measurement with an active state constraint for $SOC_{\max} = 0.60$. (a) current profile (Charge-Relaxation-Discharge-Charge) and SOC variation, (b) terminal voltage, (c) voltage across 1st RC pair, (d) voltage across 2nd RC pair. Total testing time for one OCV point measurement is 46 min (67% time reduction).

First of all, we observe a relaxation period in Fig. 5.8(a) when the SOC hits the upper bound of $SOC_{\max} = 0.60$ by the first charge current. The modified control sequence is Charge-Relaxation-Discharge-Charge. During the relaxation period, both voltages decrease exponentially due to its dynamics without any current being applied; however, V_2 , which has a relatively slow time constant, still needs to be forced to zero potential with a discharge pulse (see Fig. 5.8(c) and Fig. 5.8(d)).

Another important observation is that there exists a trade-off relationship between the total testing time and the level of SOC upper bound. The difference from the previous case where there is no bound constraint is that a relaxation period is now required for some amount of time because of the SOC constraint; thus, total testing time increases. However, the effectiveness of time reduction is still significant, even with a narrow SOC constraint bound. For instance, as one can see in Fig. 5.9, for the same target SOC ($SOC(t_f) = 0.48$), the total testing time is 76 min (46% time reduction) with an upper bound of $SOC_{\max} = 0.50$. Furthermore, as the bound increases, total testing time decreases. This time reduction is a benefit of allowing opposite current directions

(e.g., charge to discharge for an increasing SOC) in the control sequence. Therefore, if there is a need for a minimum perturbation of the battery (e.g., a small SOC variation), we can introduce a tightly bounded SOC constraint while allowing both charge and discharge input currents for the control sequence.

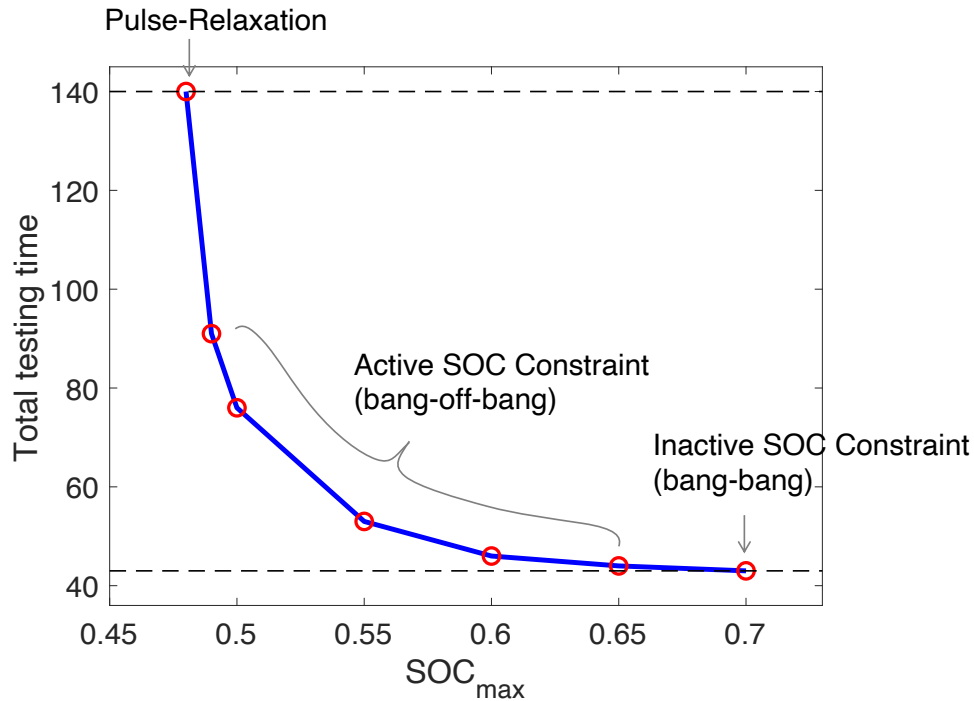


Figure 5.9: Trad-off relationship between total testing time and the level of SOC upper bound. Pulse-relaxation point is when no optimal control sequence is involved. The SOC constraint becomes inactive above $SOC_{\max} = 0.70$ for a target SOC is 0.48.

5.5.3 Sensitivity of model parameter error

One thing to note is that the optimal control problem can be solved when the model parameters are known. However, as mentioned earlier, battery parameters can change over time. Then, we can perform a parameter estimation regularly for model calibration when the battery model prediction deviates from the measured data. For the equivalent circuit type of models, it has been studied extensively on how to estimate the circuit parameters using a variety of offline and online techniques. In offline cases, parameter estimation is mostly done in a batch process based on the least-squares approaches. Two of the best-known techniques are the electrochemical impedance spectroscopy (EIS) [23] or pulsed current tests (PCT). During battery operation, we can use online estimators such as recursive least-squares (RLS) [125] and extended Kalman filter (EKF) [118]. However, these approaches rely on the static output nonlinearity and do not address how to update the OCV

curve.

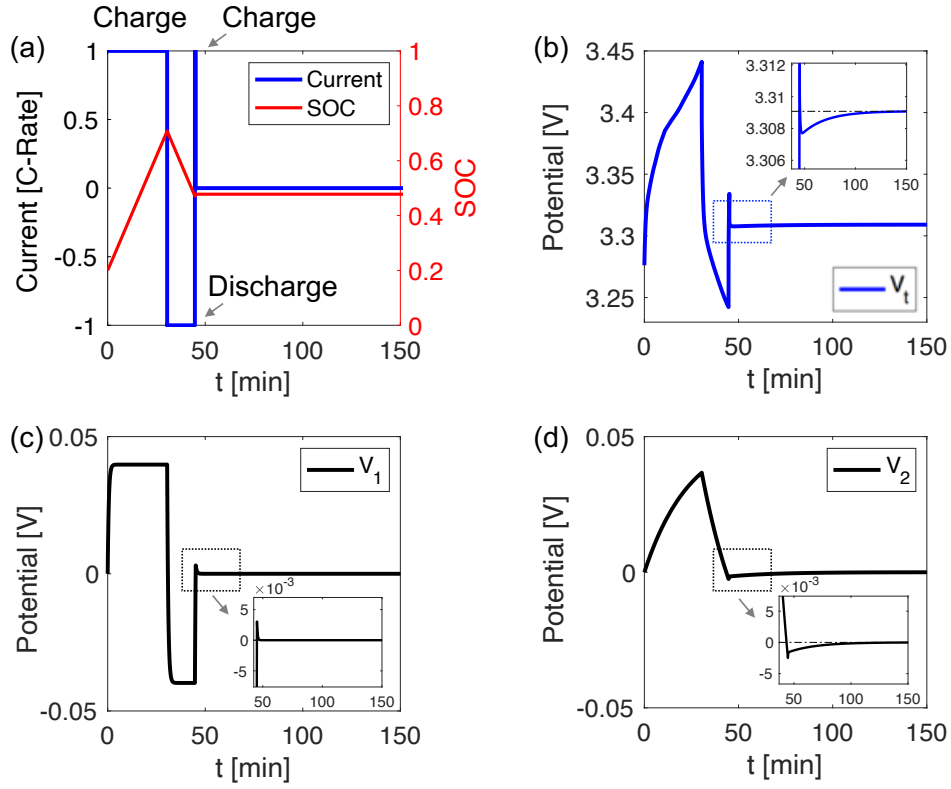


Figure 5.10: Minimum-time current profile for OCV measurement with 10% parameter errors. (a) current profile and SOC variation, (b) terminal voltage, (c) voltage across 1st RC pair, (d) voltage across 2nd RC pair. Total testing time for one OCV point measurement is about 100 min (29% time reduction).

If there is an error in the model parameters either from parameter estimation or due to aging, it should be analyzed how sensitive the proposed method is to the parameter error. In order to see the impact on the total testing time, the diffusion related RC pair parameters are increased by 5% in the plant model, and the minimum-time current profile that is obtained with the nominal parameters is applied. Note that increasing all RC parameters by 5% is the same as the time constant, $\tau = R \times C$, has changed by 10.25% in total. According to Eq. (5.1), the time constant τ determines the relaxation time after the current is cut-off. In other words, if one of the RC parameter is overestimated and the other is underestimated than true value, the total impact on the time constant can be compensated. Thus, the parameter error focused here is the time constant of both RC pairs.

The results are summarized in Fig. 5.10 and Table 5.3. The parameter error causes the terminal voltage deviated from the OCV, and it requires the relaxation time after the current becomes zero. However, the benefit of the minimum-time current profile is still observed. The total testing time

has reduced to 100 minutes (29% time reduction) in spite of the 10% error in the time constant for both RC pairs. Here, the OCV and corresponding measurement time are strictly defined when the terminal voltage reaches a complete steady-state. However, in practice, the amount of time reduction can be more beneficial by allowing steady-state defined within a bound rather than a fixed value.

Table 5.3: Comparison of Total testing time with 10% parameter errors in the model

Total Testing Time		Time Reduction
Pulse-Relaxation	Minimum-Time	
140 [min]	100 [min]	-29%

5.5.4 Reformulated switching time problem

In this section, the solutions from the original minimum-time optimal control problem and the reformulated switching time optimization problem are compared. Ideally, the reformulated switching time problem should provide the same results, but with less computation time.

5.5.4.1 Bang-Bang Control Case

The new optimization variables, t_k , are switching time when the current value switches from one extreme to another. Once the switching time is fixed, the entire input current profile is determined for the system dynamics. The solution of switching time is found based on the objective function, which is minimum final time, and the state constraint at final time. Therefore, the transformed switching time problem is a constraint optimization problem. Here, we use *fmincon* in MATLAB to solve the switching time optimization problem in Eq. (5.9).

One benefit is that the converted switching time optimization problem requires less computation time than the original optimal control problem, as shown in Table 5.4. Numerical simulations were run on a computer equipped with an 2.5GHz Intel quad-core i7-4870HQ processor and 16 GB of RAM running on macOS 10.15.2. Note that the aforementioned minimum-time problem is solved with a tool (i.e., GPOPS-II) specifically designed for an optimal control problem. Thus, if one uses typical approaches for trajectory optimization such as nonlinear programming and dynamic programming (DP) [6], it would take more computational cost.

Table 5.4: Comparison of two different solutions in switching points with the computation time

	Switching Points [min]			Computation Time [sec]
	t_{s1}	t_{s2}	t_f	
Minimum Time (Sec. 5.3.1)	29.7	43.0	43.4	3.5
Switching Time (Sec. 5.4.1)	29.7	43.0	43.4	0.4

5.5.4.2 Bang-Off-Bang Control Case

Under the presence of an active state constraint, the switching time optimization problem is reduced to Eq. (5.10) and the results of switching points are presented in Table 5.5. One can see, the two different approaches provide the same solution. To compare with the results in Section 5.5.2, the target SOC and state constraint were chosen for $SOC_f = 0.48$ and $SOC_{\max} = 0.60$. When it comes to the computation time, the benefit of converting to a switching time optimization becomes more significant. In general, computation time increases as the complexity of the problem increases, such as including the active state constraint. Comparing the two approaches in Table 5.5, the switching time optimization requires much less computing in solving the problems, i.e., it only takes 14% of computation time compared to the original optimal control problem. This is because we found the control sequence and its value from the PMP analysis and the finite number of switching points, which reduces the size of feasible solution space. Specifically speaking, in the minimum-time optimal control problem, the control u can be any value between the upper and lower bounds; thus, the finding an optimal control is not only to search the sequence but also the value while checking the violation of the constraints. On the other hand, in the converted switching time optimization problem, we already have prior knowledge of the control sequence and its value; therefore, the optimization variable is only the switching time.

5.6 Experimental Validation

This section validates the time reduction in measuring an OCV point compared to conventional pulse-relaxation case. The model parameters $\theta = [R_S, R_1, C_1, R_2, C_2]$ are identified using least-squares fit [76] and summarized in Table 5.6. Then, the minimum-time optimal control problem is solved and the optimal input current is applied to a 4.5 Ah Nickel-Manganese-Cobalt (NMC) oxide/graphite pouch cell, which was built at the University of Michigan Battery Lab.

Table 5.5: Comparison of two different solutions in switching points under the presence of an active state constraint

	Switching Points [min]				Computation Time [sec]
	t_{s1}	t_{s2}	t_{s3}	t_f	
Minimum Time (Sec. 5.3.2)	24.0	38.3	45.9	46.2	4.3
Switching Time (Sec. 5.4.2)	24.0	38.3	45.9	46.2	0.6

Table 5.6: Identified parameters for the equivalent circuit model

Identified ECM Parameters	
Parameters	Values
R_s	8.84 [m Ω]
R_1	7.10 [m Ω]
C_1	5.56e3 [F]
R_2	4.17 [m Ω]
C_2	2.26e5 [F]

5.6.1 Comparison between Pulse-Relaxation and Minimum-Time Profile

In this section, the total testing time is compared with two different methods of measuring an OCV point: (i) ordinary pulse-relaxation and (ii) proposed minimum-time profile. At each current profile testing, the cell was initialized to a 50% SOC under the room temperature of 25°C. For both cases, the current limit is set to 1C-rate bound for both charge and discharge to prevent any adverse degradation of the cell. Note that one can allow higher current level for the bound. The target SOC is chosen at 55% SOC. The ordinary pulse-relaxation profile applies 1C constant charge current until the cell SOC reaches the target value. Once it reaches the target SOC, the applied current is cut-off, called a relaxation period, until the relaxation voltage reaches a steady-state. The minimum-time optimal current profile allows the input current to be a charge or discharge current within the given bound.

In Fig. 5.11, one can see the proposed minimum-time profile takes a longer time for initial

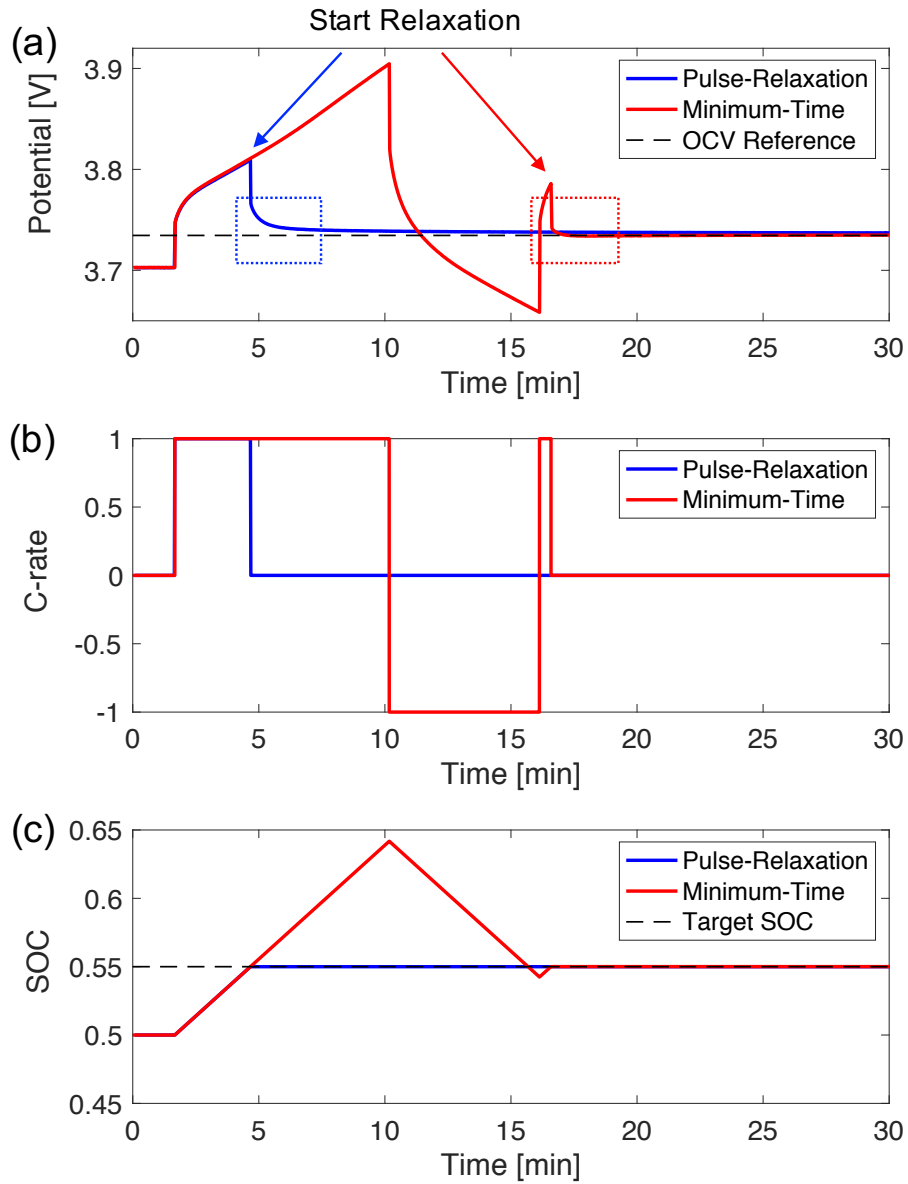


Figure 5.11: Experimental results for pulse-relaxation profile and minimum-time profile. (a) terminal voltage trajectory, (b) current profile in C-rate, (c) SOC trajectory.

SOC variation than that of the ordinary pulse-relaxation method. It is because the minimum-time profile exceeds the target SOC during the first charge current (see Fig. 5.11(c)). However, to measure a steady-state terminal voltage or OCV, it is necessary to consider the relaxation period that dominates the testing time. The relaxation voltage is the voltage response right after the current is cut-off. In Fig. 5.11(a), the voltage of the pulse-relaxation profile drops instantaneously when the

current becomes zero. After this instantaneous voltage drop, the relaxation period follows showing an exponential decaying pattern.

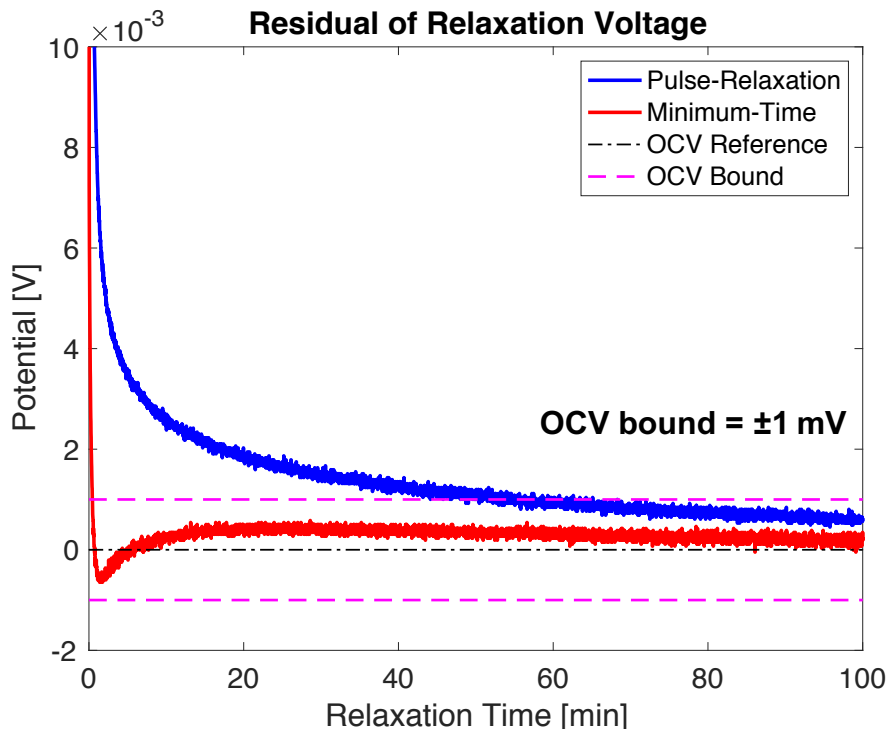


Figure 5.12: Relaxation voltage with respect to the OCV reference. OCV bound of 1 mV is plotted as dashed line to determine the relaxation time.

The zoom-in view of relaxation voltages are shown in Fig. 5.12. In this figure, time is set for zero at the start point of relaxation period (i.e., relaxation time), and the relaxation voltage is subtracted by the reference OCV value to highlight the deviation from the OCV reference. The OCV reference is defined as a steady-state terminal voltage; we take the measurement after 5hr relaxation. As we discussed earlier, the ordinary pulse-relaxation case shows the exponential decaying relaxation voltage. On the other hand, the minimum-time profile case shows a slight oscillation in the relaxation voltage, indicating the surface Li concentration of the electrode particle is still fluctuating after the current is cut-off. Nevertheless, the relaxation voltage of the proposed minimum-time profile is within a very narrow OCV bound (i.e., ± 1 mV). The OCV bound is introduced here for practicality. Even though the OCV reference should be treated as true OCV measurement, in many applications, a tolerance (or bound) is given to define a single measurement value considering measurement error due to noise or sensor accuracy. Therefore, the relaxation time is defined when the residual voltage is within a reasonable OCV bound. Note that one can also determine the OCV in terms of the slope of the voltage change, e.g., $dV_t/dt \approx 0$.

Total testing time for one OCV measurement is summarized in Table 5.7. With the given 1 mV

OCV bound, the ordinary pulse-relaxation takes 55 minutes (= 5 minutes for SOC variation + 50 minutes for relaxation). On the other hand, the proposed minimum-time current profile only takes 17 minutes (= 16 minutes for SOC deviation + 1 minutes for relaxation). Therefore, it is shown that the proposed minimum-time current profile is able to obtain very accurate OCV measurements with much less time. It is noted that the temperature rise due to the pulses from the proposed profile is less than 2°C, and it drops quickly when the current is cut off, which allows us to neglect the adverse effect on the cell degradation due to temperature rise.

Table 5.7: Comparison of total testing time for one OCV measurement from experiment

Total Testing Time		Time Reduction
Pulse-Relaxation	Minimum-Time	
55 [min]	17 [min]	-69%

5.7 Conclusion

In this chapter, an optimal control problem is proposed for direct measurement of open-circuit voltage (OCV) of a cell showing a substantial benefit in reducing the data acquisition time compared to a conventional pulse-relaxation method.

The minimum-time problem was solved numerically and analyzed by Pontryagin's maximum principle (PMP). The PMP analysis is adopted to find the optimal control sequence with the consideration of the state constraint. And then, the minimum-time optimal control problem was converted into a finite-dimensional switching time optimization problem. By converting the problem, it is shown that the proposed method is even computationally tractable for real-time applications. The results were shown with simulation and experiment that the data acquisition time for the cell OCV can be reduced by 69% compared to the conventional pulse-relaxation method.

CHAPTER 6

Electrode-Specific Degradation Diagnostics at Practical Charging Rate

6.1 Introduction

Pseudo-OCV measurement makes the implementation of the electrode-specific degradation diagnostics challenging in that it requires a very low rate constant current applied. This low-rate current requirement limits the time for data acquisition, raising a partial data availability issue in practice. In Chapter IV, the partial data window of the OCV curve and corresponding estimation accuracy was well-addressed.

Ideally we need robust algorithms that enable the estimation of aging mechanisms during normal or even fast charging. To this end, one of the candidates for a diagnostic algorithm is an extension of the peak alignment method [54] from Chapter III. In that method, the distance between two observable peaks in the differential voltage is used to estimate the graphite negative electrode's operating window and capacity using a pseudo-OCV data. These peaks are the result of the phase transitions in the graphite at specific lithiation states that enables the electrode-specific degradation diagnostics.

In this work, the feasibility of electrode degradation diagnostics is studied at a practical charging rate instead of the pseudo-OCV measurement considering a typical charging scenario in real-world applications. Under a dynamic load condition, a Li-ion cell's terminal voltage is apart from an equilibrium state (i.e. open-circuit voltage) due to its overpotential. This deviation from the equilibrium condition makes the electrode state of health (eSOH) estimation challenging. Therefore, it is needed to understand the boundary of the eSOH estimation in terms of the increasing charging rate assuming a constant current charging operation (i.e. typical constant-current-constant-voltage, CCCV, charging protocol).

This section is organized as follows. Section 6.2 opens discussion on the practical charging rate for typical electric vehicles and corresponding two consideration factors. In Section 6.3, the peak behavior map is constructed with respect to aging and C-rate to understand the boundary of

the electrode SOH estimation and the peak smoothing phenomenon is analyzed with electrochemical models. In Section 6.4, the method of estimating the internal resistance is introduced with the sensitivity-based data selection feature to improve the estimation accuracy. Furthermore, we propose the comprehensive electrode-specific SOH estimation algorithm considering a real-world usage scenario for battery electric vehicles. In Section 6.6 summarizes contributions.

6.2 Practical Charging Rate

When it comes to practical charging rates, it depends on three factors: 1) the size of the battery system, 2) the charging power, and 3) the acceptable rate of charge for battery systems. Roughly speaking, the time to full charge from empty (in hours) or C-rate can be estimated by dividing the battery size (in kWh) with the charging power (in kW). The C-rate is a measure of the current rate relative to its capacity at which a battery is completely discharged from a fully charged state. For electric vehicle (EV) applications specifically, the charger type is commonly categorized into three based on their charging capability: Level 1, Level 2, and Level 3 (or often called DC fast charging). A Level 1 charger is simply charging from a standard 120V household outlet without additional installation, which provides about 2 to 5 miles of range per hour (charging power is from 1.4 kW to 2.3 kW). Level 2 is the most common type for EV chargers since they require simple installation yet have a good power output of around 7.7 kW up to 19.2 kW, adding between 15 and 40 miles of range per hour of charging. Level 3 or DC fast chargers have the highest charging power, around 50 kW up to 150 kW, but they are expensive and require a complex installation. In recent years, ultra-high DC off-board charge with 250 kW is in development to keep up with the long-range EVs equipped with a large battery pack and make the charging comparable to refilling gas.

For a typical mid-range battery electric vehicle with a 39 kWh battery pack, it would take 6 hours to fully charge the car from empty using a 7.2 kW - Level 2 charger. It is true that EVs are rarely charged from empty, but we still can get an idea of the approximated range of C-rate of $C/5$ considering Coulombic efficiency. Charging time data in Table 6.1 is compiled from [19], [58], and automaker's charging guideline. Considering the most accessible charger type is the Level 2 charger, the practical charging rate can be defined from $C/13$ up to $C/5$.

In regards to a practical charging rate, two factors need to be considered: 1) peak smoothing behavior, and 2) overpotential due to internal cell resistance. The first part is a C-rate dependency on peak behavior. As Fig. 6.1 shows, the peaks in the differential voltage curve widen and shift as the charging C-rate increases. Since local peaks in the differential voltage curve are closely related to the graphite negative electrode parameters, it can result in poor estimation accuracy for the electrode SOH.

Secondly, the overpotential due to the internal resistance is no longer negligible under practical

Table 6.1: Estimated charge time chart for battery electric vehicles. Charge time can vary depending on ambient temperature and vehicle's acceptance rate.

Battery Electric Vehicle			Charging Time* [hrs]		
Model	Battery Size [kWh]	Range [miles]	Level 1 (1.4 kW)	Level 2 (7.2 kW)	DC Fast (50-150 kW)
Tesla Model S 100D 2019	95	303	71.5	13.0	0.8 (0-80%)
Audi e-tron SUV 2019	95	204	68.0	12.5	0.8 (0-80%)
Jaguar i-Pace 2019	90	234	64.5	13.0	0.8 (0-80%)
Hyundai Kona Electric 2019	64	258	45.5	9.0	0.5 (0-80%)
Chevrolet Bolt EV 2019	60	238	43.0	8.5	1.5 (0-80%)
Nissan Leaf 2019	40	151	28.5	6.0	0.7 (0-80%)
BMW i3 2017	32	114	23.0	4.5	0.6 (0-80%)
Volkswagen eGolf 2018	24	125	17.0	6.5	1.0 (0-80%)

*Charging times of Level 1 and 2 are from empty to full in hours

charging rates. In regards to battery degradation, not only cell capacity decreases but also internal resistance tends to increase. Since cell's current SOH is assumed unknown, the internal resistance of the battery needs to be estimated. In estimating the resistance parameter, constant current charging data does not provide sufficient excitation for parameter identification; thus, it requires additional dataset apart from simple charging data.

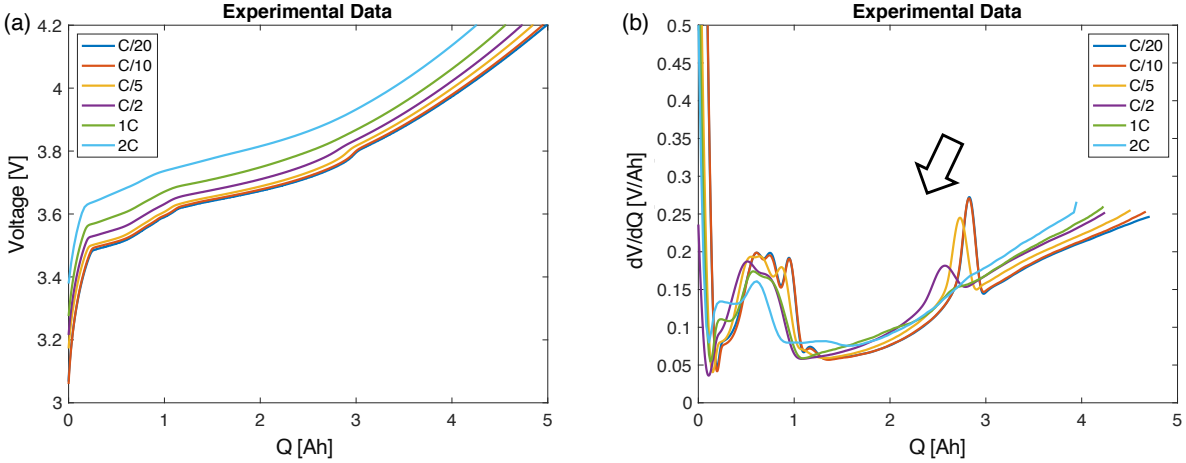


Figure 6.1: Experimental data of terminal voltage and differential voltage curves with increasing charging rates. (a) terminal voltage, (b) differential voltage (dV/dQ) showing the peak smoothing behavior.

6.3 Peak Smoothing with Increasing Current Rates

6.3.1 Peak Behavior Map

As can be seen in Fig. 6.1, as the C-rate increases there is an appreciable shift in the location and reduction of height for these peaks (called peak smoothing). Especially, the peak associated with the phase transition at a stoichiometry of $x = 0.5$ shows more smoothing than other local peaks. For instance, above 1C, the peak associated with the phase transition at $x = 0.5$ is effectively flattened and no longer observable.

Losing peak information at a high C-rate deteriorate the electrode SOH estimation because the peak is closely related to the graphite negative electrode. From this finding, we can set a boundary for the charging current rate in regards to the eSOH estimation and degradation diagnostics. In this section, the peak behavior is summarized as a peak behavior map with respect to the state-of-health of Li-ion cells and charging C-rates.

To study the degradation under a variety of conditions, 5 Ah NMC/graphite pouch cells were manufactured at the University of Michigan Battery Lab (UMBL). The cycle aging experiments were designed to cover an array of test conditions such as different charge/discharge C-rates, and different operating temperatures. The test conditions range from low C-rate room temperature baseline aging to high C-rate hot temperature accelerated aging. Each of the test conditions was performed at three different temperatures: hot ($45^{\circ}C$), cold ($-5^{\circ}C$), and room temperature ($25^{\circ}C$). Before the start of the cycling the cells were held at the target temperature for 3 hours to ensure thermal equilibrium. For peak dependency analysis, we select three cells cycle-aged with high

C-rate charge/discharge profile under different ambient temperature as summarized in Table 6.2.

Table 6.2: Cycle aging test condition matrix. The HT, RT, and CT corresponds to hot ($45^{\circ}C$), room ($25^{\circ}C$), and cold ($-5^{\circ}C$), temperature.

Cell ID	Ambient Temperature	Depth of Discharge	Charge	Discharge
HT	$45^{\circ}C$	0-100%	2C	2C
RT	$25^{\circ}C$	0-100%	2C	2C
CT	$-5^{\circ}C$	0-100%	2C	2C

The test conditions for C-rate dependency is summarized in Table 6.3. The pouch cells were installed in the fixture and put in a climate chamber with the temperature set to $25^{\circ}C$. The cell was charged with a constant current (CC) from the fully discharged state at different rates (C/20, C/10, C/5, C/2, 1C, and 2C) up to 4.2 V. The cell was discharged to 3 V with the same constant current rate of C/5 followed by a constant voltage (CV) period until the current dropped below C/40 to ensure the complete discharged state, followed by a rest of 3 hours for temperature equilibrium.

To understand the dependence of the peaks on C-rates, the amplitude and location of local peaks are investigated with the different constant charging current rates as shown in Fig. 6.2. First of all, local peaks are observable up to C/2, except the Peak 1 for Cold Temperature (CT) cells at 78% and 70% SOH levels. Beyond the end-of-life, Peak 1 from the CT cell is merged with other local peaks nearby into one, generating an inaccurate location. Above 1C, Peak 2 (related to the phase transition at a stoichiometry of $x = 0.5$) is flattened no information can be obtained. From this, we can set a conservative boundary for the robust peak information up to C/5 rate.

Comparing Peak 1 and Peak 2, Peak 2 shows more variations than that of Peak 1 in both amplitude and location as the C-rate increases. The amplitude decrease means the peak is flattened, making it unobservable, hence deteriorating the electrode-specific SOH estimation. Another interesting observation is that the location of the peak decreases (i.e. shift to the lower $Q[Ah]$) for both Peak 1 and Peak 2 as the cell's SOH level decreases (see Fig. 6.2(d) and (e)). It is important in eSOH estimation because the peaks in the differential voltage curve are directly connected to the graphite negative electrode parameters. From Ref. [54], the relationship between the peak location and the negative electrode parameters can be summarized as follows,

$$\hat{C}_n = \frac{|Q^1 - Q^2|}{|x^1 - x^2|}, \quad (6.1a)$$

$$\hat{x}_0 = x^1 - \frac{Q^1}{\hat{C}_n}. \quad (6.1b)$$

where Q^1 and Q^2 are the locations of the distinct peaks from the cell charge dV/dQ curve, and

Table 6.3: C-rate dependency test procedure.

Description	State	Controls	Current	Stop-criterion
Initialization	0	CC discharge	$C/5 = 1 \text{ A}$	$V < 3.0$
	1	CV at 3.0 V	variable	$I < C/40$
	2	Rest	0 A	$t > 3 \text{ hr}$
C/20 Charge	3	CC charge	$C/20 = 0.25 \text{ A}$	$V > 4.2$
	4	Rest	0 A	$t > 3 \text{ hr}$
Initialization	5	CC discharge	$C/5 = 1 \text{ A}$	$V < 3.0$
	6	CV at 3.0 V	variable	$I < C/40$
	7	Rest	0 A	$t > 3 \text{ hr}$
C/10 Charge	8	CC charge	$C/10 = 0.5 \text{ A}$	$V > 4.2$
	9	Rest	0 A	$t > 3 \text{ hr}$
Initialization	10	CC discharge	$C/5 = 1 \text{ A}$	$V < 3.0$
	11	CV at 3.0 V	variable	$I < C/40$
	12	Rest	0 A	$t > 3 \text{ hr}$
C/5 Charge	13	CC charge	$C/5 = 1 \text{ A}$	$V > 4.2$
	14	Rest	0 A	$t > 3 \text{ hr}$
Initialization	15	CC discharge	$C/5 = 1 \text{ A}$	$V < 3.0$
	16	CV at 3.0 V	variable	$I < C/40$
	17	Rest	0 A	$t > 3 \text{ hr}$
C/2 Charge	18	CC charge	$C/2 = 2.5 \text{ A}$	$V > 4.2$
	19	Rest	0 A	$t > 3 \text{ hr}$
Initialization	20	CC discharge	$C/5 = 1 \text{ A}$	$V < 3.0$
	21	CV at 3.0 V	variable	$I < C/40$
	22	Rest	0 A	$t > 3 \text{ hr}$
1C Charge	23	CC charge	$1C = 5 \text{ A}$	$V > 4.2$
	24	Rest	0 A	$t > 3 \text{ hr}$

the x^1 and x^2 are the stoichiometric states (i.e. negative electrode SOC) from the graphite negative electrode's differential voltage curve dU_n/dx . Here, the location of the peak of the cell is a measurement and the stoichiometric states are a priori known assuming the graphite negative electrode open-circuit potential, $U_n(x)$, is given.

In Eq. (6.1a), the negative electrode capacity, C_n , is estimated by the relative distance between

two peaks without knowing the exact the peak location, whereas the lower utilization window, x_0 , is dependent on the peak location, Q^1 . Therefore, although both peaks are shifting as the C-rate increases, it is worth checking the relative distance between the two for the negative electrode capacity estimation. Fig. 6.3 presents the peak distance with respect to the cell SOH and the C-rate. In can be seen that the peak distance shows less dependency on the C-rate than cell SOH, proving the usefulness of the peak distance at practical charging rate for eSOH estimation.

It is note that, with the finding from Fig. 6.3, the negative electrode capacity, C_n , is then estimated directly from the CC charge data up to $C/5$ without use of nonlinear least square estimation (i.e. voltage fitting for the electrode parameter estimation, $\theta = [C_p, C_n, y_{100}, x_{100}]$, in Chapter II). This separation of parameters reduces the number of the unknown in the nonlinear least square estimation, improving the estimation accuracy and making the eSOH estimation tractable at a practical charging rate.

6.3.2 Analysis on Peak Smoothing Phenomenon

In this section, first, the underlying physics of the peak smoothing behavior at increasing C-rate is studied with different electrochemical models, namely single-particle model (SPM), single-particle model with electrolyte (SPMe), and Dolye Fuller Newman (DFN) model. The electrochemical models basically describe the distribution of lithium concentrations inside a cell. Fuller *et al.* [30] developed a pseudo-two-dimensional (P2D) model (called DFN model after authors' name) assuming the electrode active materials as multiple spherical particles across the electrode thickness. Although the DFN model provides very accurate model prediction and internal dynamics, the model complexity and computational cost make this model difficult to use in control applications. To deal with the model complexity, many attempts have been made. For instance, Ning and Popov [70] proposed the single-particle model replacing each electrode with a single-spherical particle with no electrolyte dynamics based on the uniform current distribution across both electrodes. With the inclusion of electrolyte dynamics, the SPM has extended to the SPM_e [35, 82].

The model parameters are adopted from [66] for pouch cells built at the University of Michigan Battery Lab (UMBL). The cell chemistry is NMC/graphite, and the detailed specification of the battery can be found in [66]. For comparing the voltage prediction and the differential voltage (dV/dQ) curve for peak smoothing behavior, we used Python Battery Mathematical Modelling (PyBaMM) that solves physics-based electrochemical differential-algebraic equation models by using state-of-the-art automatic differentiation and numerical solvers [100]. In Fig. 6.4, a comparison of three electrochemical models' voltage and the experimental data is plotted at different charging rates (i.e. charging rate of $C/20$, $C/2$, and $1C$). Basically, three electrochemical models show a great match with the data for the constant-current charging mode.

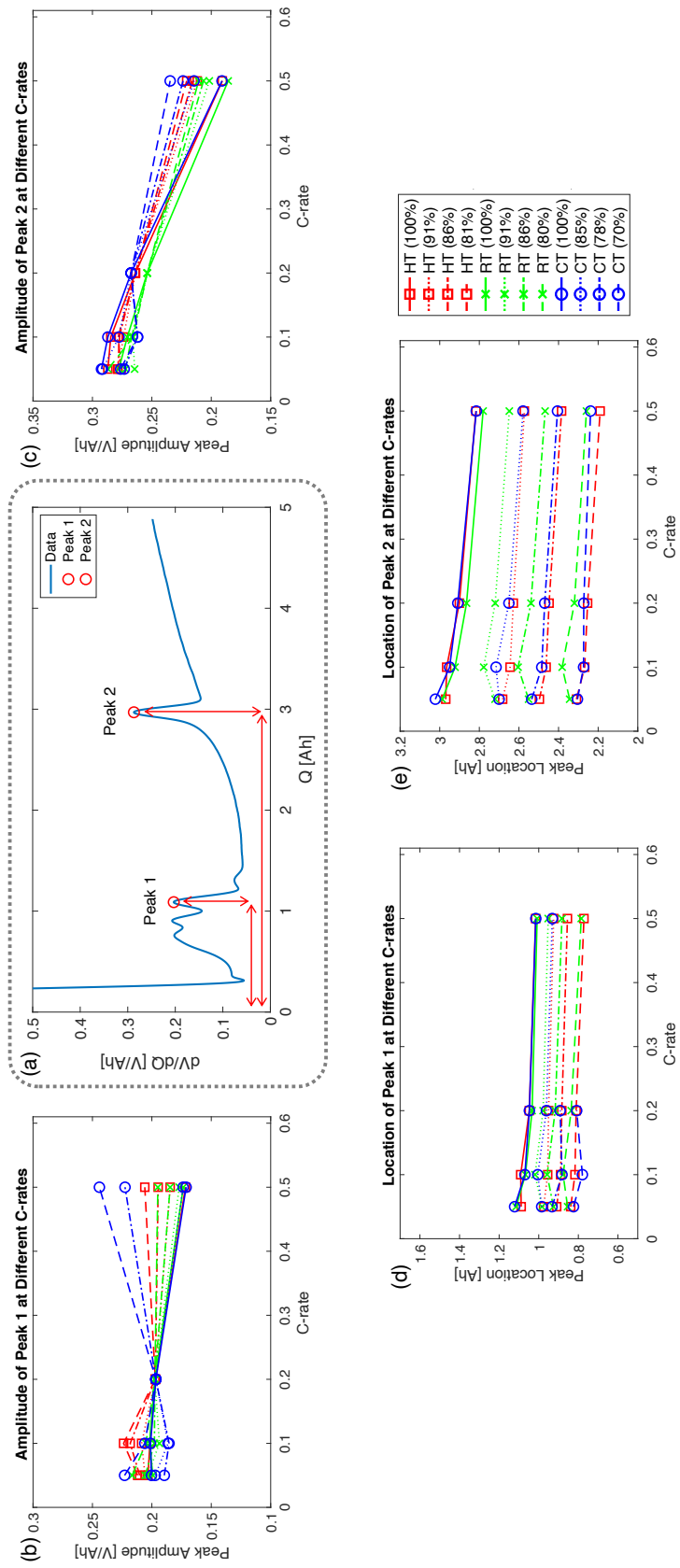


Figure 6.2: Peak behavior map with respect to charging rate for three different ambient temperatures. (a) Schematic of peak amplitude and location, (b) amplitude of Peak 1, (c) amplitude of Peak 2, (d) location of Peak 1, (e) location of Peak 2.

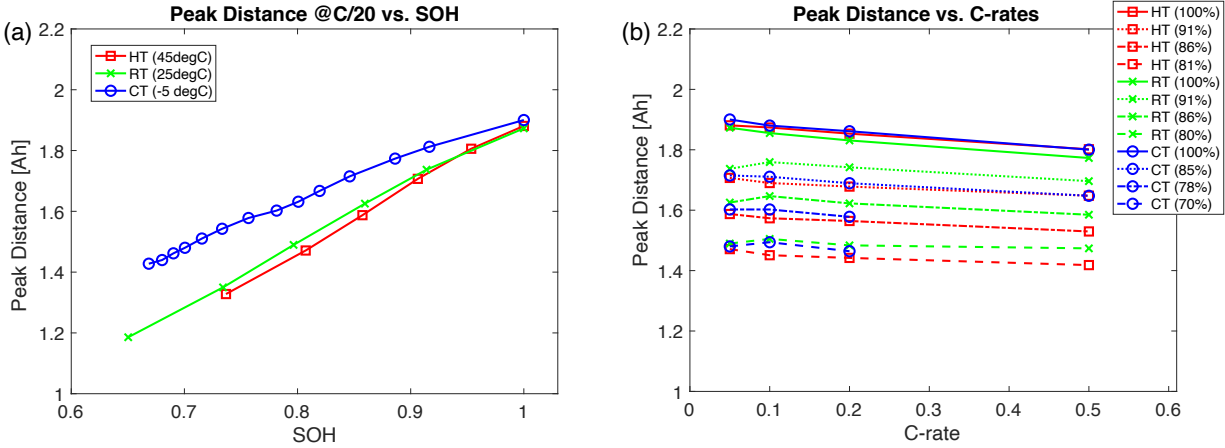


Figure 6.3: Peak distance with respect to cell state-of-health (SOH) and charging rate for three different ambient temperatures. (a) peak distance vs. cell SOH, (b) peak distance vs. C-rate (SOH of the cell is denoted in the bracket), showing less dependency on the C-rate than SOH.

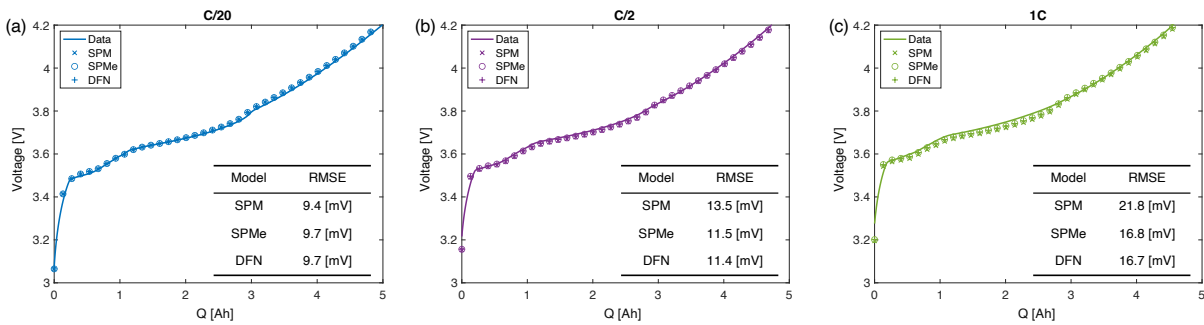


Figure 6.4: Comparison of the terminal voltage between the experimental data and three electrochemical models at different charging rates. (a) C/20, (b) C/2, (c) 1C. All of these models show a good match with the experimental data.

However, differentiating these models by looking at only the voltage response is difficult. The difference becomes clear when it comes to the peak behavior in the dV/dQ curve under different charging C-rates as shown in Fig. 6.5. Fig. 6.5(b), (d), and (f) show the dV/dQ curves with increasing charging rates from C/20 to 2C. Among the three models, only the DFN model is capable of capturing the peak smoothing phenomenon (i.e. peak widen and pressed while shifting to the lower capacity), whereas the SPM and SPMe models show only the peak shifting without smoothing. When comparing the single-particle type models and the DFN model, the biggest difference is the capability of capturing the lithium concentration distribution across the electrode thickness, where the former cannot, but the latter is capable. Since the peak in the dV/dQ curve is originated from graphite negative electrode, the surface concentration of lithium is further analyzed for the DFN model using the PyBaMM.

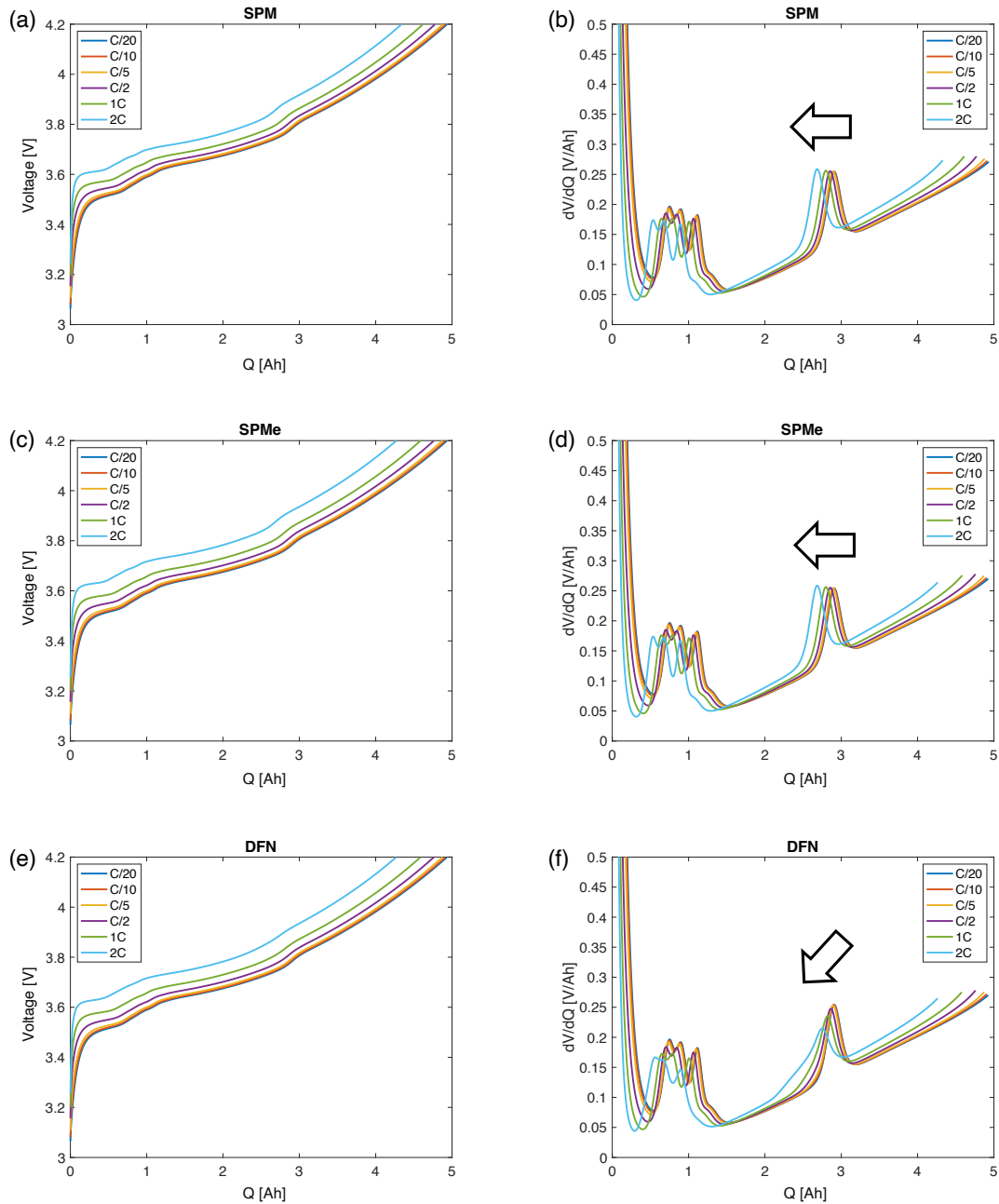


Figure 6.5: Simulation results of terminal voltage and differential voltage curves with increasing charging rates. (a) terminal voltage of SPM, (b) differential voltage of SPM with peak shifting, (c) terminal voltage of SPMe, (d) differential voltage of SPMe with peak shifting, (e) terminal voltage of DFN model, (f) differential voltage of DFN model showing the peak shifting and smoothing behavior.

The schematic of the DFN model is shown in Fig. 6.6(a) with the location of slicing for the surface concentration of lithium across the negative electrode (anode). As mentioned earlier, the

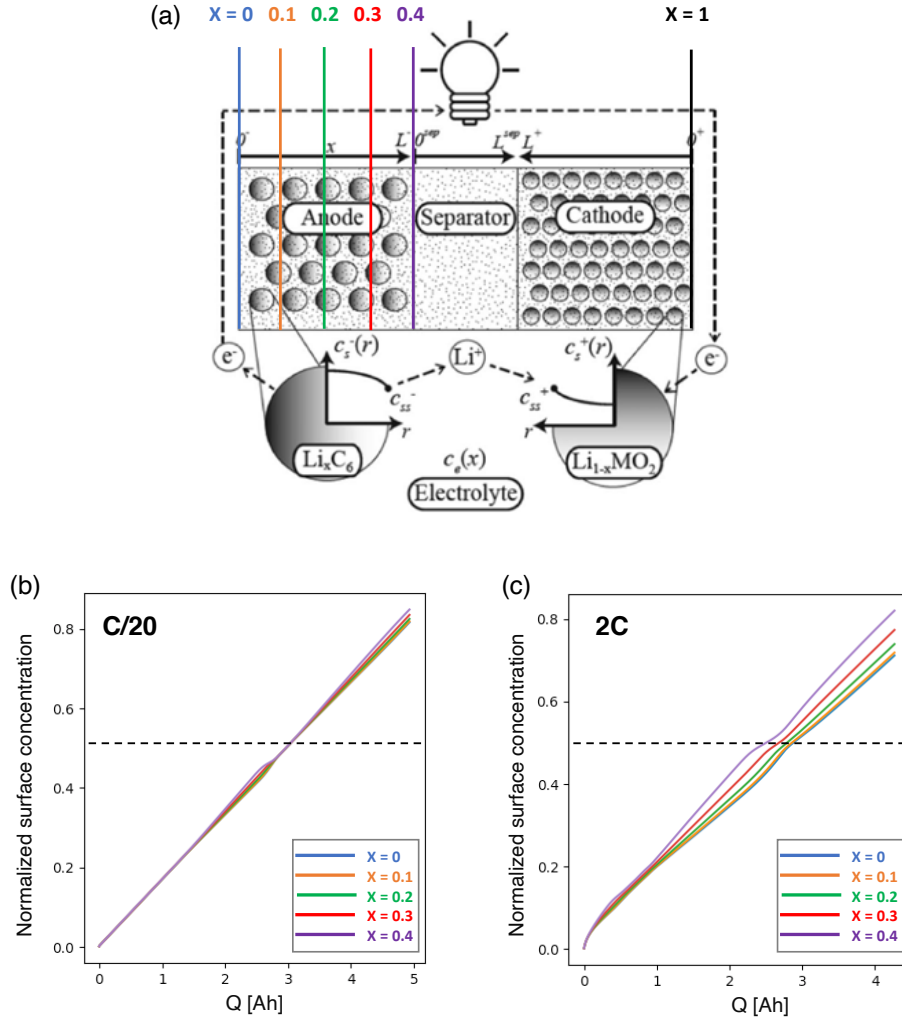


Figure 6.6: Simulation results of surface concentration of Li using DFN model. (a) Schematic of slicing for surface concentration of Li across negative electrode thickness, (b) surface concentration distribution of lithium at C/20 charge, (c) surface concentration distribution of lithium at 2C charge.

DFN model is capable of explaining the Li concentration difference in the electrode thickness, while the single-particle type models cannot. Hence, as shown in Fig. 6.6(b) and Fig. 6.6(c), the normalized surface Li concentrations of the graphite negative electrode at different locations have different values when the battery is being charged at a constant current. The Li concentrations begin with the uniform distribution initially; however, they diverge and converge during charging. Comparing the two charging rates, C/20 vs. 2C, it is found that the divergence of the surface concentration of lithium becomes large when a higher current is applied. Dashed lines in Fig. 6.6(b) and Fig. 6.6(c) indicate the phase transition for graphite at a stoichiometric state of $x = 0.5$, which corresponds to the peak showing the peak smoothing in the dV/dQ curve around 3 Ah. Because of the divergence of the Li concentration at high C-rates during charging, the phase transition of

the graphite negative electrode does not occur simultaneously, causing the peak smoothing.

Mohtat *et al.* [66] develop a multi-sized particle model to capture the smoothing behavior in the differential voltage curve at high C-rates. In [66], the connection between the particle size distribution and peak smoothing is also explained by the divergence between the particle surface concentrations associated with limits in the diffusion process; the particles surface concentration remain separated, where the smaller particles charge faster at the second plateau.

6.4 Overpotential due to Internal Resistance

Another consideration is the overpotential due to internal resistance. Since the electrode-specific SOH estimation relies on the cell's open-circuit voltage (OCV), the difference between the terminal voltage and the OCV needs to be modeled for a practical rate of charging scenario. Battery model parameters are often identified as a function of SOC and temperature for accurate voltage prediction; however, it increases the complexity of the model and makes the online parameter identification challenging under dynamic operation. For the case of the electrode SOH estimation, the overpotential can be simply modeled with the lumped constant resistance under constant current (CC) charging mode, assuming the resistance does not vary much over the commonly utilized SOC range of 20% - 90%.

With battery degradation, the internal resistance of a cell tends to increase; thus, it requires additional parameter estimation for the internal resistance besides the electrode SOH estimation. Treating the cell internal resistance as an additional unknown on top of the electrode SOH parameters makes the whole parameter set less identifiable due to the increased number of unknown parameters. Furthermore, for a constant current charging scenario, the resistance parameter does not have sufficient excitation, resulting in poor estimation results [61]. Therefore, it is advisable to separate the parameter estimation into two sub-problems based on the battery's operation mode: 1) resistance estimation using transient data, 2) electrode SOH estimation using CC charge data.

6.4.1 Battery model

For the problem of identifying the internal resistance of a cell, an equivalent circuit model with a single RC pair is used to capture the battery's voltage dynamics.

Consider the OCV-R-RC equivalent circuit model in discrete-time,

$$\begin{aligned}
SOC(k+1) &= SOC(k) - \frac{\Delta T}{3600C_{bat}}I(k), \\
V_1(k+1) &= \left(1 - \frac{\Delta T}{R_1C_1}\right)V_1(k) + \frac{\Delta T}{C_1}I(k), \\
V_t(k) &= V_{oc}(SOC(k)) - V_1(k) - R_0I(k),
\end{aligned} \tag{6.2}$$

where C_{bat} is the cell capacity and $I > 0$ for discharging. Typically, the resistance R_0, R_1 and capacitance C_1 vary with SOC, current direction, and temperature; however, they are assumed to be a constant in the following analyses.

6.4.2 Sensitivity-based Least Square Estimation

In this section, the method for estimating the resistance parameters is presented. Since we need a lumped resistance for the electrode SOH estimation, the ordinary least square estimation is used. From the equivalent circuit model in Eq. (6.2), we can rewrite the equations in a linear regression form with the new output signal, $y(k) = V_{oc}(SOC(k)) - V_t(k)$, representing the voltage difference between the open-circuit voltage and the terminal voltage. The value of $y(k)$ can be computed based on measurements and the known OCV model. Specifically, the $SOC(k)$ can be obtained by integrating current and scaling the integral to SOC using the cell capacity, and the corresponding $V_{oc}(SOC(k))$ is based on the OCV-SOC relationship.

With the new output, $y(k)$, an ARX (Auto-Regression with eXogenous inputs) equation can be derived through time shift and algebraic manipulations,

$$\begin{aligned}
y(k) &= V_1(k) + R_0I(k), \\
V_1(k) &= \left(1 - \frac{\Delta T}{R_1C_1}\right)V_1(k-1) + \frac{\Delta T}{C_1}I(k-1),
\end{aligned} \tag{6.3}$$

and thus

$$y(k) = \left(1 - \frac{\Delta T}{R_1C_1}\right)V_1(k-1) + \frac{\Delta T}{C_1}I(k-1) + R_0I(k). \tag{6.4}$$

By replacing $V_1(k-1)$ with $y(k-1)$ and $I(k-1)$,

$$V_1(k-1) = y(k-1) - R_0I(k-1). \tag{6.5}$$

Then, Eq. (6.4) can be written

$$\begin{aligned}
y(k) &= \left(1 - \frac{\Delta T}{R_1 C_1}\right)[y(k-1) - R_0 I(k-1)] + \frac{\Delta T}{C_1} I(k-1) + R_0 I(k) \\
&= \left(1 - \frac{\Delta T}{R_1 C_1}\right)y(k-1) + \frac{(R_0 + R_1)\Delta T - R_0 R_1 C_1}{R_1 C_1} I(k-1) + R_0 I(k) \\
&= a_0 y(k-1) + b_0 I(k-1) + b_1 I(k).
\end{aligned} \tag{6.6}$$

where

$$a_0 = 1 - \frac{\Delta T}{R_1 C_1}, \quad b_0 = \frac{(R_0 + R_1)\Delta T - R_0 R_1 C_1}{R_1 C_1}, \quad b_1 = R_0. \tag{6.7}$$

A parametric linear regression form can then be obtained as

$$y(k) = \theta^T \phi(k), \tag{6.8}$$

where

$$\theta = [a_0, b_0, b_1]^T, \quad \phi(k) = [y(k-1), I(k-1), I(k)]^T. \tag{6.9}$$

This linear regression equation can also be written in matrix notation as

$$Y = \Phi \theta, \tag{6.10}$$

where Y is $N \times 1$ vector of the output signals, Φ is a $N \times 3$ matrix of regressor, and N is the size of data window for LS estimation

$$Y = \begin{bmatrix} y(1) \\ y(2) \\ \dots \\ y(N) \end{bmatrix}, \quad \Phi = \begin{bmatrix} \phi^T(1) \\ \phi^T(2) \\ \dots \\ \phi^T(N) \end{bmatrix} \tag{6.11}$$

The parameters, θ , can be identified by solving the least square problem:

$$\hat{\theta} = (\Phi^T \Phi)^{-1} (\Phi^T Y). \tag{6.12}$$

Now, the problem is how to collect the measurement of voltage and current from a transient discharge cycle. The conventional estimation methods tend to use all of the data points for estimating variables. There exist several challenges in implementing this LS estimation in real-world applications. First, not all data points are sensitive to the target parameters to estimate. Using insensitive data can cause significant estimation errors due to unknown disturbances such as mea-

surement noise and model uncertainty. Unlike the lab setting where the current and voltage data cannot be designed or controlled, estimating the resistance parameter in a real-world case needs to use unpredictable random data collected online. Secondly, the number of data points in a batch LS estimation can be limited by the onboard BMS memory. With a typical sampling rate of 1 Hz or 10 Hz in automotive applications, several hours of drive cycle data might require a lot of memory for onboard BMS to store and process it. Therefore, in this work, the analytic sensitivity and data selection strategy is proposed. Sensitivity is the relationship between the variation of output voltage and that of the unknown parameter to identify, defined as

$$S = \frac{\partial V}{\partial \theta}. \quad (6.13)$$

A higher sensitivity value means a stronger correlation between the output and the parameter. Using highly sensitive data for estimation will yield good accuracy, demonstrated by the Fisher information matrix and Cramer-Rao bound analysis [52]. The data selection strategy is motivated by Ref. [60] where the analytic expressions of the sensitivity of equivalent circuit parameters are introduced. The key idea is to determine if the incoming data is sensitive enough or not for each parameter, and extract only the favorable data points (i.e. selecting data points that show higher sensitivity than the sensitivity threshold) that could improve the estimation quality and reduce the number of data points required.

In [59], the sensitivities of the target variables R_1 and τ_1 have been derived in a compact form as explicit functions of generic current sequence, I , based on continuous-time model and Laplace transform,

$$\begin{aligned} S^{R_0} &= \frac{\partial V}{\partial R_0}(t) = -I(t), \\ S^{R_1} &= \frac{\partial V}{\partial R_1}(t) = \mathcal{L}^{-1}\left\{\frac{1}{1 + \tau_1 s}\right\} * I(t), \\ S^{\tau_1} &= \frac{\partial V}{\partial \tau_1}(t) = \mathcal{L}^{-1}\left\{-\frac{R_1 s}{(1 + \tau_1 s)^2}\right\} * I(t), \end{aligned} \quad (6.14)$$

where \mathcal{L}^{-1} stands for the inverse Laplace transform, s is the complex frequency variable, and $*$ represents convolution. These expressions can be conveniently used to calculate the sensitivity of data points in any measurement sequence in real time through the realization of state-space form.

Note that, with the sensitivity-based data selection algorithm, N in Eq. (6.11) indicates the number of the pre-selected data points. Thus, data points in the vector Y and the regressor matrix Φ do not have to be in series measurements. Instead, it only requires current time and previous time's voltage and current measurements.

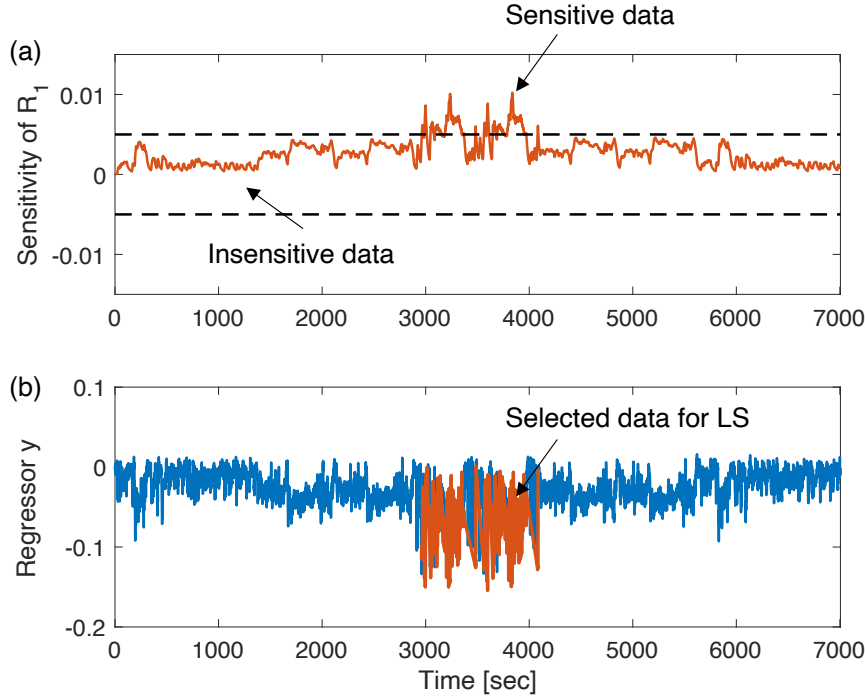


Figure 6.7: Example of sensitivity-based data selection strategy. (a) sensitivity of data points for resistance R_1 , (b) selected data points.

6.4.3 Adaptive Algorithm

Fig. 6.8 illustrates the workflow of the proposed adaptive parameter estimation algorithm. Depending on the battery operation mode, the parameter estimation is conducted separately in two different threads. The resistance parameter θ_1 is estimated from transient data such as the drive cycle of an electric vehicle. Estimation is performed by ordinary least square (OLS) estimation as a batch process, but only data points with higher sensitivity are selected. To be specific, in the upper pipeline in Fig. 6.8, only a window of data points is used in the LS estimation through the sensitivity-based data selection algorithm from the transient data. Since the least square estimation operates once with the fixed sized data window, we call it as window LS estimation.

Once the battery is on charge mode, the lumped resistance, $R_{total} = R_0 + R_1$, is then provided to the electrode SOH (eSOH) estimator that is also conducted in a batch process using nonlinear least square. With more accurate resistance information, the eSOH estimation accuracy improves. Since the eSOH estimation is associated with equality constraints, *fmincon* in MATLAB is used. Detailed procedures of the eSOH estimation can be found in [54].

Since the resistance parameter estimation is based on the known OCV model, the output of the eSOH estimation, $V_{oc}(SOC)$, C_{bat} , and θ_2 in the lower pipeline in Fig. 6.8 is provided to the

internal resistance estimation block as a feedback for updating the resistance parameter estimate when the next drive cycle data is available.

The proposed framework works as an adaptive process because the update of the two sets of parameter estimates, $\theta_1 = [R_0, R_1]$ and $\theta_2 = [C_p, C_n, y_{100}, x_{100}]$, is performed separately and dependent on each other at the time of parameter estimation. Therefore, this adaptive process should be regularly executed when the new data is provided.

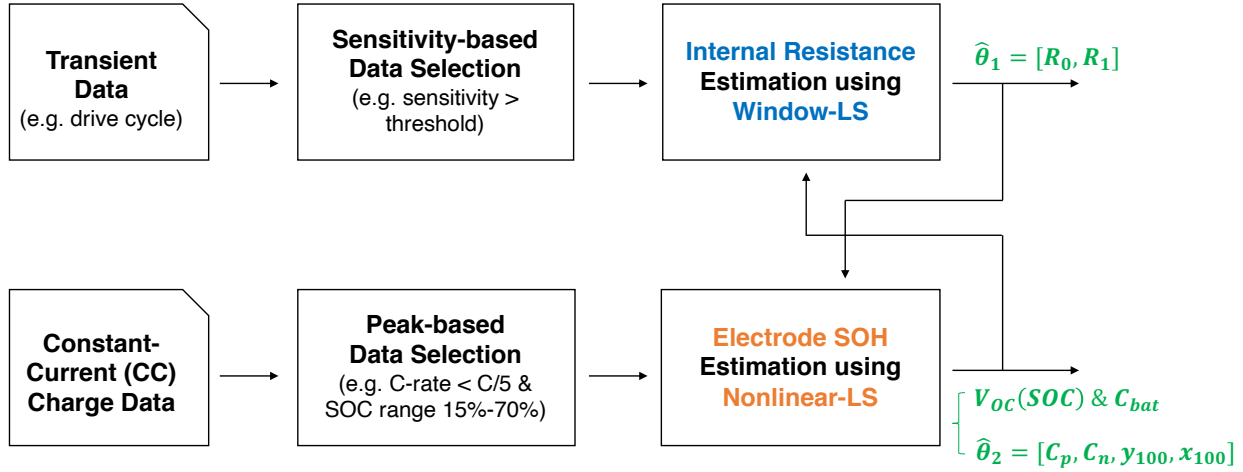


Figure 6.8: Proposed framework with an adaptive parameter estimation from two separate datasets. The resistance parameters are estimated using transient data and the electrode SOH parameters are estimated from constant-current charge data. Both estimations pre-select data points to improve the estimation accuracy.

6.5 Results and Discussion

6.5.1 Resistance Estimation via Window Least Square Estimation

The resistance parameters are identified using the least square estimation method in Eq. (6.11) such that N data points are selected from the transient data through sensitivity criterion. Sensitivity calculation is realized from the Laplace domain to the discrete-time domain via state-space realization of the transfer function in Eq. (6.14). The initial current is zero; thus, the initial sensitivity is set to zero.

The effectiveness of the sensitivity data selection is studied with a single RC equivalent circuit model (i.e. OCV-R-RC model in Eq. (6.2)) and transient data generated from a synthetic drive cycle and additive Gaussian white noise. The synthetic drive cycle is composed of several standard drive cycles based on a home-to-work/work-to-home commute scenario. Drive cycle and

corresponding required current profile was obtained by using Advisor (A user-friendly advanced powertrain simulation software developed at National Renewable Energy Laboratory) [114] assuming driving a BMW i3 2018 with 33 kWh battery pack. The EPA standard drive cycles used for the synthetic drive cycle are UDDS (Urban Dynamometer Driving Schedule), HWFET (Highway Fuel Economy Test), and US06 (one of Supplemental Federal Test Procedure, SFTP). The UDDS represents city driving conditions, HWFET is used to determine the highway fuel economy rating, and SFTP US06 combines the current city and highway cycles to reflect real-world fuel economy more accurately that has a high speed, quick acceleration, and four stops. As shown in Fig. 6.9, US06 has more frequent large spikes in current profile than the other two, and HWFET has a higher average current than UDDS, reflecting the highway driving condition. This dynamic current profile provides different sensitivity for each parameter in Eq. (6.14) depending on the magnitude of the current and the fixed current holding time.

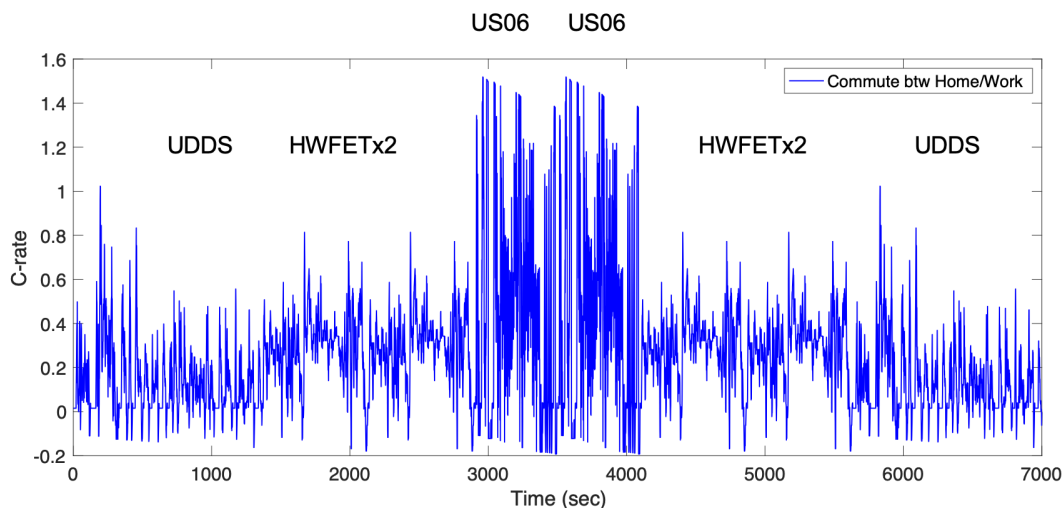


Figure 6.9: Current profile of synthetic drive cycle. This profile is assumed for a home-to-work/work-to-home commute scenario for a battery electric vehicle (BMW i3 2018 with 33 kWh battery pack).

The normalized sensitivity values from the given synthetic drive cycle are presented in Fig. 6.10. Comparing Fig. 6.9 and Fig. 6.10, it is found that the sensitivity value has a dependency on the drive cycle that battery cell is operated on. Generally, higher current values provide higher sensitivity for the model parameters. We can evaluate the identifiability of the model parameter based on the magnitude of the normalized sensitivity in Fig. 6.10. The ohmic resistance, R_0 is the most sensitive, the resistance in RC pair, R_1 , is the second, and the time constant, $\tau = R_1 C_1$, is the least sensitive. A higher sensitivity means a stronger correlation between the output and the parameter; hence, a better identifiability.

The sensitivity threshold is arbitrary, meaning there is no rule of thumb for determining its

value. We can set up different values of the threshold for different parameters. Based on the threshold value, the number of selected data points can be different. A more conservative threshold (i.e. lower threshold value) would take more data points, but it decreases the overall sensitivity of the dataset. On the other hand, an aggressive threshold results in a small number of data points that make the window LS vulnerable. However, one good practice is identifying the battery model parameters when it is fresh state and applying a variety of standard drive cycles to find the optimal value for a robust and accurate resistance estimation. Note that the overarching goal is to select only the favorable data points that could improve the estimation quality and reduce the number of data points required.

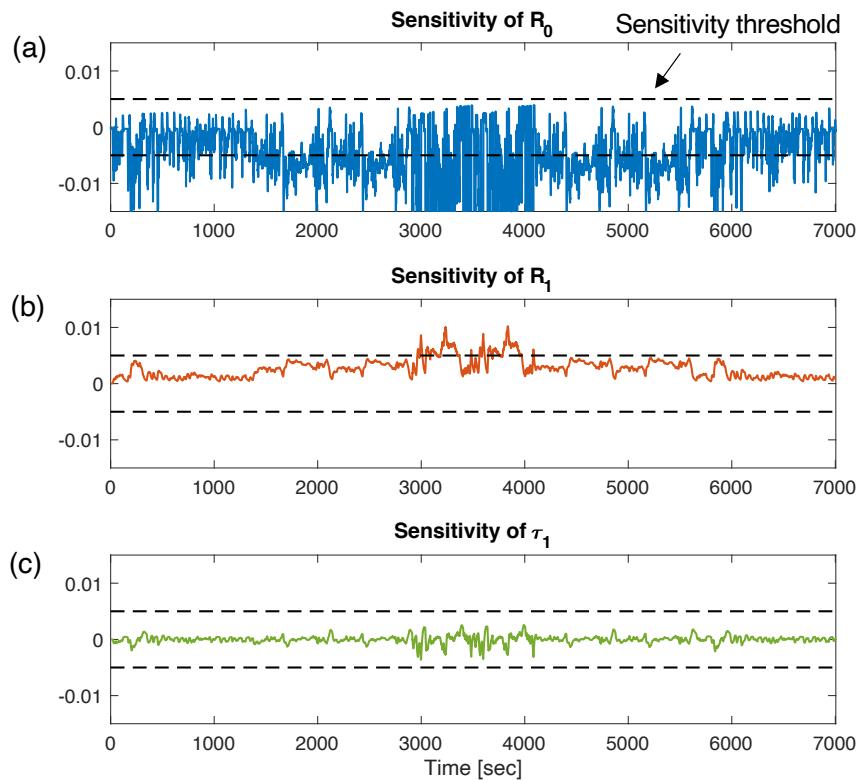


Figure 6.10: Sensitivity of equivalent circuit parameters with synthetic drive cycle. Sensitivity values show drive cycle dependency.

To examine the impact of the data-selection strategy in resistance estimation, a simulation study is performed based on a known model with the synthetic drive cycle shown in Fig. 6.9. First, the current profile is applied to the model to predict the terminal voltage added with Gaussian white noise with a standard deviation of 5 mV for a real-world voltage sensor accuracy. The sensitivity values are computed in real-time from Eq. (6.14) to store data points that pass the sensitivity threshold for the window LS estimation. Since the additive noise is random, the estimation accu-

racy is evaluated via Monte Carlo simulation with 1,000 iterations. Finally, the error statistics (e.g. mean and standard deviation of the estimation error) are plotted.

The mean and standard deviation of estimation errors ($\mu \pm \sigma$) of the equivalent circuit model parameters are plotted in Fig. 6.11. Note that each plot is not in the same scale. The estimation results agree with the notion of identifiability from the average sensitivity in Fig. 6.10 in that the ohmic resistance, R_0 , shows the smallest error in average, then the resistance in a RC pair, R_1 , lastly the time constant, τ_1 shows the largest error in average. In terms of the effectiveness of the data selection, RC pair's parameters, R_1 and τ_1 , are significantly improved with the data selection strategy.

In summary, the contributions of the sensitivity-based data selection are threefold. 1) the estimation accuracy is improved by selecting the sensitive data from transient data, 2) the estimation is no longer dependent on the drive cycle and more robust, and 3) it helps reduce the number of data points used in LS estimation, tractable for onboard applications.

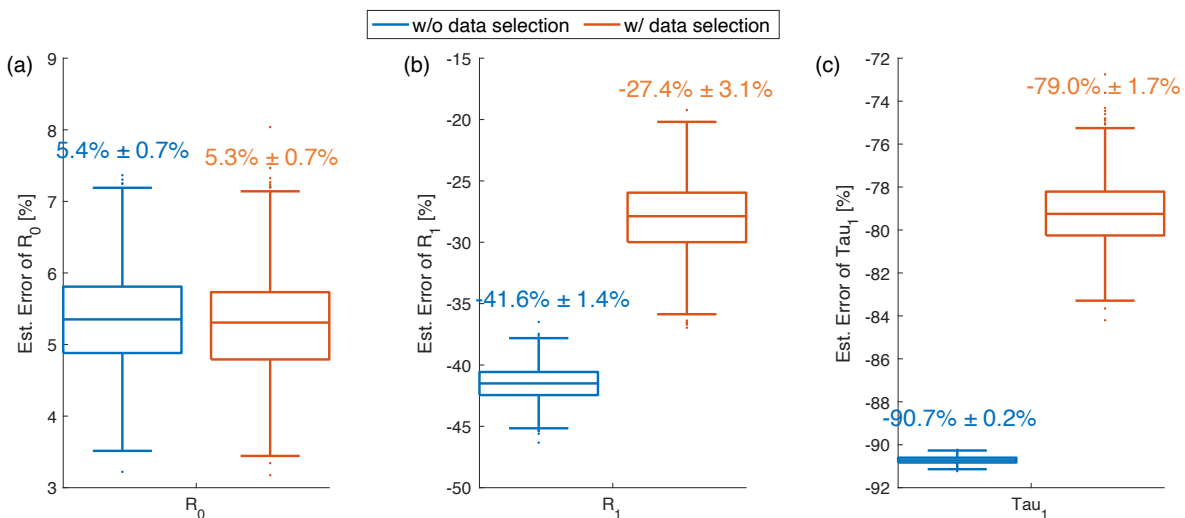


Figure 6.11: Estimation error statistic (i.e. mean and standard deviation) of equivalent circuit model parameters with and without data selection strategy. (a) ohmic resistance R_0 , (b) RC pair resistance R_1 , (c) RC pair time constant τ_1 .

6.5.2 Electrode SOH Estimation Error due to Inaccurate Resistance

Although the data selection strategy improves the quality of estimation, it still can result in an estimation error for the resistance parameters (see Fig. 6.11). Especially, an accurate estimate of RC pair resistance, R_1 , is challenging and an on-going research topic. Another issue is a modeling

error, which includes many aspects. For instance, with more rigorous identification of parameters, the equivalent circuit model parameters are typically modeled as a function of SOC and temperature. This study assumes a constant value for the model parameters by removing SOC dependence, and assuming temperature is controlled within a reasonable bound. Furthermore, a difference in the parameter value can exist depending on the charge and discharge operation mode. In [76], an equivalent circuit model with different parameters for charge and discharge is developed for lithium iron phosphate (LFP)/graphite cell. Hence, we should understand the impact of inaccurate resistance to the electrode SOH estimation for a robust and reliable algorithm.

In this analysis, the estimation is focused on the electrode-specific parameters such as electrode capacity and utilization range, $\theta_2 = [C_p, C_n, y_{100}, x_{100}]$. First, CC charge data is generated from a known model under C/5 rate. Then, the electrode parameter estimation is performed using nonlinear least square (NLS) as illustrated in Eq. (2.12) while varying the resistance parameter values. Under constant current charging mode, the overpotential due to internal resistance can be modeled as a lumped ohmic drop, $\Delta V = I \times (R_0 + R_1) = I \times R_s$, with the equivalent series resistance, R_s . Thus, the inaccurate resistance means the error in the lumped resistance, $R_s = R_0 + R_1$. This analysis aims to understand how much error will occur for the electrode-specific parameters when the resistance estimate is inaccurate. Therefore, the estimation errors of the electrode parameters and corresponding cell capacity are plotted with respect to the percentage error of the lumped resistance.

Fig. 6.12 shows the estimation error of the electrode parameters and cell capacity to the lumped resistance error ranging from -50% to +50%. It is found that the positive electrode (PE) parameters such as PE capacity, C_p , and the PE lower utilization range, y_0 , are the most sensitive to the resistance error. For a cell with NMC/graphite chemistry, the NMC PE dominates for the overall cell voltage, where the graphite negative electrode (NE) shows mostly plateaus. Therefore, inaccurate resistance affects mainly the PE parameters. Another interesting observation is that even with a large error in the resistance, negative electrode parameters and cell capacity are still estimated with reasonable accuracy. For instance, a 50% error in the resistance induces less than 0.5% error for the NE capacity and less than 1% error for the cell capacity. It is worth noting that there is no measurement noise or modeling error considered in order to check the sole impact of the inaccurate resistance. One reasoning for the accurate estimation of the NE parameters is that the peak distance is independent of the resistance value. To sum up, from this simulation study, the impact of the resistance error on the electrode parameter estimates is acceptable, verifying the robustness of the adaptive algorithm.

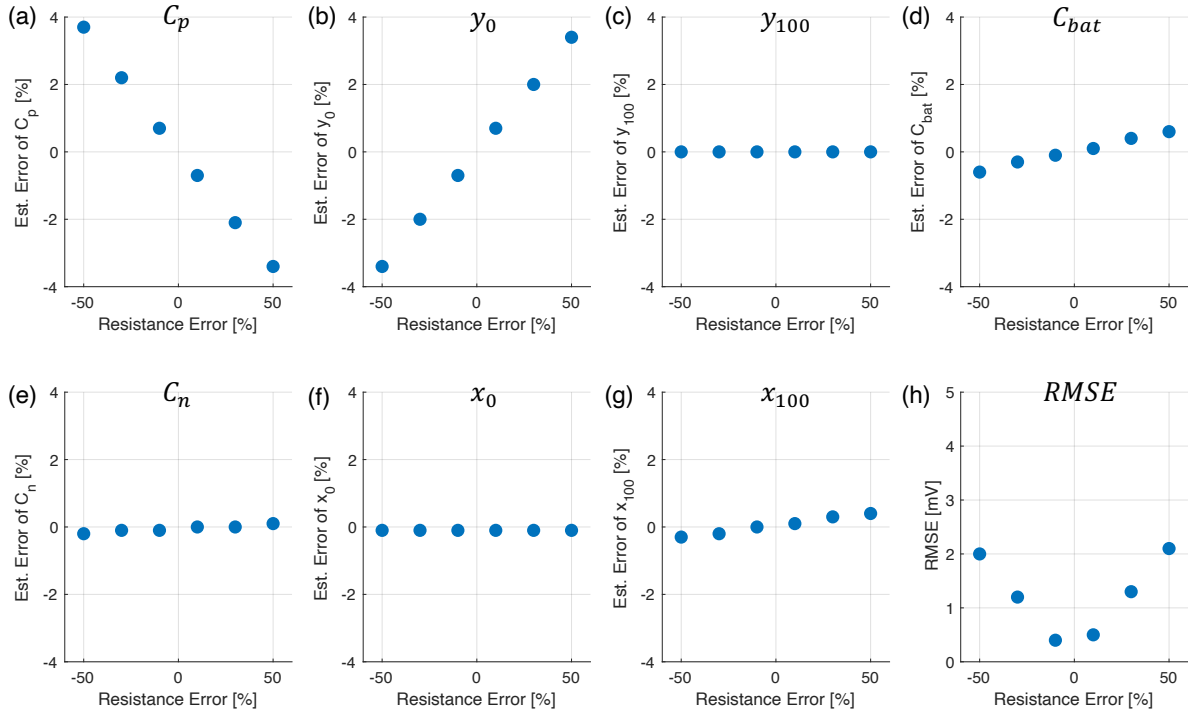


Figure 6.12: Estimation error of electrode parameters with respect to resistance error. (a) estimation error of positive electrode capacity, (b) estimation error of positive electrode lower utilization range, (c) estimation error of positive electrode upper utilization range, (d) estimation error of cell capacity, (e) estimation error of negative electrode capacity, (f) estimation error of negative electrode lower utilization range, (g) estimation error of negative electrode upper utilization range, (h) root-mean-square-error for voltage fit.

6.6 Conclusion

In this chapter, the feasibility of the electrode-specific SOH estimation is analyzed considering a real-world charging scenario. First, the peak behavior map is constructed from comprehensive aging test data. It is found that the peak distance does not change much with increasing C-rate up to $C/5$, enabling the negative electrode capacity estimation directly from the measured data at a practical charging rate. Secondly, the peak smoothing behavior with increasing C-rate is investigated using electrochemical models to understand this phenomenon's root cause. The non-uniformity of the graphite negative electrode's surface concentration across the electrode thickness is found to be causing the phase transition out of synchronized; thus, the peak smooths out. Third, the method of estimating the resistance parameter is introduced to deal with the overpotential due to the internal resistance during the constant current charging mode. Finally, the overall algorithm for the electrode SOH estimation is proposed integrating the comprehensive estimation procedures.

CHAPTER 7

Physics-Guided Machine Learning for Battery Diagnostics and Prognostics

7.1 Introduction

Recent data-driven machine learning approaches have shown great potential in battery state of health (SOH) estimation and cycle life or remaining useful life (RUL) prediction. Diagnostic information on battery degradation allows for its maximum utilization while avoiding unfavorable or even dangerous operations. Furthermore, advancements in lifetime prediction lead to predictive maintenance and extend the opportunity for second-life applications.

In the data-driven approach, often called the black-box approach, very little or no prior understanding of the Li-ion battery's physical degradation is required. Instead, data-driven models attempt to find a correlation between the given input and output data. For battery diagnostics and prognostics, the input data is typically battery operational data, including voltage, current, temperature, or some features extracted from such battery data. And the output data is the battery SOH or cycle life.

Although these machine learning approaches are gaining more attention due to their easy accessibility with open-source software and remarkable improvements in computing power and data management platforms, it still has some challenges. For instance, without knowledge of battery degradation, establishing input and output data from experiments can be arbitrary and time-consuming. Furthermore, it could be challenging to interpret the results of data-driven methods without knowledge of the underlying physics.

In this work, two case studies are presented to show how physics can guide data-driven machine learning algorithms in battery degradation diagnostics and prognostics. The first case study is the electrode-specific degradation diagnostics using the generated aged data and electrochemical features extracted from the differential curves. In this example, the data-driven diagnostic model specifically benefits from training/testing dataset preparation and feature selection [49]. The second case study is about the early prediction of battery cycle life [101], where it only uses the first

few cycle data to predict the lifetime of the battery down to end-of-life. In this example, a predictive algorithm motivated by a recent work [95] is applied to different chemistry battery cell with diverse aging conditions.

This chapter is organized as follows; Section 7.2 presents the first case study on the electrode degradation diagnostics using an artificial neural network model. Section 7.3 introduces the second case study on the early prediction of battery cycle life with feature extraction in the discharge voltage curve and ridge regression model. Lastly, Section 7.4 summarizes the contributions of the physics-guided machine learning.

7.2 Case Study 1: Electrode Degradation Diagnostics using Neural Network

7.2.1 Background

In terms of electrode-level degradation of a Li-ion battery, sets of degradation mechanisms can be clustered into so-called degradation modes. There are three commonly accepted degradation modes: loss of lithium inventory (LLI), loss of active positive electrode material (LAM_{PE}), and loss of active negative electrode material (LAM_{NE}) [26, 8]. These three degradation modes [LAM_{PE}, LAM_{NE}, LLI] are closely related to the changes in the electrode SOH parameters $\theta = [C_p, C_n, y_0, x_0]$, i.e., electrode capacity and utilization range, where the parametric OCV model can be written as follows

$$V_{oc}(Q; \theta) = U_p \left(y_0 - \frac{Q}{C_p} \right) - U_n \left(x_0 + \frac{Q}{C_n} \right). \quad (7.1)$$

In the model-based approach, the electrode-specific degradation diagnostics is formulated as a parameter identification problem finding a proper set of electrode parameters, θ , such that the error between the model and data is minimized as described in Chapter 2.

However, there exist some challenges to solve this nonlinear least-squares problem in onboard applications. Since the OCV model is nonlinear, the parameter identification becomes a non-convex optimization problem and thus local minima could exist. One way to address this non-convexity is to run a solver with various initial points and finding multiple local minima. This procedure requires a decent optimization solver with multiple running; thus, it increases computational cost.

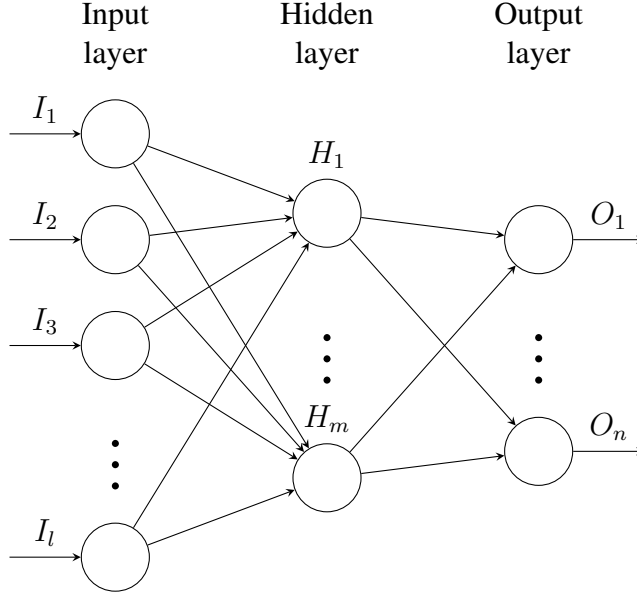


Figure 7.1: Schematic structure for a three layer feed-forward neural network.

7.2.2 Proposed Data-driven Method using Neural Network

To avoid the complex optimization problem, we propose a machine learning-based approach for electrode-level Li-ion battery degradation diagnostics using a multi-layer feed-forward neural network model with the electrochemical features. An artificial neural network (ANN) is an interconnected group of nodes (see Fig. 7.1). Each circular node represents an artificial neuron, and an arrow represents a connection from the output of one neuron to the input of another. The input layer is composed of electrochemical features extracted from the differential analysis. Final outputs represent the percentage degree of three different degradation modes [LAM_{PE} , LAM_{NE} , LLI].

7.2.3 Degradation Simulation and Electrochemical Features

In terms of battery degradation, the resulting degree of three degradation modes, [LAM_{PE} , LAM_{NE} , LLI], can be arbitrary depending on the battery usage and storage conditions. Covering all different combinations of degradation requires extensive aging tests, which cost a substantial amount of time and effort. Instead of conducting numerous aging testing, we can generate aged cell's OCV curve based on the physical-model in Eq. (7.1) by changing the electrode SOH parameters, $\theta = [C_p, C_n, y_0, x_0]$, for different degree of degradation. For example, 10% LAM_{PE} can be simulated by reducing the positive electrode capacity C_p by 10% from the nominal value. It is worth mentioning that simulating aged cell data is valid only when the half-cell potentials of both electrodes are accurately known. Aging simulation can also be performed by an open-source toolbox named

'Alawa' [26].

Table 7.1: Nominal parameters for a LFP/graphite cell

	Parameters	Values
Full-Cell	C	2.30 Ah
	V_{max}	3.6 V
	V_{min}	2.5 V
Positive Electrode	C_p	2.50 Ah
	$[y_0, y_{100}]$	[0.95, 0.02]
Negative Electrode	C_n	2.89 Ah
	$[x_0, x_{100}]$	[0.04, 0.83]

As a source of training and testing dataset, all possible combinations of three independent degradation modes [LAM_{PE}, LAM_{NE}, LLI] are simulated for a LFP/graphite cell. The nominal parameters to represent the cell's fresh condition are provided in Table 7.1. Aged cell data are generated in two ways; a sole degradation mode and a combined mode. First, the sole degradation mode is simulated to have a clear demonstration of different patterns in the differential curves for each degradation mode. Figure 7.2 summarizes the evolution of the OCV curve and differential curves. Degradation level ranges from 1% to 10% with 1% increment, which produces 30 data sets for three modes.

- LAM_{PE}: PE capacity C_p is reduced and NE capacity C_n is fixed. This reduction leads to changes in utilization range x_0 and y_0 .
- LAM_{NE}: NE capacity C_n is reduced and PE capacity C_p is fixed. This reduction leads to changes in utilization range x_0 and y_0 .
- LLI: Reduction in utilization range without any changes in electrode capacity C_p and C_n .

However, degradation of real batteries can be more complicated than a single degradation mode. A cell could undergo a mixture of degradation modes at different levels, that makes it challenging to accurately identify the individual degradation modes. To emulate a realistic scenario of an aged cell, the combined degradation case is also simulated. For the given parameters and cell chemistry, it is found that some features start to disappear above 10% of degradation level, which makes the NN losing input features. Thus, in this study, the degradation level is set until each degradation mode reaches to 10% degradation as summarized in Table 7.2. It should be noted

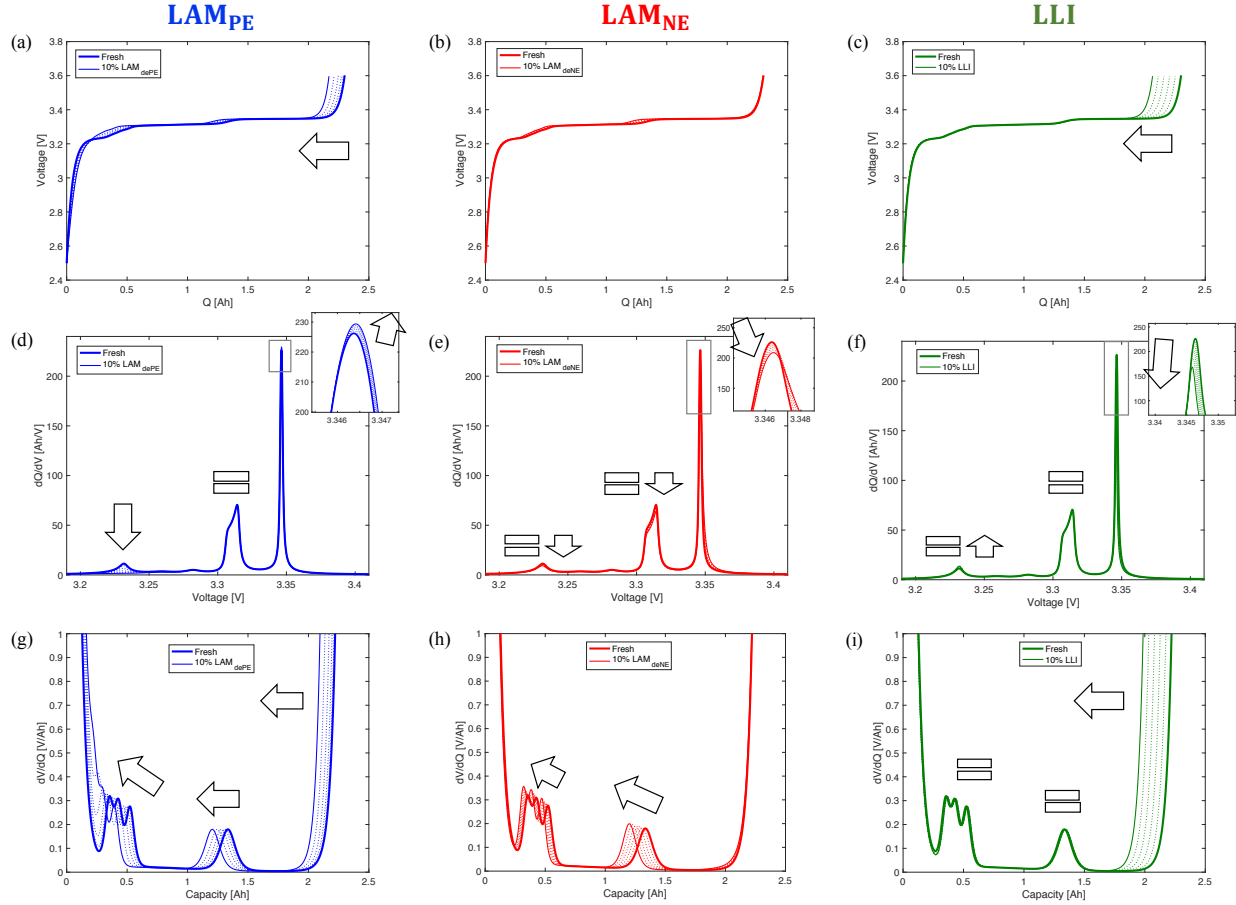


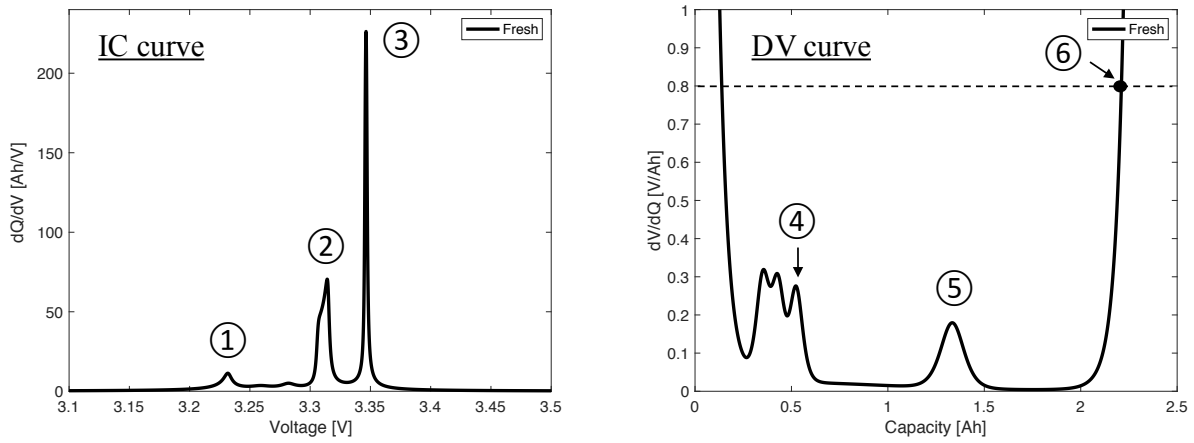
Figure 7.2: Evolution of three different data curves with increments of three different degradation modes. First column (blue) is for LAM_{PE} , second column (red) is for LAM_{NE} , third column (green) is for LLI. (a)-(c) OCV curve, (d)-(f) IC curve, (g)-(i) DV curve. Fresh cell data is outlined in thick solid line, dashed lines represent 2% increment of each degradation mode, and thin solid lines indicate data for 10% degradation for each mode.

that the proposed framework can be applied to any type of cell chemistry and degradation level as long as the electrochemical features are captured.

Physics-guided machine learning can benefit from feature extraction. The derivative of the voltage measured at a slow rate constant current produces two most common types of differential curves: incremental capacity (IC, dQ/dV) curve and differential voltage (DV, dV/dQ) curve. Despite a simple inverse relationship, there exist distinct differences between the two curves: IC curve is plotted for cell voltage, which is a direct measurement of the battery; on the other hand, DV curve is referenced to the capacity, which is an accumulative Amp-hour charge obtained by Coulomb counting. Regarding the electrochemical features, the DV curve has local peaks at phase transitions of the electrode material, whereas the peaks in the IC curve are from phase equilibria. The plateau corresponds to the coexistence of the phases or phase equilibrium, and the step

Table 7.2: Degradation simulation scenarios

Degradation modes	Degradation level (%)																
	Fresh	Single mode						Combined mode									
LAM_{PE}	0	1	0	0	...	10	0	0	1	1	0	1	...	9	9	0	9
LAM_{NE}	0	0	1	0	...	0	10	0	1	0	1	1	...	9	0	9	9
LLI	0	0	0	1	...	0	0	10	0	1	1	1	...	0	9	9	9



Feature	Description	Feature	Description	Feature	Description
F1	IC Peak ① location	F5	IC Peak ③ location	F9	DV Peak ⑤ location
F2	IC Peak ① intensity	F6	IC Peak ③ intensity	F10	DV Peak ⑤ intensity
F3	IC Peak ② location	F7	DV Peak ④ location	F11	DV Peak distance ④-⑤
F4	IC Peak ② intensity	F8	DV Peak ④ intensity	F12	DV = 0.8 ⑥ location

Figure 7.3: Defined features from the IC and DV curves. Three distinct points are chosen from each curve based on the differential analysis studies.

between the plateaus is called a phase transition. The peaks in these curves are assigned to PE, NE, or their sum by comparing the half-cell potentials to the cell. Here, 12 different features are defined from local peaks in each differential curve, as summarized in Fig. 7.3. In this particular case, the IC curve contains three distinct peaks. These peaks correspond to the phase equilibria of the negative electrode, where the graphite half-cell potential is flat. The DV curve shows three consecutive local peaks in the low capacity area where the graphite has multiple phase transitions where the stoichiometric state $x \approx 0.18$ [21]. To manifest the cell capacity fade, the location of the

point at $dV/dQ = 0.8$ [V/Ah] is chosen for a feature. Note that the characteristics of local peaks in the differential curves can be different from battery chemistry and its nominal parameters.

7.2.4 Results and Discussion

To accurately estimate the degree of each degradation mode, a thorough investigation has been made in training and testing. In the training phase, the given data set is divided into a training set and a validation set with random indexing (i.e., in total 230 data sets are randomly split at 8:2 ratio). Since data separation is randomly performed, the best NN model is selected based on the minimum validation error among 1,000 times repetition for cross-validation. Training for the NN parameters, weights and bias term, is done through the use of the Levenberg-Marquardt (LM) algorithm. The performance of the NN model is evaluated by computing estimate errors based on the given test data sets in Fig. 7.4(b) which are not included in training data. The error is defined:

$$\mathbf{e} = \begin{bmatrix} e_1 \\ e_2 \\ e_3 \end{bmatrix} = \begin{bmatrix} LAM_{PE} \\ LAM_{NE} \\ LLI \end{bmatrix}_{Est} - \begin{bmatrix} LAM_{PE} \\ LAM_{NE} \\ LLI \end{bmatrix}_{Real} \quad (7.2)$$

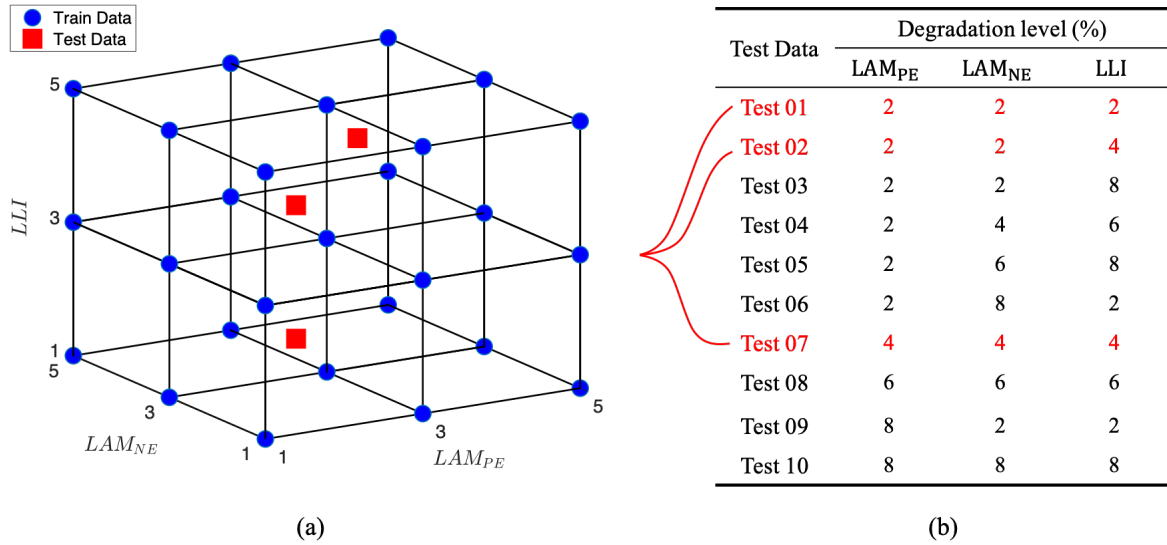


Figure 7.4: Schematic view of training and testing data sets. (a) Train and test data structure (a subset of data is selected for illustration), (b) all test data set with degradation level

Various error metrics can be used for evaluating the performance of trained model. In this study, two most common types of error metrics are used; mean absolute error (MAE) and root mean squared error (RMSE) for testing. The MAE measures the average magnitude of the errors in a set of model estimations. In the MAE, all the individual differences are weighted equally

in the average. Meanwhile, the RMSE is a square root of the averaged quadratic score where the difference between model estimation and observed values are squared during calculation. Since the errors are squared before averaged, the RMSE put a relatively high weight to large errors, hence the RMSE is more sensitive to the large errors. For this reason, the RMSE is typically considered more useful to check model performance to the outliers when large errors are particularly undesirable. The MAE and the RMSE are calculated for the test errors,

$$MAE = \frac{1}{3n} \sum_{j=1}^n \left(\sum_{i=1}^3 |e_{i,j}| \right), \quad (7.3)$$

$$RMSE = \sqrt{\frac{1}{3n} \sum_{j=1}^n \left(\sum_{i=1}^3 e_{i,j}^2 \right)}. \quad (7.4)$$

In this section, the performance of the proposed method using a NN model is presented and discussed with a focus on the network structure and the diagnostic accuracy. First, different structure of the neural network is studied to find the best model structure. Due to the nature of the NN model, as increasing the number of layers and neurons results in growing the number of NN model parameters to optimize, hence it often faces an over-fitting issue. In this study, in total 8 different candidate structures are compared to see the impact of the number of neurons and hidden layers.

Results are summarized in Table 7.3 where the NN structure is represented by a sequence of the number of neurons from the input layer to the hidden layer to the output layer. Since the dimension of input feature is 12 (the extracted feature from the IC and DV curves) and the output dimension is 3 (degree of degradation for three degradation modes), all models are composed of 12 neurons in the input layer and 3 neurons in the output layer. It can be seen that the number of network parameters increases as the model structure becomes complicated. Comparing the results from Model 2 to Model 5, the impact of increasing the number of neurons is shown that the test error decreases and after a certain number of parameters it begins to grow indicating the over-fitting problem. Model 4 shows the best performance over the given test data set in both MAE and RMSE less than 0.1.

Secondly, the diagnostic errors are evaluated for each degradation mode [LAM_{PE} , LAM_{NE} , LLI]. By comparing the errors, the empirical diagnostic accuracy of each degradation mode can be analyzed with two types of error metrics. Figure 7.5 shows that, for the considered battery chemistry, LAM_{NE} is most accurately estimated over the given test data. Investigating the input features and output degradation levels, we found that the feature F11, distance between two peaks in the DV curve, only changes with an increase in the degradation level of LAM_{NE} . Therefore, the better accuracy of LAM_{NE} can be achieved when the change in F11 is discernible, which is the considered case of an LFP/Graphite cell. It is also found that LLI is most challenging to be

Table 7.3: Parametric study for selecting the best model structure. The best result is highlighted in boldface text.

Model ID	NN Structure	Number of Parameters	Test Error (MAE)	Test Error (RMSE)
Model 1	12x3	39	0.579	0.937
Model 2	12x6x3	99	0.132	0.190
Model 3	12x8x3	131	0.063	0.106
Model 4	12x10x3	163	0.055	0.087
Model 5	12x12x3	195	0.070	0.093
Model 6	12x6x10x3	181	0.069	0.124
Model 7	12x10x6x3	217	0.073	0.106
Model 8	12x10x10x3	273	0.135	0.200

accurately estimated in the averaged test errors. In Fig. 7.5, two error metrics (MAE and RMSE) show the largest deviation for LLI mode, indicating that the individual errors are widely spread out or there exists a particularly large error compared to the other two degradation modes.

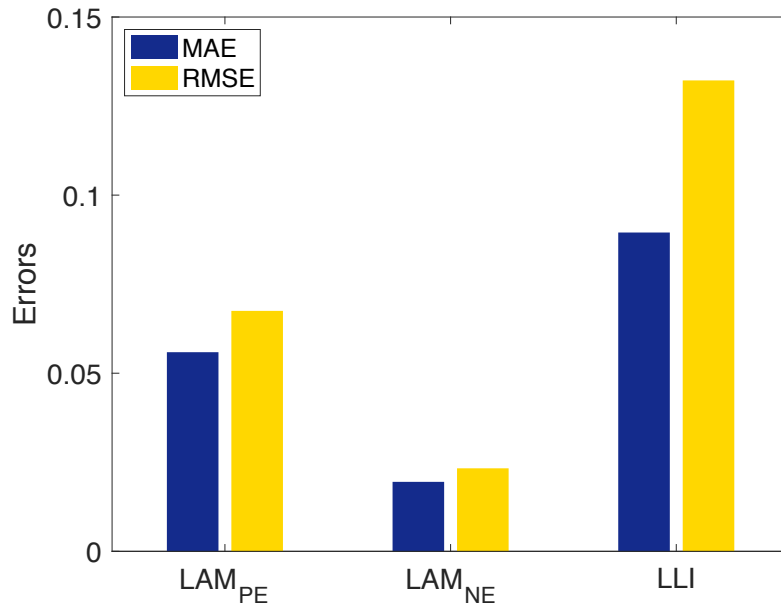


Figure 7.5: Averaged test errors (MAE and RMSE) over the test data set for three independent degradation modes.

7.2.5 Interpretable Machine Learning

As shown in Fig. 7.3, the proposed NN model is built with 12 features defined from two differential curves (i.e. IC curve and DV curve). Although individual features provide different electrochemical information, not all of the features might be useful in building a NN model. Furthermore, for machine learning algorithms, several potential issues arise when a data set is high dimensional (i.e. commonly referred to as the curse of dimensionality). First, as more input features we have, the risk of overfitting the model increases, which would result in undesirable out of sample performance. Secondly, it takes more time and computational cost to train and optimize the model with many input features. Finally, the data-driven models become more challenging to interpret the relationship between the input features and model predictions as the model complexity tends to increase with more input features.

Most machine learning algorithms are referred to as black-box models because they can be created directly from input and output data without physical knowledge of underlying phenomena or mechanisms. However, the black-box models often raise a question on how the data-driven model works. For instance, it is typically impossible for even those who build them to understand how input features are used to make such predictions. This question is an on-going research topic for interpretable machine learning in the artificial intelligence (AI) community [24]. Interpretability is the degree to which a model can be understood in human terms. Nevertheless, it is not desirable to restrict ourselves to simple models such as decision trees or linear regression that are considered interpretable due to their simplicity and thus trade model performance for interpretability. Instead, we apply methods that analyze the model after the model is trained. The partial dependence plot (PDP) is an easy-to-understand visualization of the features' impact on the predicted output from the trained model. The PDP maps the marginal effect of the selected input features and uncovers the relationship between the predicted response and the individual input features (details on the PDP can be found in [67]).

Although the PDP is one of the useful graphical tools to visualize and analyze the interaction between the predicted response and a set of input features of interest, however, the reliability of the produced plots strongly builds on the independence assumption of the input features. Furthermore, the size of the set of input feature is recommended to be small thus the input features of interest are typically selected among the most important features.

In this study, Pearson's correlation coefficient is used to check the linear dependence between the features and select a subset of uncorrelated or weakly correlated features. Note that correlation cannot capture the non-linear relationship between features; hence the goal of the correlation analysis here is not to prove the independence between features but to exclude some features showing apparent linear dependency with the correlation value close to 1 or -1 . For dependency analysis, principal component analysis (PCA) is one good option. However, the PCA makes it difficult to

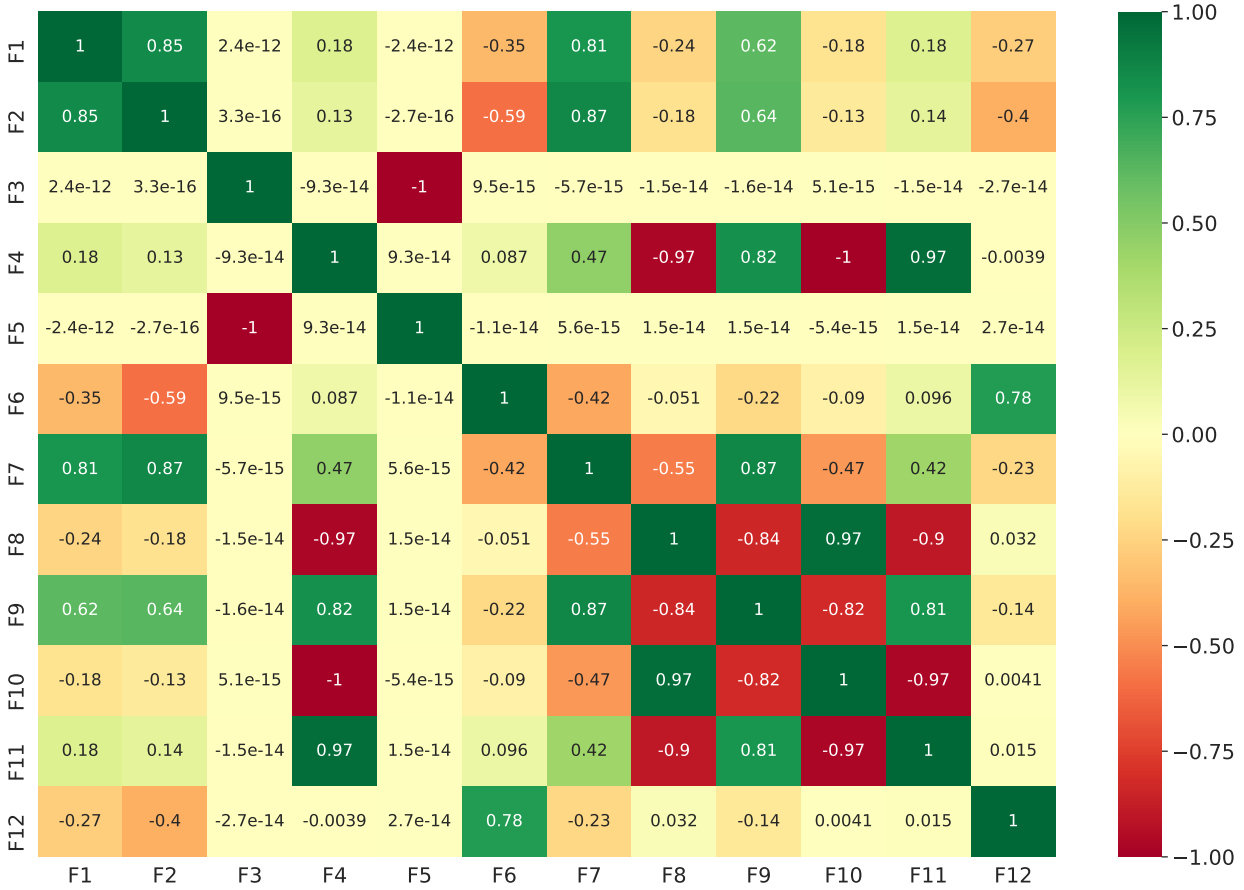


Figure 7.6: Correlation matrix for input features. The correlation coefficient value is denoted where two features are crossed. Green means positive and red means negative correlation.

interpret the given input features; therefore, it is not considered in this study.

Fig. 7.6 presents the correlation matrix as a heatmap. The correlation coefficient values are denoted where two features are crossed. Green means positive and red means negative correlation. The stronger the color, the larger the correlation magnitude, meaning that two features have a linear relationship (except the main diagonal). For instance, F4 shows strong correlations with F8 (-0.97) and F11 (0.97), which means that F4, F8, and F11 are close to linearly dependent. In which case, building a NN model with linearly dependent features can be redundant and inefficient. Moreover, dependent features violate the assumption for the PDP analysis. Therefore, we down select six features (F2, F3, F6, F9, F11, and F12) out of 12 different features defined as shown in Fig. 7.3 using this correlation matrix that has a relatively weak correlation to each other.

Fig. 7.7 shows six 1-way partial dependence plots. The target variables are the percentage degree of three degradation modes [LAM_{PE}, LAM_{NE}, LLI] as illustrated in different colors. From the PDP, the relationship between input feature and target response is clearly seen; hence we can un-

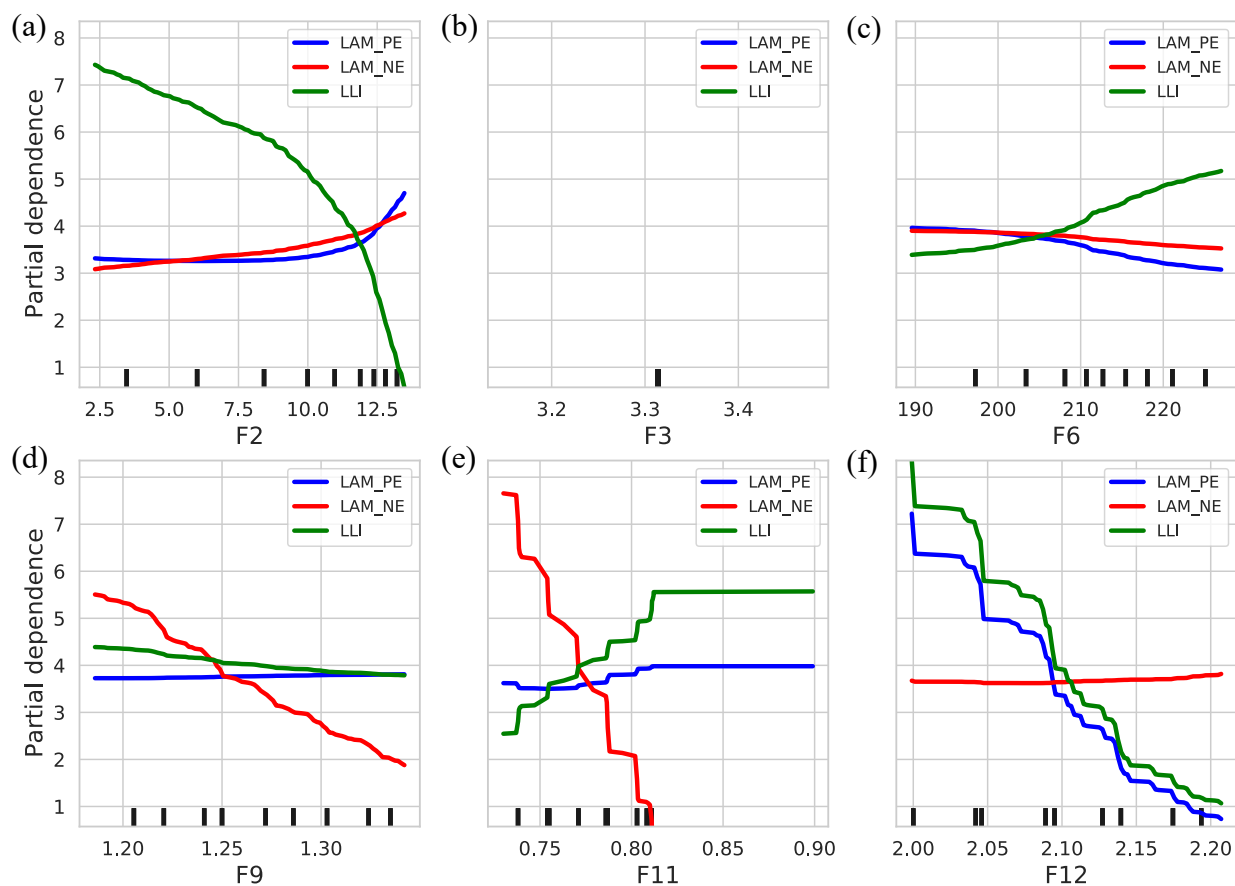


Figure 7.7: Partial dependence plots (PDP) with the selected features for three degradation modes.

Understand which feature is dominant in explaining the individual degradation mode. For instance, in Fig. 7.7(a) F2 shows a strong dependence on LLI compared to other degradation modes, indicating F2 (IC peak 1 intensity) is the main contributing feature for LLI estimation. Similarly, LAM_{NE} can be distinguished from others with F11 (DV peak distance), verifying the rationale for the empirical diagnostic accuracy results shown in Fig. 7.5. Furthermore, it is found that F3 (IC peak 2 location) does not contribute to the model performance at all, even though it is extracted from one of the peaks similarly to other features. To sum up, this PDP result can be used 1) for feature selection where the insensitive feature can be removed from the data; thus, it can reduce the effort on data collection and avoid the issue with high input feature dimension, and 2) for interpretation of the data-driven model on how the feature of interest impacts the model prediction.

7.2.6 Summary

In this case study, an electrochemical feature-based diagnostic model is proposed for estimating the level of electrode-level degradation modes (i.e. percentage degree of LAM_{PE} , LAM_{NE} , and LLI). The main contribution of this work is twofold. First, it combines the comprehensive electrochemical features extracted from both the incremental capacity (IC) curve and the differential voltage (DV) curve to enhance the diagnosis accuracy. Secondly, to the best of authors' knowledge, it is the first attempt applying a machine learning algorithm for the electrode health diagnostics, which can resolve the implementation issue of the model-based approach for onboard application. With the given specific features from both differential curves, the proposed NN model shows strong potential in identifying each degradation mode with high accuracy.

7.3 Case Study 2: Early Prediction of Battery Cycle Life

7.3.1 Background

Recent data-driven approaches have shown great potential in predicting the battery cycle life by utilizing features from various battery data. Severson et al. [95] demonstrated fairly accurate cycle life prediction (9.1% test error) with early (first 100) cycle data of the discharge voltage curve. In their study, a dataset of 124 LFP/graphite A123 cells was generated from different fast charging rates and their charging profiles. The cells were cycled between full charge and full discharge with identical nominal temperatures and discharge C-rates, but varying charge C-rates.

However, this study cautions that data-driven approaches must be combined with specific design of experiments in order to limit the range of aging conditions. In this work, we investigate the performance of the data-driven approach for battery lifetime prognostics with Li-ion batteries cycled under a variety of aging conditions, in order to determine when the data-driven approach can successfully be applied associated with electrochemical knowledge on battery degradation. We also analyze the impact of the partial data window on the prediction accuracy considering a real-world system.

7.3.2 Experimental Method and Data Generation

In this work, we construct a dataset of 12 NMC/graphite cells cycled to failure and probe the feasibility of this particular data-driven approach in Ref. [95]. To study the degradation under a variety of conditions, 12 identical 5 Ah NMC/graphite pouch cells were selected from a batch manufactured at the University of Michigan Battery Lab (UMBL). The cycle aging experiments were designed to cover an array of test conditions such as different charge/discharge C-rates, and

different operating temperatures. The test conditions, summarized in Table 7.4, range from low C-rate room temperature baseline aging to high C-rate hot temperature accelerated aging. Each of the test conditions was performed at three different temperatures: hot (45°C), cold (-5°C), and room temperature (25°C). Before the start of the cycling the cells were held at the target temperature for 3 hours to ensure thermal equilibrium.

The cycling consists of a constant current (CC) charge until reaching 4.2 V, followed by a constant voltage (CV) phase at 4.2 V until the current falls below $C/50$, and finally CC discharge until reaching 3.0 V. The dynamic tests were performed using a battery cycler (Biologic, France). The fixtures were installed inside a climate chamber (Cincinnati Ind., USA) in order to control the temperature during cycling and the characterization tests. The temperature was measured using a K-type thermocouple (Omega, USA) placed on the surface of the battery.

Throughout the cycling, intermediate diagnostic ($C/20$) tests were performed at a periodic number of cycles corresponding to an expected 5% capacity loss. For these diagnostic tests, the cells were brought back to the room temperature (25°C) and held at rest for 3 hours to ensure thermal equilibrium. The diagnostic test consists of an initial $C/5$ discharge until reaching 3.0 V, followed by a constant voltage (CV) phase at 3.0 V until the charge current falls below $C/50$ and 1 hour rest to ensure the cell is fully discharged. This is followed by a $C/20$ charge until reaching 4.2 V, then a constant voltage (CV) phase at 4.2 V until the charge current falls below $C/50$ and 1 hour rest. Finally, the cell is discharged at $C/20$ until reaching 3.0 V.

The discharge capacity curves of the 12 cells cycled to full depth-of-discharge are shown in Fig. 7.8(a). Discharge capacity is plotted as a function of Ah-throughput, rather than cycle number, because cells charged and discharged between fixed voltage limits at different temperatures and C-rates observe different Ah-throughput per cycle. Thus, the term *Ah-throughput life* is defined as the Ah-throughput at which 80% of initial capacity was reached. The wide variety of operating conditions gives rise to a wide range of Ah-throughput lives for the cells, ranging from 1000 Ah to 3000 Ah with significant capacity loss during early cycling. Fig. 7.8(c) shows that the percent capacity remaining after the first 200 Ah of throughput does correlate with Ah-throughput life, but only weakly (Pearson correlation coefficient of 0.50), indicating the difficulty of the early prediction. The correlation of the early percentage capacity loss with Ah-throughput life provides a baseline benchmark for features in the discharge voltage curve.

On average, the cells cycled at hot temperature degraded the fastest, followed by the cells cycled at cold temperature, and the cells cycled at room temperature degraded the slowest. Meanwhile, higher charge and discharge rates led to faster degradation on average. While these observations hold in an averaged sense, there are also significant outliers. For example, cell 1, cycled at low C-rate, and cell 12, cycled at room temperature, are among the fastest degrading cells. The fact that averaged trends were as expected but with significant outliers suggests that differences

in degradation rate were driven by a mix of operating variations and manufacturing variations. It should be noted that the cells used in these experiments were designed as energy cells, rather than power cells, hence the poor performance at these relatively high C-rates.

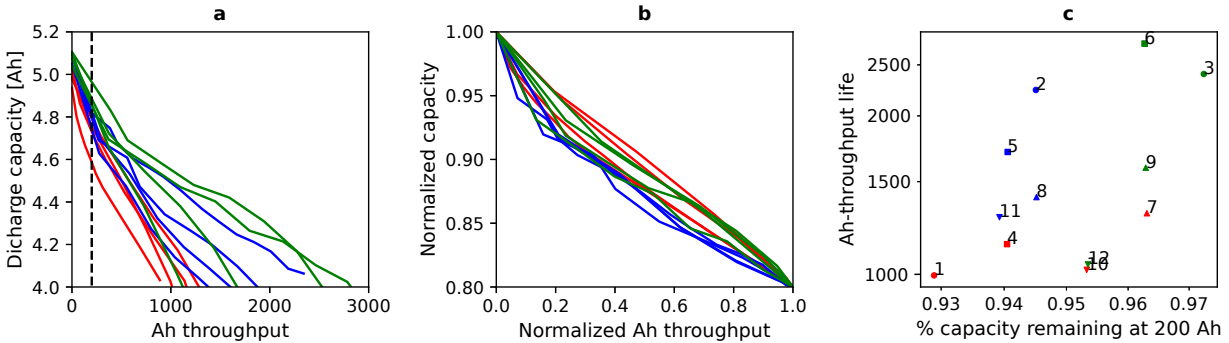


Figure 7.8: Discharge capacity curves and correlation with Ah-throughput life, indicating the difficulty of the early prediction. (a) Discharge capacities as a function of Amp-hour (Ah) throughput. The dashed black line is at 200 Ah throughput. (b) Same data, but normalized so that 80% relative capacity is reached at a normalized Ah throughput of 1, showing the relative shapes of the discharge capacity curves. (c) Correlation of percent remaining capacity after 200 Ah of throughput to Ah-throughput life. The correlation is 0.50. Colors denote temperature: hot (red), room (green), cold (blue).

7.3.3 Feature Extraction and Machine Learning Approach

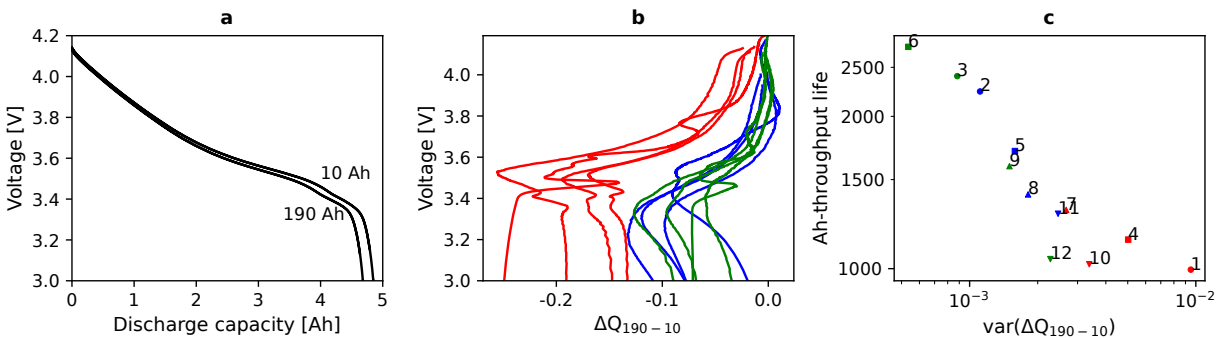


Figure 7.9: Features from the discharge voltage curves. (a) Typical discharge voltage curves after 10 Ah and 190 Ah of cycling. (b) Difference between discharge voltage curves from cycles taken after 10 Ah of cycling and 190 Ah of cycling. (c) Ah-throughput life against variance of ΔQ_{190-10} , plotted on a log-log scale. The correlation is -0.90 .

Charge and discharge voltage curves contain much more information than simply providing the capacity of the cell. Typically, state-of-health-related information is extracted from either a

charge/discharge voltage curve or its derivative with respect to discharge capacity (differential voltage analysis), on a cycle-by-cycle basis. For example, electrochemical models can be parametrized using voltage curves, or features can be directly extracted from them [8, 49]. Severson *et al.* [95] propose a new approach, comparing two discharge voltage curves from different cycles, shown here in Fig. 7.9(a). By inverting the discharge voltage curve to find the discharge capacity as a function of voltage, and then taking the difference in discharge capacities between cycles, we obtain discharge capacity difference

$$\Delta Q_{x-y}(V) = Q_x(V) - Q_y(V). \quad (7.5)$$

Here, we define Q_x to be the discharge capacity as a function of voltage for the cycle in which x Ah throughput was reached. The typical convention is to use $x > y$, so that ΔQ_{x-y} is negative, but this is not strictly necessary.

Fig. 7.9(b) shows ΔQ_{190-10} for all 12 cells, and Fig. 7.9(c) shows the variance of each of these curves plotted against Ah-throughput life on a log-log axis, with a strong negative correlation of -0.90. Other statistics of the ΔQ_{190-10} curve, such as the minimum and mean values, also show very good correlation, while the skew and kurtosis show poor correlation (see Table 7.5). This excellent correlation holds despite the wide range of operating temperatures and charge/discharge C-rates that were used not only to cycle the cells but also to obtain the ΔQ_{190-10} curve (the ΔQ_{190-10} curve is calculated directly from cycling data, rather than from separate low C-rate characterization cycles at room temperature).

To demonstrate the effectiveness of using features from the discharge voltage curve for battery lifetime prognostics, we use some of the data to train a simple machine learning algorithm, then evaluate its predictive power on a test set. Note that We restrict ourselves to simple regularized linear regressions as the small size of the dataset could easily lead to over-fitting if using more advanced algorithms. The focus of this work is to better understand the features themselves, and what are the scenarios in which they can be useful for prognostics, rather than optimization of the prognostics algorithm itself.

Based on the correlations in Table 7.5, we select the logarithms of variance, mean, and minimum of ΔQ_{190-10} as features, and the log of Ah-throughput life as the objective. Note that final errors are reported for the Ah-throughput life not in its logarithm.

We use a regularized linear regression model, the Ridge regression model. With this algorithm, we find a vector of weights \mathbf{w}^* that minimizes the cost function

$$J(\mathbf{w}) = \|\mathbf{y} - \mathbf{X}\mathbf{w}\|_2 + \alpha\|\mathbf{w}\|_2 \quad (7.6)$$

where \mathbf{y} is the vector of data and \mathbf{X} is the matrix of features. The hyperparameter α was tuned for

optimal results, to a value of 8. We choose the ridge regression model because the model only has three features, all of which are known to correlate strongly with the objective, so L1-regularizations such as LASSO regression are not necessary (L1-regularization is useful when trying to obtain sparse models where some of the weights are set to zero). We implement the ridge regression using the Python packages such as numpy, pandas, and scikit-learn.

7.3.4 Results and Discussion

For training and testing, the data is separated into training and testing sets with an 8/4 ratio. Averaging over 100 such random splits, the average training RMSE is 269 Ah (13% MPE) and the average testing RMSE is 335 Ah (16% MPE). This can be compared to the average error from a simple regression to the mean, which gives an average training RMSE of 539 Ah (29%) and an average testing RMSE of 617 Ah (35%). Therefore, using features from the discharge voltage curve approximately reduces the error of lifetime prediction in half. In Fig. 7.10, cell-by-cell predictions for a single representative train/test split are presented, which gives a training RMSE of 211 Ah (12% MPE) and a testing RMSE of 277 Ah (14% MPE). The strong correlation of the features obtained from the discharge voltage curve verifies the capability of the presented data-driven approaches even for different cell chemistry (LFP/graphite in [95] and NMC/graphite in this study), a wide range of operating temperatures, and various C-rates for charge/discharge cycling.

From this, we can see how physics can help in understanding the results in two aspects. Firstly, the strong correlation of the features obtained from the discharge voltage curve can be rationalized with the electrode-specific degradation diagnostic results from the characterization tests. In the case of these NMC/graphite cells, the degradation mechanism leading to these features is also visible in the discharge capacity curve even after 200 Ah of cycling, but using the feature from the discharge voltage curve gives superior predictive power. Using differential voltage analysis on the characterization tests, we can better understand what are the main degradation mode occurring in these cells, and hence rationalize the predictive power of the discharge voltage features. For each characterization cycle (C/20 discharges at room temperature), we use the algorithm of Mohtat *et al.* [65] to determine which form of degradation has occurred: loss of lithium inventory (LLI), or loss of active material (LAM) in the negative or positive electrode. At the same time, we calculate $\text{var}(\Delta Q)$ for that cycle by taking the difference in the discharge voltage curve with the first characterization cycle for that cell. This allows us to build a map between $\text{var}(\Delta Q)$ and LLI, LAM_n , and LAM_p , shown in Fig. 7.11. These results show that $\text{var}(\Delta Q)$ tracks LLI in exactly the same way at all C-rates and temperatures, which may be why $\text{var}(\Delta Q)$ is such a good predictor of end-of-life. Note that there may be other forms of degradation, such as SEI formation, lithium plating, or particle cracking, that also contribute to $\text{var}(\Delta Q)$ but are not captured by LLI or LAM

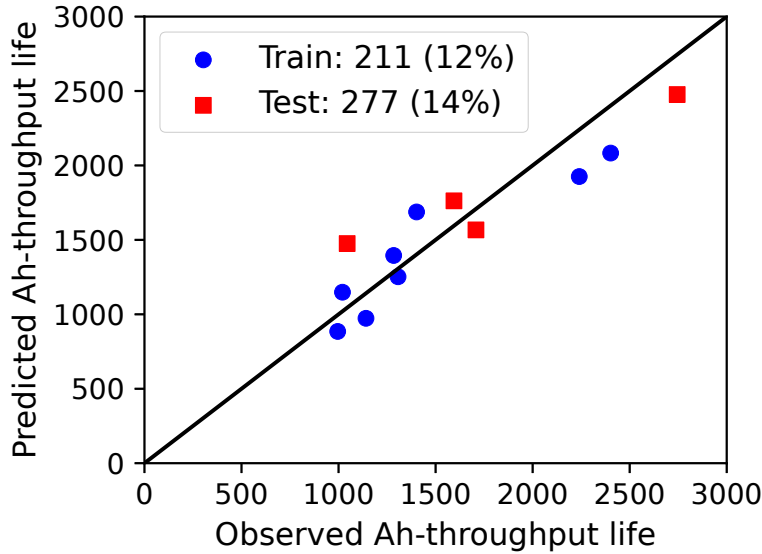


Figure 7.10: Ah-throughput life predictions using a ridge regression algorithm. The logarithms of minimum, mean, and variance of ΔQ_{190-10} are used as features. The legend shows root-mean-square error (in Ah) and mean percentage error. For comparison, a baseline prediction (from a regression to the mean) for this case gives 513 Ah training RMSE (27%) and 720 Ah testing RMSE (39%).

in the characterization cycles.

Another important finding is the impact of the partial data window on the correlation between the feature and the Ah-throughput life. In a real-life system, full discharges rarely occur, and so typically only partial discharge data is available. We investigate whether this method is still useful in this case by reducing the size of the window used for the calculation of ΔQ_{190-10} , and plotting the resulting correlation of its variance with respect to the Ah-throughput life in Fig. 7.12. There is a very rapid drop-off in the log-correlation between variance and Ah-throughput life as soon as the depth of discharge is reduced from 100% (i.e. whenever the final voltage drop-off in Fig. 7.8(a) is not captured in ΔQ). Other features (minimum, mean) in the ΔQ_{190-10} curve show similar correlation with Ah-throughput life when reducing the size of the data window. Fig. 7.12(b) shows the voltage and differential voltage (dV/dQ) for a representative cell as a function of depth of discharge. This shows that it is important to capture the final voltage drop-off, between 90 and 100% depth of discharge, to get the best correlation. Furthermore, the correlation decreases further when the cell is not discharged below the peak in dV/dQ at 40% depth of discharge. These results suggest that, for NMC/graphite cells, this data-driven approach is only useful if full discharge data is available. This effect is likely to also be significant for LFP/graphite cells used in [95], since the portion of the voltage curve that produces the ΔQ feature is only reached at around 90% depth of

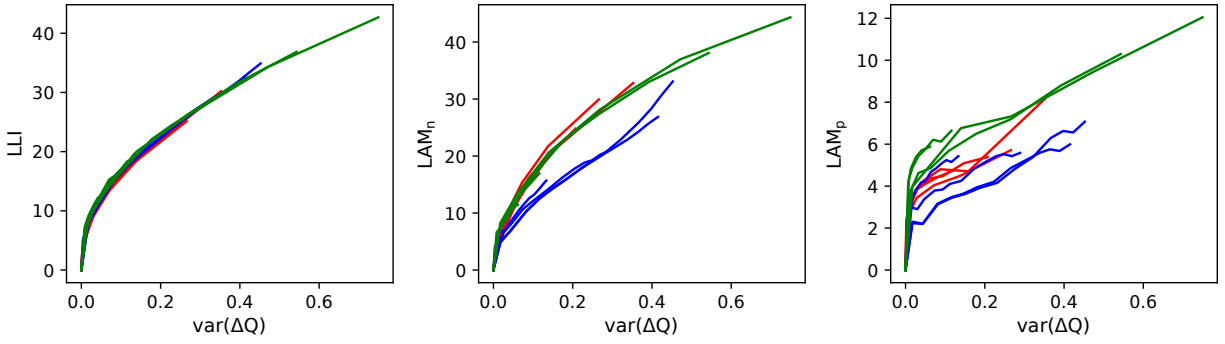


Figure 7.11: Map between the variance of (ΔQ) and the degradation modes. Degradation modes are loss of lithium inventory (LLI), loss of active material in the negative electrode (LAM_n), and loss of active material in the positive electrode (LAM_p).

discharge.

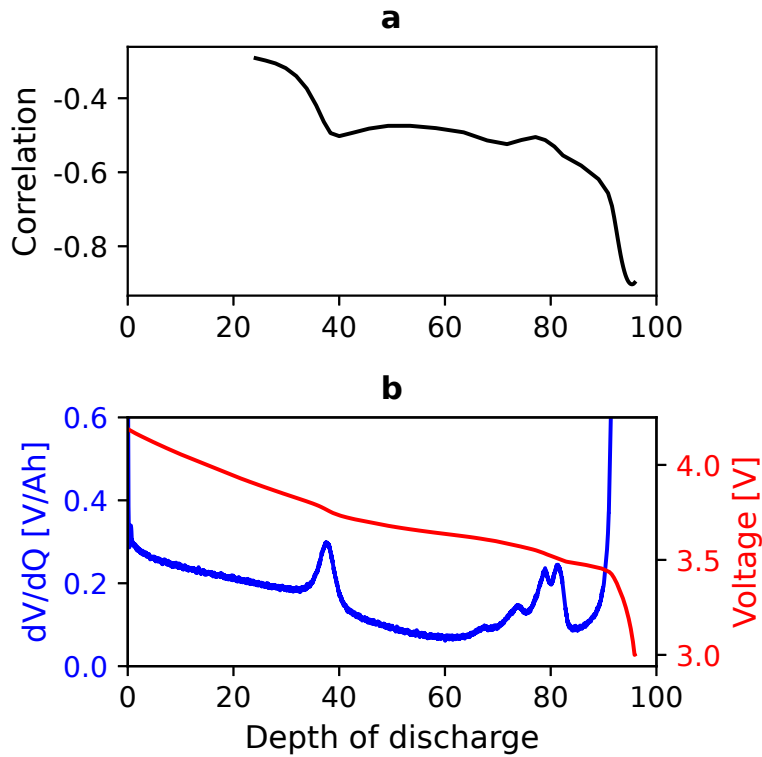


Figure 7.12: Correlation between the log of the variance of ΔQ_{190-10} and the Ah-throughput life with varying data window size. Note that varying the minimum voltage makes it available to calculate ΔQ_{190-10} . The bottom plot shows voltage, and differential voltage (dV/dQ), for reference.

7.3.5 Summary

The second case study verifies the capability of the data-driven prognostics in the early-prediction of Li-ion battery lifetime using features from the discharge capacity difference curve. This suggests that the data-driven approach is promising in the case where constant-current discharge data can be deliberately generated, even if the operating temperatures and discharge currents vary.

The strong correlation and corresponding good prediction accuracy were rationalized with the electrode-specific degradation diagnostics, which were obtained from the detailed understanding of the battery degradation. We also found that the suggested feature (the variance of discharge capacity difference) loses the strong correlation when using either partial discharge voltage data. This loss of the correlation due to the partial data window was explained by the differential voltage curve's electrochemical information.

7.4 Conclusion

In this chapter, two case studies are presented to show how the physics can guide and improve data-driven machine learning algorithms in battery degradation diagnostics and prognostics. The two case studies demonstrate the benefit of electrochemical information of the battery degradation, especially in feature selection and interpretation of the results for both diagnostic and prognostic approaches.

In the first case study, 12 different input features are extracted from local peaks in the differential voltage and incremental capacity curves, where these curves, commonly used in the electrochemical analysis, manifest the thermodynamic information of the individual electrode inside the cell. Furthermore, aged cell data for all possible combinations of different degrees of degradation modes can be generated based on physical knowledge on the electrode degradation and the OCV change without the need for executing extensive aging tests.

In the second case study, the strong correlation between the proposed feature, the variance of ΔQ_{190-10} , and the Ah-throughput life is explained with the electrode-specific degradation diagnostic results from the characterization tests. To be specific, it is found that $\text{var}(\Delta Q)$ tracks LLI for all different aging conditions (e.g. C-rate and temperature), indicating the main degradation mode for Ah-throughput life is LLI that can be extracted from the discharge capacity difference in early cycle data. Furthermore, the analysis on the impact of partial data window (i.e. when less electrochemical information is available) to the correlation shows the possible challenges in real-world applications.

Without an understanding of the underlying physics, pure data-driven approaches could face practical limitations. Combining the strengths of data-driven approaches and physics-based models

is essential to better estimate health, diagnose degradation, predict life, and detect the onset of failures. Therefore, a possible future extension from this is to develop a proper hybrid model to use for battery diagnostics and lifetime prediction that provides more accurate results with much less training data.

Table 7.4: The aging test conditions matrix. ^a The H, C, and R corresponds to hot (45°C), cold (-5°C), and room (25°C) temperature. ^b Constant current until 4.2 V and then constant voltage until ($I < C/50$).

Cyclic aging conditions													
Condition group	Test number	Temperature ^a			DOD	Charge ^b			Discharge				
		H	C	R		0-100%	0-50%	C/5	1.5C	2C	2C	C/5	1.5C
A	01, 02, 03	✓	✓	✓	✓	✓	✓	✓	✓	✓	✓	✓	✓
B	04, 05, 06	✓	✓	✓	✓	✓	✓	✓	✓	✓	✓	✓	✓
C	07, 08, 09	✓	✓	✓	✓	✓	✓	✓	✓	✓	✓	✓	✓
D	10, 11, 12	✓	✓	✓	✓	✓	✓	✓	✓	✓	✓	✓	✓

Table 7.5: Log-correlation of various statistics of the discharge difference curve, ΔQ_{190-10} , with Ah-throughput life.

Statistic	Log-correlation
Mimimum	-0.87
Mean	-0.84
Variance	-0.90
Skew	-0.18
Kurtosis	-0.24

CHAPTER 8

Conclusions and Future Work

This work presents the diagnostics for electrode-specific degradation of Li-ion batteries considering various practical aspects for real-world applications. The electrode-specific degradation diagnosis is performed by quantifying the extent of the three main degradation modes, namely Loss of Lithium Inventory (LLI), Loss of Active Material at Positive and Negative Electrodes (LAM_{PE} and LAM_{NE}) via model-based parameter identification. This work particularly focuses on practical considerations such as half-cell potential change, partial data availability, estimation accuracy, and practical charging rate.

8.1 Summary of Contributions

The contributions in this dissertation arise from the thorough understanding of the limitations in electrode-specific degradation diagnostics in real-world applications and relevant publications are summarized as follows.

1. A novel electrode state-of-health estimation method that can calibrate the aged half-cell potential function for metal oxide positive electrode was developed [54].
2. Guideline was developed for determining the desired OCV data window based on identifiability analysis and error bound of electrode state-of-health parameters [52].
3. A time-optimal current profile and computationally efficient method were developed for fast acquisition of the desired OCV data window [50].
4. An adaptive algorithm was proposed for electrode-specific degradation at a practical charging rate with analysis on peak smoothing behavior [66].
5. Possible ways of improving data-driven machine learning methods were proposed in battery degradation diagnostics and prognostics using physics-guided approaches [49, 101].

In Chapter 3, a novel method for estimating the electrode-specific state of health under the consideration of positive electrode half-cell potential change is proposed. In the proposed method, the alignment of local peaks in the differential voltage curve are used to identify the contribution of individual electrodes to the cell OCV curve and the aged positive electrode half-cell potential is calibrated. The proposed method includes experimental data to provide valid estimates of the electrode parameters.

In Chapter 4, the reliability of electrode parameter estimation accuracy is analyzed with a focus on the limited data availability for the OCV of a cell. In this work, the Cramer-Rao Bound (CRB) and confidence interval are used for quantifying the estimate's error bound of the electrode parameters at different locations and sizes of the partial data window. With the proposed method, a preferable data range is given for the required estimation accuracy.

In Chapter 5, a method to directly measure the equilibrium voltage of a battery cell is presented. The key idea is to allow bi-directional current applying (e.g. both charge and discharge pulses are available even when the battery is in charge) such that one can actively perturb a battery cell with a concatenation of charge and discharge pulses. By doing so, unlike the typical way of measuring the OCV of a cell waiting for a long relaxation period when the terminal voltage reaches a steady-state, the proposed minimum-time current profile removes the relaxation period, and thus the total data acquisition time is reduced to less than half.

In Chapter 6, the feasibility of the electrode SOH estimation is studied focusing on practical charging rates. In this work, first, the smoothing behavior of the peak in the differential voltage curve is analyzed with respect to increasing C-rate and aging state. Secondly, the estimation of the internal resistance and its impact on the electrode SOH estimation accuracy is studied. Lastly, an adaptive algorithm that enables estimating the internal resistance and electrode parameter in a real-world battery usage scenario is proposed.

In Chapter 7, two case studies are presented to show how the physics can guide and improve data-driven machine learning algorithms in battery degradation diagnostics and prognostics. The two case studies demonstrate the benefit of electrochemical information of the battery degradation, especially in feature selection and interpretation of the results for both diagnostic and prognostic approaches.

8.2 Future work

This dissertation addresses practical considerations in identifying electrode parameters associated with partial data availability, data acquisition strategy, and half-cell potential change due to aging. The proposed approach is found to be effective in providing accurate information about electrode-specific degradation modes and their diagnostics. Nevertheless, to advance the presented work, the

following can be considered as opportunities for future research.

8.2.1 Degradation diagnostics for field use cases

When it comes to battery degradation study, battery cycling and storage conditions such as current and temperature can be closely controlled in a laboratory setting. 'Ground truth' battery health, e.g., capacity and resistance, can easily be measured with regular characterization cycles as requested, and batteries can be cycled continuously until failure, which is often specified as the point where measured capacity reaches 80% of the pristine cell capacity. Lab tests are useful to find out how different operating conditions affect cycle life, and hence determine warranties and plan maintenance schedules.

However, unlike the lab-based testing, field-use cases have several critical challenges. Firstly, unlike the lab-based test, operating conditions can vary throughout a cell's life in the real world. For instance, electric vehicle batteries undergo seasonal variations in ambient temperature, geographical differences, varying SOC windows depending on drivers. This uncertainty also applies to future operating conditions, so any predictions about the future must take into account the wide range of operating conditions possible. Secondly, the data from the field use cases is difficult to be used for degradation diagnostics for several reasons. Typical industrial sensors have less accuracy than the lab test equipment and sensors. During operation, there are numerous disturbance sources including measurement noise, input bias and noise, and so on. Most of all, smaller coverage of the available data range and rapidly varying currents make it very challenging to extract features or fit parameters.

A possible extension from this work includes constructing degradation data from a variety of usage scenarios. Indeed, the availability of data on long-term aging tests of Li-ion batteries is still a challenge in developing and validating the diagnosis of battery degradation. If we could use field data to supplement or replace lab tests, this would significantly increase the amount of data available, accelerating our understanding of battery performance. Furthermore, the robustness and accuracy of the algorithm can be investigated under more field use cases.

8.2.2 Second-life batteries via advanced battery degradation diagnostics

When a battery pack cannot provide a required capacity or power for its primary use, retired Li-ion batteries can be re-purposed into a different second-life application. It is reported that these second-life batteries are both environmentally beneficial and economically viable. Especially, with the explosive growth of electric vehicle markets, end-of-life batteries from the primary application can then be reassembled into a second-life battery pack for applications such as grid or stationary energy storage systems.

In terms of long-term battery degradation, cell-to-cell variability is the main challenge to build a second-life battery pack. This variability has two sources: 1) extrinsic and 2) intrinsic. One of the most common extrinsic factors is operating conditions. Battery degradation is subject to their operating conditions, including temperature, charge/discharge current rate, depth of discharge, mechanical pressure, and so on. For instance, despite the battery cooling system, there is a temperature gradient inside a battery pack resulting in non-uniform degradation between cells. Intrinsic factors mostly originate from manufacturing variability in electrode materials, manufacturing processes, formation conditions, etc.

Since two batteries can have similar capacity but different internal health states, detailed Li-ion battery SOH information is essential to build a robust and reliable second-life battery pack. With comprehensive diagnostic information, retired Li-ion batteries can be evaluated rigorously and re-assembled into second-life applications. When building a re-purposed battery pack, multiple aged cells can be optimally selected depending on their degradation status and the use of applications.

8.2.3 Physics-guided machine learning in battery lifetime prediction

Depending on their applications, Li-ion batteries undergo different usage patterns and environmental conditions, making the degradation of batteries different. A critical challenge is to achieve accurate predictions of a lifetime under various operating conditions in use. Improvements in remaining life prediction can bring a more beneficial warranty design, cost-effective predictive maintenance, improved prospects for second-life applications, and ultimately better control and management of the battery systems that could prolong their life.

Two distinct approaches exist to address the challenge of lifetime prediction: data-driven methods and physics-based models. Data-driven methods try to find a correlation between the given input and output data, not necessarily relying on the underlying physics. Due to its nature, data-driven models require a lot of training data, which is not always available. Alternatively, in the physics-based approach, models are constructed from first-principles, and they are tuned with parameter identification through data fitting. It uses relatively less experimental data than the data-driven methods, but a specific experimental design is often required.

Unfortunately, neither of these approaches alone can solve the challenge of battery lifetime prognostics. The data-driven approach suffers from the *curse of dimensionality*, where the amount of data needed to capture all combinations of operating conditions grows exponentially. A hybrid approach can be used to combine the flexibility of the data-driven approach with the accurate physics-based approach. The specific form of the hybrid model to use for lifetime prediction is yet to be determined. One promising approach is physics-guided machine learning. For instance, one could use electrochemical knowledge on battery degradation to identify useful features in the

data to use as input to data-driven machine learning algorithms instead of raw data. Alternatively, data-driven models can be used to improve the physics-based models by filling the gap between the physics-based model prediction and actual measurement with the data-driven techniques.

APPENDIX A

Optimal Control Theories

A.1 State Constraints In Optimal Control Problem

The state constraint $\Omega_x(t) \subset \mathbb{R}^n$ is defined by the scalar inequality function $G(x, t) \leq 0$. The function $G(x, t)$ is assumed to be continuously differentiable. In the formulation of the modified Hamiltonian, it is assumed that the state constraint $x^*(t) \in \Omega_x(t)$ is active in a subinterval $[t_1, t_2]$ of $[t_0, t_f]$ and inactive for $t_0 \leq t < t_1$ and $t_2 < t \leq t_f$. Then, the constraint function $G(x, t)$ is taken for consecutive derivatives with respect to time until the control u appears explicitly for the first time in $G^{(j)}$:

$$\begin{aligned}
 G^{(0)}(x, t) &= G(x, t) \\
 G^{(1)}(x, t) &= \frac{d}{dt}G(x, t) = \frac{\partial G(x, t)}{\partial x}x\dot{(t)} + \frac{\partial G(x, t)}{\partial t} \\
 &\vdots \\
 G^{(j-1)}(x, t) &= \frac{d}{dt}G^{(j-2)}(x, t) \\
 G^{(j)}(x, u, t) &= \frac{d}{dt}G^{(j-1)}(x, t).
 \end{aligned} \tag{A.1}$$

Then, the following modifications are satisfied for the optimal control u^* when the state constraint is active in the time interval $t \in [t_1, t_2]$. The Hamiltonian and co-states are augmented by the active state constraint with additional Lagrange multiplier μ where $\mu^* \geq 0$,

$$\begin{aligned}
 \bar{H} &= H(x^*, u, \lambda^*, t) + \mu^* G^{(j)}(x^*, u, t), \\
 \dot{\lambda}^*(t) &= -\bar{H}_x \\
 &= -H_x - \mu^* G_x^{(j)}, \\
 G^{(j)}(x^*, t) &= 0.
 \end{aligned} \tag{A.2}$$

where \bar{H} is the augmented Hamiltonian function and satisfies the optimality condition

$$\begin{aligned} H(x^*, u^*, \lambda^*, t) + \mu^* G^{(j)}(x^*, u^*, t) &\leq \\ H(x^*, u, \lambda^*, t) + \mu^* G^{(j)}(x^*, u, t). \end{aligned}$$

A.2 Number of Switching Point

For a linear time-optimal control, we can analyze the general form of the switching function $\phi(t)$ using Hamiltonian \mathcal{H} ,

$$\begin{aligned} \dot{\lambda}(t) &= -A^T \lambda(t), \\ \lambda(t) &= \lambda(t_0) e^{-A^T(t-t_0)}, \\ \phi(t) &= \lambda^T(t) B = \lambda(t_0) e^{-A^T(t-t_0)} B. \end{aligned} \tag{A.3}$$

In the case when all eigenvalues of A are real, $\phi(t)$ is given as a sum of exponential functions,

$$\phi(t) = \gamma_1(t) e^{\alpha_1 t} + \dots + \gamma_k(t) e^{\alpha_k t}, \tag{A.4}$$

where $\gamma_i(t)$ are polynomials with degree at most $q_i - 1$ where q_i is the multiplicity of α_i and α_i are real.

Define

$$\deg \phi(t) = \sum_{i=1}^k (1 + \deg \gamma_i). \tag{A.5}$$

Then $\phi(t)$ can have at most $(\deg \phi - 1)$ zeros. The proof of this claim is by induction. If $\deg \phi = 1$ then ϕ is of the form, $\phi(t) = ce^{\alpha_1 t}$, $c \neq 0$, and does not have zeros. Suppose the claim has been proved for all functions with $\deg \phi = r - 1$ and consider ϕ with $\deg \phi = r$. Let $\xi(t) = \phi(t) e^{-\alpha_1 t} = \gamma_1(t) + \sum_{i=2}^k \gamma_i(t) e^{(\alpha_i - \alpha_1)t}$. Since $\deg \gamma_1(t)$ is one less than $\deg \phi(t)$, it follows by induction hypothesis that $\dot{\xi}(t)$ has at most $r - 1$ zeros. By mean value theorem, $\xi(b) - \xi(a) = \dot{\xi}(c)(b - a)$, and between any two zeros of function, ξ , there must be a zero of its derivative; hence, $\dot{\xi}$ and, therefore, ϕ can at most r zeros [105].

BIBLIOGRAPHY

- [1] K Amine, J Liu, and I Belharouak. High-temperature storage and cycling of c-lifepo4/graphite li-ion cells. *Electrochemistry communications*, 7(7):669–673, 2005.
- [2] D Andre, M Meiler, K Steiner, Ch Wimmer, T Soczka-Guth, and DU Sauer. Characterization of high-power lithium-ion batteries by electrochemical impedance spectroscopy. i. experimental investigation. *Journal of Power Sources*, 196(12):5334–5341, 2011.
- [3] David Anseán, Víctor Manuel García, Manuela González, Cecilio Blanco-Viejo, Juan Carlos Viera, Yoana Fernández Pulido, and Luciano Sánchez. Lithium-ion battery degradation indicators via incremental capacity analysis. *IEEE Transactions on Industry Applications*, 55(3):2992–3002, 2019.
- [4] Harvey Thomas Banks, Stacey L Ernstberger, and Sarah L Grove. Standard errors and confidence intervals in inverse problems: sensitivity and associated pitfalls. *Journal of Inverse and Ill-posed Problems jiiip*, 15(1):1–18, 2007.
- [5] Federico Baronti, Walter Zamboni, Roberto Roncella, Roberto Saletti, and Giovanni Spagnuolo. Open-circuit voltage measurement of lithium-iron-phosphate batteries. In *Instrumentation and Measurement Technology Conference (I2MTC), 2015 IEEE International*, pages 1711–1716. IEEE, 2015.
- [6] Dimitri P Bertsekas, Dimitri P Bertsekas, Dimitri P Bertsekas, and Dimitri P Bertsekas. *Dynamic programming and optimal control*, volume 1. Athena scientific Belmont, MA, 1995.
- [7] Christoph R Birkl, Euan McTurk, Stefanie Zekoll, Felix H Richter, Matthew R Roberts, Peter G Bruce, and David A Howey. Degradation diagnostics for commercial lithium-ion cells tested at- 10° c. *Journal of The Electrochemical Society*, 164(12):A2644–A2653, 2017.
- [8] Christoph R Birkl, Matthew R Roberts, Euan McTurk, Peter G Bruce, and David A Howey. Degradation diagnostics for lithium ion cells. *Journal of Power Sources*, 341:373–386, 2017.
- [9] CR Birkl, E McTurk, MR Roberts, PG Bruce, and DA Howey. A parametric open circuit voltage model for lithium ion batteries. *Journal of The Electrochemical Society*, 162(12):A2271–A2280, 2015.

- [10] Ira Bloom, Jon P Christophersen, Daniel P Abraham, and Kevin L Gering. Differential voltage analyses of high-power lithium-ion cells: 3. another anode phenomenon. *Journal of power sources*, 157(1):537–542, 2006.
- [11] Ira Bloom, Andrew N Jansen, Daniel P Abraham, Jamie Knuth, Scott A Jones, Vincent S Battaglia, and Gary L Henriksen. Differential voltage analyses of high-power, lithium-ion cells: 1. technique and application. *Journal of Power Sources*, 139(1-2):295–303, 2005.
- [12] John Cannarella and Craig B Arnold. Stress evolution and capacity fade in constrained lithium-ion pouch cells. *Journal of Power Sources*, 245:745–751, 2014.
- [13] Lluç Canals Casals, B Amante García, and Camille Canal. Second life batteries lifespan: Rest of useful life and environmental analysis. *Journal of environmental management*, 232:354–363, 2019.
- [14] Rajeswari Chandrasekaran. Quantification of bottlenecks to fast charging of lithium-ion-insertion cells for electric vehicles. *Journal of Power Sources*, 271:622–632, 2014.
- [15] Zheng Chen, Chunting Chris Mi, Yuhong Fu, Jun Xu, and Xianzhi Gong. Online battery state of health estimation based on genetic algorithm for electric and hybrid vehicle applications. *Journal of Power Sources*, 240:184–192, 2013.
- [16] W Choi and A Manthiram. Comparison of metal ion dissolutions from lithium ion battery cathodes. *Journal of The Electrochemical Society*, 153(9):A1760–A1764, 2006.
- [17] Jon P Christophersen, Gary L Hunt, Chinh D Ho, and David Howell. Pulse resistance effects due to charging or discharging of high-power lithium-ion cells: A path dependence study. *Journal of Power Sources*, 173(2):998–1005, 2007.
- [18] Ariel Cintrón-Arias, Harvey Thomas Banks, Alex Capaldi, and Alun L Lloyd. A sensitivity matrix based methodology for inverse problem formulation. *Journal of Inverse and Ill-posed Problems*, 17(6):545–564, 2009.
- [19] ClipperCreek. *Estimated Charge Times Chart*, (accessed: 11.30.2020). <https://energywisemnstore.com/content/Time-to-Charge-Chart-Clipper-Creek.pdf>.
- [20] Andrea Cordoba-Arenas, Simona Onori, Yann Guezennec, and Giorgio Rizzoni. Capacity and power fade cycle-life model for plug-in hybrid electric vehicle lithium-ion battery cells containing blended spinel and layered-oxide positive electrodes. *Journal of Power Sources*, 278:473–483, 2015.
- [21] JR Dahn. Phase diagram of Li_xC_6 . *Physical Review B*, 44(17):9170, 1991.
- [22] Christopher L Darby, William W Hager, and Anil V Rao. An hp-adaptive pseudospectral method for solving optimal control problems. *Optimal Control Applications and Methods*, 32(4):476–502, 2011.

- [23] Trung K Dong, Angel Kirchev, Florence Mattera, and Yann Bultel. Modeling of lithium iron phosphate batteries by an equivalent electrical circuit: Method of model parameterization and simulation. *ECS Transactions*, 25(35):131–138, 2010.
- [24] Mengnan Du, Ninghao Liu, and Xia Hu. Techniques for interpretable machine learning. *Communications of the ACM*, 63(1):68–77, 2019.
- [25] Matthieu Dubarry, M Bercibar, A Devie, D Anseán, N Omar, and I Villarreal. State of health battery estimator enabling degradation diagnosis: Model and algorithm description. *Journal of Power Sources*, 360:59–69, 2017.
- [26] Matthieu Dubarry, Cyril Truchot, and Bor Yann Liaw. Synthesize battery degradation modes via a diagnostic and prognostic model. *Journal of power sources*, 219:204–216, 2012.
- [27] Joel C Forman, Saeid Bashash, Jeffrey L Stein, and Hosam K Fathy. Reduction of an electrochemistry-based li-ion battery model via quasi-linearization and pade approximation. *Journal of the Electrochemical Society*, 158(2):A93–A101, 2011.
- [28] Joel C Forman, Scott J Moura, Jeffrey L Stein, and Hosam K Fathy. Genetic identification and fisher identifiability analysis of the doyle–fuller–newman model from experimental cycling of a lifepo4 cell. *Journal of Power Sources*, 210:263–275, 2012.
- [29] Rujian Fu, Meng Xiao, and Song-Yul Choe. Modeling, validation and analysis of mechanical stress generation and dimension changes of a pouch type high power li-ion battery. *Journal of Power Sources*, 224:211–224, 2013.
- [30] Thomas F Fuller, Marc Doyle, and John Newman. Simulation and optimization of the dual lithium ion insertion cell. *Journal of the Electrochemical Society*, 141(1):1–10, 1994.
- [31] Divya Garg, William W Hager, and Anil V Rao. Pseudospectral methods for solving infinite-horizon optimal control problems. *Automatica*, 47(4):829–837, 2011.
- [32] Hans P Geering. *Optimal control with engineering applications*. Springer, 2007.
- [33] James A Gilbert, Javier Bareño, Timothy Spila, Stephen E Trask, Dean J Miller, Bryant J Polzin, Andrew N Jansen, and Daniel P Abraham. Cycling behavior of ncm523/graphite lithium-ion cells in the 3–4.4 v range: diagnostic studies of full cells and harvested electrodes. *Journal of The Electrochemical Society*, 164(1):A6054–A6065, 2017.
- [34] Sébastien Grolleau, Arnaud Delaille, Hamid Gualous, Philippe Gyan, Renaud Revel, Julien Bernard, Eduardo Redondo-Iglesias, Jérémy Peter, and SIMCAL Network. Calendar aging of commercial graphite/lifepo4 cell—predicting capacity fade under time dependent storage conditions. *Journal of Power Sources*, 255:450–458, 2014.
- [35] Anupama Guduru, Paul WC Northrop, Shruti Jain, Andrew C Crothers, Timothy R Marchant, and Venkat R Subramanian. Analytical solution for electrolyte concentration distribution in lithium-ion batteries. *Journal of Applied Electrochemistry*, 42(4):189–199, 2012.

- [36] Arijit Guha and Amit Patra. State of health estimation of lithium-ion batteries using capacity fade and internal resistance growth models. *IEEE Transactions on Transportation Electrification*, 4(1):135–146, 2017.
- [37] Xuebing Han, Minggao Ouyang, Languang Lu, Jianqiu Li, Yuejiu Zheng, and Zhe Li. A comparative study of commercial lithium ion battery cycle life in electrical vehicle: Aging mechanism identification. *Journal of Power Sources*, 251:38–54, 2014.
- [38] Hongwen He, Rui Xiong, and Jinxin Fan. Evaluation of lithium-ion battery equivalent circuit models for state of charge estimation by an experimental approach. *energies*, 4(4):582–598, 2011.
- [39] Yan-Bing He, Feng Ning, Quan-Hong Yang, Quan-Sheng Song, Baohua Li, Fangyuan Su, Hongda Du, Zhi-Yuan Tang, and Feiyu Kang. Structural and thermal stabilities of layered $\text{Li}(\text{Ni}_{1/3}\text{Co}_{1/3}\text{Mn}_{1/3})\text{O}_2$ materials in 18650 high power batteries. *Journal of Power Sources*, 196(23):10322–10327, 2011.
- [40] Kohei Honkura, Hidetoshi Honbo, Yoshimasa Koishikawa, and Tatsuo Horiba. State analysis of lithium-ion batteries using discharge curves. *ECS Transactions*, 13(19):61–73, 2008.
- [41] Chao Hu, Byeng D Youn, and Jaesik Chung. A multiscale framework with extended kalman filter for lithium-ion battery soc and capacity estimation. *Applied Energy*, 92:694–704, 2012.
- [42] Xiaosong Hu, Shengbo Li, and Huei Peng. A comparative study of equivalent circuit models for li-ion batteries. *Journal of Power Sources*, 198:359–367, 2012.
- [43] Ala A Hussein. Capacity fade estimation in electric vehicle li-ion batteries using artificial neural networks. *IEEE Transactions on Industry Applications*, 51(3):2321–2330, 2014.
- [44] J Jaguemont, L Boulon, and Y Dubé. A comprehensive review of lithium-ion batteries used in hybrid and electric vehicles at cold temperatures. *Applied Energy*, 164:99–114, 2016.
- [45] K Jalkanen, J Karppinen, L Skogström, T Laurila, M Nisula, and K Vuorilehto. Cycle aging of commercial nmc/graphite pouch cells at different temperatures. *Applied energy*, 154:160–172, 2015.
- [46] Christian Julien, Alain Mauger, Karim Zaghbi, and Henri Groult. Comparative issues of cathode materials for li-ion batteries. *Inorganics*, 2(1):132–154, 2014.
- [47] Deepak K Karthikeyan, Godfrey Sikha, and Ralph E White. Thermodynamic model development for lithium intercalation electrodes. *Journal of Power Sources*, 185(2):1398–1407, 2008.
- [48] IL-Song Kim. A technique for estimating the state of health of lithium batteries through a dual-sliding-mode observer. *IEEE Transactions on Power Electronics*, 25(4):1013–1022, 2009.

- [49] Suhak Lee and Youngki Kim. Li-ion battery electrode health diagnostics using machine learning. In *2020 American Control Conference (ACC)*, pages 1137–1142. IEEE, 2020.
- [50] Suhak Lee, Youngki Kim, Jason B Siegel, and Anna G Stefanopoulou. Minimum-time measurement of open circuit voltage of battery systems. In *2019 American Control Conference (ACC)*, pages 884–889. IEEE, 2019.
- [51] Suhak Lee, Peyman Mohtat, Jason B Siegel, and Anna G Stefanopoulou. Beyond estimating battery state of health: identifiability of individual electrode capacity and utilization. In *2018 Annual American Control Conference (ACC)*, pages 2288–2293. IEEE, 2018.
- [52] Suhak Lee, Peyman Mohtat, Jason B Siegel, Anna G Stefanopoulou, Jang-Woo Lee, and Tae-Kyung Lee. Estimation error bound of battery electrode parameters with limited data window. *IEEE Transactions on Industrial Informatics*, 16(5):3376–3386, 2019.
- [53] Suhak Lee, Jason B Siegel, Anna G Stefanopoulou, Jang-Woo Lee, and Tae-Kyung Lee. Comparison of individual-electrode state of health estimation methods for lithium ion battery. In *ASME 2018 Dynamic Systems and Control Conference*. American Society of Mechanical Engineers Digital Collection, 2018.
- [54] Suhak Lee, Jason B Siegel, Anna G Stefanopoulou, Jang-Woo Lee, and Tae-Kyung Lee. Electrode state of health estimation for lithium ion batteries considering half-cell potential change due to aging. *Journal of The Electrochemical Society*, 167(9):090531, 2020.
- [55] An Li, Serge Pelissier, Pascal Venet, and Philippe Gyan. Fast characterization method for modeling battery relaxation voltage. *Batteries*, 2(2):7, 2016.
- [56] Yi Li, Kailong Liu, Aoife M Foley, Alana Zülke, Maitane Berecibar, Elise Nanini-Maury, Joeri Van Mierlo, and Harry E Hoster. Data-driven health estimation and lifetime prediction of lithium-ion batteries: A review. *Renewable and Sustainable Energy Reviews*, 113:109254, 2019.
- [57] Bor Yann Liaw, Ganesan Nagasubramanian, Rudolph G Jungst, and Daniel H Doughty. Modeling of lithium ion cells—a simple equivalent-circuit model approach. *Solid state ionics*, 175(1-4):835–839, 2004.
- [58] Chris Lilly. *EV charging guides*, (accessed: 11.30.2020). <https://www.zap-map.com/charge-points/ev-charging-guides/>.
- [59] Xinfan Lin. Analytic analysis of the data-dependent estimation accuracy of battery equivalent circuit dynamics. *IEEE Control Systems Letters*, 1(2):304–309, 2017.
- [60] Xinfan Lin. A data selection strategy for real-time estimation of battery parameters. In *2018 Annual American Control Conference (ACC)*, pages 2276–2281. IEEE, 2018.
- [61] Xinfan Lin and Anna G Stefanopoulou. Analytic bound on accuracy of battery state and parameter estimation. *Journal of The Electrochemical Society*, 162(9):A1879, 2015.

- [62] Ping Liu, John Wang, Jocelyn Hicks-Garner, Elena Sherman, Souren Soukiazian, Mark Verbrugge, Harshad Tataria, James Musser, and Peter Finamore. Aging mechanisms of lifepo4 batteries deduced by electrochemical and structural analyses. *Journal of the Electrochemical Society*, 157(4):A499–A507, 2010.
- [63] Hans E. Melin. The lithium-ion battery end-of-life market—a baseline study. In *World Economic Forum: Cologny, Switzerland*, pages 1–11, 2018.
- [64] Shankar Mohan, Youngki Kim, and Anna G Stefanopoulou. Estimating the power capability of li-ion batteries using informationally partitioned estimators. *IEEE Transactions on Control Systems Technology*, 24(5):1643–1654, 2015.
- [65] Peyman Mohtat, Suhak Lee, Jason B Siegel, and Anna G Stefanopoulou. Towards better estimability of electrode-specific state of health: Decoding the cell expansion. *Journal of Power Sources*, 427:101–111, 2019.
- [66] Peyman Mohtat, Suhak Lee, Valentin Sulzer, Jason B Siegel, and Anna G Stefanopoulou. Differential expansion and voltage model for li-ion batteries at practical charging rates. *Journal of The Electrochemical Society*, 167(11):110561, 2020.
- [67] Christoph Molnar. *Interpretable machine learning*. Lulu. com, 2020.
- [68] Scott J Moura. Estimation and control of battery electrochemistry models: A tutorial. In *2015 54th IEEE Conference on Decision and Control (CDC)*, pages 3906–3912. IEEE, 2015.
- [69] Dipak Munshi and Martin Kilbinger. Principal component analysis of weak lensing surveys. *Astronomy & Astrophysics*, 452(1):63–73, 2006.
- [70] Gang Ning and Branko N Popov. Cycle life modeling of lithium-ion batteries. *Journal of The Electrochemical Society*, 151(10):A1584–A1591, 2004.
- [71] Ki-Yong Oh, Jason B Siegel, Lynn Secondo, Sun Ung Kim, Nassim A Samad, Jiawei Qin, Dyché Anderson, Krishna Garikipati, Aaron Knobloch, Bogdan I Epureanu, et al. Rate dependence of swelling in lithium-ion cells. *Journal of Power Sources*, 267:197–202, 2014.
- [72] Saehong Park, Dylan Kato, Zach Gima, Reinhardt Klein, and Scott Moura. Optimal experimental design for parameterization of an electrochemical lithium-ion battery model. *Journal of The Electrochemical Society*, 165(7):A1309, 2018.
- [73] C Pastor-Fernández, T Bruen, WD Widanage, MA Gama-Valdez, and J Marco. A study of cell-to-cell interactions and degradation in parallel strings: implications for the battery management system. *Journal of Power Sources*, 329:574–585, 2016.
- [74] Michael A Patterson and Anil V Rao. Gpops-ii: A matlab software for solving multiple-phase optimal control problems using hp-adaptive gaussian quadrature collocation methods and sparse nonlinear programming. *ACM Transactions on Mathematical Software (TOMS)*, 41(1):1, 2014.

- [75] Christina Peabody and Craig B Arnold. The role of mechanically induced separator creep in lithium-ion battery capacity fade. *Journal of Power Sources*, 196(19):8147–8153, 2011.
- [76] Hector E Perez, Jason B Siegel, Xinfan Lin, Anna G Stefanopoulou, Yi Ding, and Matthew P Castanier. Parameterization and validation of an integrated electro-thermal cylindrical lfp battery model. In *ASME 2012 5th Annual Dynamic Systems and Control Conference joint with the JSME 2012 11th Motion and Vibration Conference*, pages 41–50. American Society of Mechanical Engineers, 2012.
- [77] Martin Petit, Eric Prada, and Valérie Sauvart-Moynot. Development of an empirical aging model for li-ion batteries and application to assess the impact of vehicle-to-grid strategies on battery lifetime. *Applied energy*, 172:398–407, 2016.
- [78] Mathias Petzl and Michael A Danzer. Advancements in ocv measurement and analysis for lithium-ion batteries. *IEEE Transactions on energy conversion*, 28(3):675–681, 2013.
- [79] Gregory L Plett. *Battery management systems, Volume I: Battery modeling*, volume 1. Artech House, 2015.
- [80] Githin K Prasad and Christopher D Rahn. Model based identification of aging parameters in lithium ion batteries. *Journal of power sources*, 232:79–85, 2013.
- [81] Kun Qian, Yiyang Li, Yan-Bing He, Dongqing Liu, Yong Zheng, Dan Luo, Baohua Li, and Feiyu Kang. Abuse tolerance behavior of layered oxide-based li-ion battery during overcharge and over-discharge. *RSC advances*, 6(80):76897–76904, 2016.
- [82] Saeed Khaleghi Rahimian, Sean Rayman, and Ralph E White. Extension of physics-based single particle model for higher charge–discharge rates. *Journal of Power Sources*, 224:180–194, 2013.
- [83] M Rehme, S Richter, A Temmler, and U Götze. Second-life battery applications-market potentials and contribution to the cost effectiveness of electric vehicles. In *5th Conference on Future Automotive Technology (CoFAT). Munich (May 2009)*. doi, volume 10, 2016.
- [84] Jürgen Remmlinger, Michael Buchholz, Markus Meiler, Peter Bernreuter, and Klaus Dietmayer. State-of-health monitoring of lithium-ion batteries in electric vehicles by on-board internal resistance estimation. *Journal of Power Sources*, 196(12):5357–5363, 2011.
- [85] Jorn M Reniers, Grietus Mulder, and David A Howey. Review and performance comparison of mechanical-chemical degradation models for lithium-ion batteries. *Journal of The Electrochemical Society*, 166(14):A3189–A3200, 2019.
- [86] Seyed Mohammad Rezvanizani, Zongchang Liu, Yan Chen, and Jay Lee. Review and recent advances in battery health monitoring and prognostics technologies for electric vehicle (ev) safety and mobility. *Journal of Power Sources*, 256:110–124, 2014.
- [87] Michael A Roscher and Dirk Uwe Sauer. Dynamic electric behavior and open-circuit-voltage modeling of lifepo4-based lithium ion secondary batteries. *Journal of Power Sources*, 196(1):331–336, 2011.

- [88] M Safari and C Delacourt. Modeling of a commercial graphite/lifepo4 cell. *Journal of The Electrochemical Society*, 158(5):A562–A571, 2011.
- [89] Bhaskar Saha, Kai Goebel, and Jon Christophersen. Comparison of prognostic algorithms for estimating remaining useful life of batteries. *Transactions of the Institute of Measurement and Control*, 31(3-4):293–308, 2009.
- [90] Nassim A Samad, Youngki Kim, and Jason B Siegel. On power denials and lost energy opportunities in downsizing battery packs in hybrid electric vehicles. *Journal of Energy Storage*, 16:187–196, 2018.
- [91] Zachary J Schiffer, John Cannarella, and Craig B Arnold. Strain derivatives for practical charge rate characterization of lithium ion electrodes. *Journal of The Electrochemical Society*, 163(3):A427–A433, 2016.
- [92] Johannes Schmalstieg, Stefan Käbitz, Madeleine Ecker, and Dirk Uwe Sauer. A holistic aging model for li (nimnco) o2 based 18650 lithium-ion batteries. *Journal of Power Sources*, 257:325–334, 2014.
- [93] Alexander P Schmidt, Matthias Bitzer, Árpád W Imre, and Lino Guzzella. Experiment-driven electrochemical modeling and systematic parameterization for a lithium-ion battery cell. *Journal of Power Sources*, 195(15):5071–5080, 2010.
- [94] GA Sever and CJ Wild. Nonlinear regression. *Hoboken: Wiley*, 2003.
- [95] Kristen A Severson, Peter M Attia, Norman Jin, Nicholas Perkins, Benben Jiang, Zi Yang, Michael H Chen, Muratahan Aykol, Patrick K Herring, Dimitrios Fraggedakis, et al. Data-driven prediction of battery cycle life before capacity degradation. *Nature Energy*, 4(5):383–391, 2019.
- [96] Joongpyo Shim, Robert Kosteki, Thomas Richardson, Xiangyun Song, and Kathryn A Striebel. Electrochemical analysis for cycle performance and capacity fading of a lithium-ion battery cycled at elevated temperature. *Journal of power sources*, 112(1):222–230, 2002.
- [97] Sarah G Stewart, Venkat Srinivasan, and John Newman. Modeling the performance of lithium-ion batteries and capacitors during hybrid-electric-vehicle operation. *Journal of The Electrochemical Society*, 155(9):A664–A671, 2008.
- [98] Barbara Stiaszny, Jörg C Ziegler, Elke E Krauß, Jan P Schmidt, and Ellen Ivers-Tiffée. Electrochemical characterization and post-mortem analysis of aged limn2o4–li (ni0. 5mn0. 3co0. 2) o2/graphite lithium ion batteries. part i: Cycle aging. *Journal of Power Sources*, 251:439–450, 2014.
- [99] Petre Stoica and Boon Chong Ng. On the cramér-rao bound under parametric constraints. *IEEE Signal Processing Letters*, 5(7):177–179, 1998.
- [100] Valentin Sulzer, Scott G Marquis, Robert Timms, Martin Robinson, and S Jon Chapman. Python battery mathematical modelling (pybamm). *ECSarXiv*, 2020.

- [101] Valentin Sulzer, Peyman Mohtat, Suhak Lee, Jason B Siegel, and Anna G Stefanopoulou. Promise and challenges of a data-driven approach for battery lifetime prognostics. *arXiv preprint arXiv:2010.07460*, 2020.
- [102] Tanvir R Tanim and Christopher D Rahn. Aging formula for lithium ion batteries with solid electrolyte interphase layer growth. *Journal of Power Sources*, 294:239–247, 2015.
- [103] Fabio Todeschini, Simona Onori, and Giorgio Rizzoni. An experimentally validated capacity degradation model for li-ion batteries in phevs applications. *IFAC Proceedings Volumes*, 45(20):456–461, 2012.
- [104] Shijie Tong, Matthew P Klein, and Jae Wan Park. On-line optimization of battery open circuit voltage for improved state-of-charge and state-of-health estimation. *Journal of Power Sources*, 293:416–428, 2015.
- [105] SA Vakhrameev. A bang-bang theorem with a finite number of switchings for nonlinear smooth control systems. *Journal of Mathematical Sciences*, 85(3):2002–2016, 1997.
- [106] Klaus J Vetter. *Electrochemical kinetics: theoretical aspects*. Elsevier, 2013.
- [107] Georg Vossen. Switching time optimization for bang-bang and singular controls. *Journal of optimization theory and applications*, 144(2):409–429, 2010.
- [108] Thomas Waldmann, Marcel Wilka, Michael Kasper, Meike Fleischhammer, and Margret Wohlfahrt-Mehrens. Temperature dependent ageing mechanisms in lithium-ion batteries—a post-mortem study. *Journal of Power Sources*, 262:129–135, 2014.
- [109] John Wang, Justin Purewal, Ping Liu, Jocelyn Hicks-Garner, Souren Soukazian, Elena Sherman, Adam Sorenson, Luan Vu, Harshad Tataria, and Mark W Verbrugge. Degradation of lithium ion batteries employing graphite negatives and nickel–cobalt–manganese oxide+spinel manganese oxide positives: Part 1, aging mechanisms and life estimation. *Journal of Power Sources*, 269:937–948, 2014.
- [110] Zhenpo Wang, Jun Ma, and Lei Zhang. State-of-health estimation for lithium-ion batteries based on the multi-island genetic algorithm and the gaussian process regression. *Ieee Access*, 5:21286–21295, 2017.
- [111] Jingwen Wei, Guangzhong Dong, and Zonghai Chen. Remaining useful life prediction and state of health diagnosis for lithium-ion batteries using particle filter and support vector regression. *IEEE Transactions on Industrial Electronics*, 65(7):5634–5643, 2017.
- [112] Caihao Weng, Yujia Cui, Jing Sun, and Huei Peng. On-board state of health monitoring of lithium-ion batteries using incremental capacity analysis with support vector regression. *Journal of Power Sources*, 235:36–44, 2013.
- [113] Caihao Weng, Jing Sun, and Huei Peng. A unified open-circuit-voltage model of lithium-ion batteries for state-of-charge estimation and state-of-health monitoring. *Journal of power Sources*, 258:228–237, 2014.

- [114] Keith B Wipke, Matthew R Cuddy, and Steven D Burch. Advisor 2.1: A user-friendly advanced powertrain simulation using a combined backward/forward approach. *IEEE transactions on vehicular technology*, 48(6):1751–1761, 1999.
- [115] M Wohlfahrt-Mehrens, C Vogler, and J Garche. Aging mechanisms of lithium cathode materials. *Journal of power sources*, 127(1-2):58–64, 2004.
- [116] Lifeng Wu, Xiaohui Fu, and Yong Guan. Review of the remaining useful life prognostics of vehicle lithium-ion batteries using data-driven methodologies. *Applied Sciences*, 6(6):166, 2016.
- [117] Yinjiao Xing, Wei He, Michael Pecht, and Kwok Leung Tsui. State of charge estimation of lithium-ion batteries using the open-circuit voltage at various ambient temperatures. *Applied Energy*, 113:106–115, 2014.
- [118] Rui Xiong, Fengchun Sun, Zheng Chen, and Hongwen He. A data-driven multi-scale extended kalman filtering based parameter and state estimation approach of lithium-ion polymer battery in electric vehicles. *Applied Energy*, 113:463–476, 2014.
- [119] Duo Yang, Xu Zhang, Rui Pan, Yujie Wang, and Zonghai Chen. A novel gaussian process regression model for state-of-health estimation of lithium-ion battery using charging curve. *Journal of Power Sources*, 384:387–395, 2018.
- [120] Yilin Yin and Song-Yul Choe. Actively temperature controlled health-aware fast charging method for lithium-ion battery using nonlinear model predictive control. *Applied Energy*, 271:115232, 2020.
- [121] Chi Zhang, Fuwu Yan, Changqing Du, Jianqiang Kang, and Richard Fiifi Turkson. Evaluating the degradation mechanism and state of health of lifepo4 lithium-ion batteries in real-world plug-in hybrid electric vehicles application for different ageing paths. *Energies*, 10(1):110, 2017.
- [122] Liqiang Zhang, Chao Lyu, Gareth Hinds, Lixin Wang, Weilin Luo, Jun Zheng, and Kehua Ma. Parameter sensitivity analysis of cylindrical lifepo4 battery performance using multi-physics modeling. *Journal of The Electrochemical Society*, 161(5):A762, 2014.
- [123] Mingchuan Zhao, Stephen Kariuki, Howard D Dewald, Frederick R Lemke, Robert J Staniewicz, Edward J Plichta, and Richard A Marsh. Electrochemical stability of copper in lithium-ion battery electrolytes. *Journal of the Electrochemical Society*, 147(8):2874–2879, 2000.
- [124] Honghe Zheng, Qingna Sun, Gao Liu, Xiangyun Song, and Vincent S Battaglia. Correlation between dissolution behavior and electrochemical cycling performance for $\text{lini}_{1/3}\text{co}_{1/3}\text{mn}_{1/3}\text{o}_2$ -based cells. *Journal of Power Sources*, 207:134–140, 2012.
- [125] Yuan Zou, Xiaosong Hu, Hongmin Ma, and Shengbo Eben Li. Combined state of charge and state of health estimation over lithium-ion battery cell cycle lifespan for electric vehicles. *Journal of Power Sources*, 273:793–803, 2015.